THESIS

TOWARDS UNDERSTANDING THE PROCESSES THAT INFLUENCE GLOBAL MEAN TEMPERATURE

Submitted by

Kathryn A. Mullin

Department of Atmospheric Science

In partial fulfillment of the requirements

For the Degree of Master of Science

Colorado State University

Fort Collins, Colorado

Fall 2011

Master's Committee:

Advisor: David Thompson

Scott Denning
Julia Klein

ABSTRACT

TOWARDS UNDERSTANDING THE PROCESSES THAT INFLUENCE GLOBAL MEAN TEMPERATURE

Global mean surface temperature variability is largely determined by the global mean surface energy budget, which is driven by many natural and anthropogenic forcings. In theory, if all natural sources of global mean temperature variability could be removed from the global mean temperature time series the anthropogenic signal would be clearer. Previous studies have exploited this reasoning to remove the signature of volcanoes, the El-Niño Southern Oscillation (ENSO), and dynamic variability from the global mean temperature time series. This thesis extends previous work by 1) examining the linkages between global mean temperature and natural variability as a function of timescale; and 2) examining the two-way coupling between area-averaged surface temperatures and sea ice concentration. The results reveal a series of unique spatial structures in surface temperatures that drive intraannual, interannual, and decadal variability in global mean temperature. The results confirm the apparent role of hemispheric mean temperatures in driving sea ice variability, and also point to a possible feedback between wintertime sea ice concentration and springtime surface

temperatures over the Northern Hemisphere. Linkages between sea ice concentration and surface temperature in the Southern Hemisphere are much weaker, and it can be argued that the hemispheric difference in these linkages may aid in explaining the different trends in sea ice between the two hemispheres.

ACKNOWLEDGEMENTS

Deepest thanks go to my advisor Dr. David W. J. Thompson, whose support and guidance have been invaluable. I would also like to thank my committee members, Dr. Scott Denning, Professor of Atmospheric Science at Colorado State University (CSU), and Dr. Julia Klein, Professor of Forest, Rangeland, and Watershed Stewardship at Colorado State University (CSU). Further thanks go to my research group, especially Kevin Grise for his help with various questions over the past two years. I would also like to thank my classmates, roommate, and family for their support. This research was supported by a NSF Climate Dynamics grant.

TABLE OF CONTENTS

CHAPTER ONE

Introduction

Earth's global climate system can be viewed in the context of its energy budget. The energy balance at the top of the atmosphere is key as it determines the net energy within the Earth system (Hartmann, 1994). The energy balance at the surface is important in determining the overall earth-atmosphere energy balance, and how much energy is available to evaporate surface water and to change the temperature of the surface (Figure 1.1).

The global mean surface energy budget determines global mean surface temperature. The latter is important for at least two reasons: (1) global mean temperatures are expected to rise in response to increasing greenhouse gases and (2) global mean temperatures provide one of the longest and best available environmental records. The observed surface warming of the past century was roughly 0.75°C (Figure 1.2; IPCC Chapter 3, 2007) and this warming has been clearly linked to radiative forcing by greenhouse gases (Santer et al., 1996). However, the warming is also obscured to some extent by natural variability in the climate system. The natural variability can mask the effect of anthropogenic forcing, and the broad goals of this research are to quantify the natural variability and thus isolate more clearly the effects of human emissions on global mean temperature. This chapter reviews the natural and anthropogenic factors that are thought to affect the surface energy budget and global mean temperature. We will begin with an overview of the surface energy budget and move on to a discussion of sources of global mean temperature variability, both natural and anthropogenic.

1.1 The Surface Energy Budget

Before we discuss specific sources of global mean temperature variability in more detail it is important to understand how earth's surface temperature changes. Surface temperature can be better understood by looking at the surface energy budget. The surface energy budget is more complex than the energy budget at the top of the atmosphere. It considers not just radiation, but fluxes by conduction and convection of heat and moisture as well. Figure 1.1 illustrates the fluxes present at earth's surface: radiative (both longwave and shortwave), latent heat, and sensible heat. The surface flux can be written as follows:

$$\frac{\partial E_S}{\partial t} = G = R_S - LE - SH - \Delta F_{eo} \tag{1.1}$$

where $\frac{\partial E_S}{\partial t} = G$ is the storage of energy in the surface soil and water, R_S is the net radiative flux of energy into the surface, LE is the latent heat flux from the surface to the atmosphere, SH is the sensible heat flux from the surface to the atmosphere, and ΔF_{eo} is the horizontal flux out of the column of land-ocean below the surface. For our purposes, ΔF_{eo}, the horizontal flux out of the column can be assumed to be negligible (Hartmann, 1994).

1.1.1 Radiative Flux

We will first look more closely at the radiative portion of the energy budget. The net radiative flux at earth's surface, the sum of radiative inputs and outputs, plays a large role in controlling earth's surface temperature. There are four main components in the net surface radiative flux: the upward and downward shortwave radiation flux and the upward and downward longwave radiation flux. Shortwave radiation refers to wavelengths that carry most of the energy associated with solar radiation (less than 4μm), while longwave radiation is associated with wavelengths that contain most of the terrestrial radiation (greater than 4μm) (Wallace and Hobbs, 2006). The net radiative flux (R_S) can be described by the following equation:

$$R_S = F_{S\downarrow} - F_{S\uparrow} + F_{L\downarrow} - F_{L\uparrow} \tag{1.2}$$

In equation 1.2, $F_{S\downarrow}$ is the flux of downward shortwave radiation from the sun that reaches earth's surface. Incoming solar radiation can be reflected, absorbed, and transmitted by clouds and aerosols as it moves through the atmosphere, and thus, $F_{S\downarrow}$ is often less than the solar radiation incident on the top of the atmosphere. $F_{S\uparrow}$ accounts for the sunlight reflected by earth's surface. $F_{L\downarrow}$ is the flux of longwave radiation from the atmosphere that reaches the earth's surface. And $F_{L\uparrow}$ is the upward flux of longwave radiation from the surface. The sum of the four fluxes, R_S, is nearly constant throughout a given day (Wallace and Hobbs, 2006).

Of the 342W/m^2 of solar energy present at the top of the atmosphere, 49%, or 168 W/m^2, is absorbed by the earth's surface. The remaining energy is reflected (107 W/m^2) or absorbed by the atmosphere (67 W/m^2) through water vapor, clouds, aerosols, and ozone. As for longwave radiation, the surface emits 390 W/m^2 upwards, while 324 W/m^2 are reabsorbed by the earth's surface. When all fluxes of shortwave and longwave radiation at the surface are summed, the surface gains 102 W/m^2 of energy (168 W/m^2 – 390 W/m^2 + 324 W/m^2 = 102 W/m^2). In general, the surface surplus of energy radiatively balances the atmosphere, which represents an energy deficit of 102 W/m^2. The loss of 102 W/m^2 in the atmosphere would mean a 200°C cooling over the course of one year (Ackerman and Knox, 2002). Since the temperature of the atmosphere if fairly stable this is obviously not the case. Something must be facilitating energy transfer from the surface to the atmosphere. This transfer occurs not by radiation, but by two other forms of heat transfer discussed below, latent heat and sensible heat transfer.

1.1.2 Latent and Sensible Heat Fluxes

Latent and sensible heat fluxes act to deplete the energy imbalance between the atmosphere and the earth's surface. Both fluxes are produced by turbulent motions in the boundary layer, or the lowest part of the atmosphere that is directly influenced by its interactions with earth's surface. Latent heat accounts for roughly 78 W/m^2 of energy transfer from the surface to the atmosphere and is associated with heat related to moisture. Latent heat transfer can occur by processes such as evaporation from oceans and lakes and sublimation from glaciers (Ackerman and

Knox, 2002). Latent heat flux is related to the difference in specific humidity (q) between the surface and the atmosphere at a reference height and can be estimated using the bulk aerodynamic formula:

$$LE = L\rho C_{DE} U_r \left(q_s - q_a\left(z_r\right)\right) \tag{1.3}$$

where L is the latent heat of evaporation, ρ is air density, C_{DE} is the aerodynamic transfer coefficient for humidity, U_r is the wind speed at a reference level, q is the specific humidity at the surface (s) and at a reference air level (a), and z_r is the reference height (Hartmann, 1994).

Sensible heat accounts for 24W/m^2 of energy transferred from earth's surface to the atmosphere and occurs through the processes of conduction and convection (Ackerman and Knox, 2002). The sensible heat flux relates to mean wind speed and temperature and can also be estimated using a bulk aerodynamic formula:

$$SH = c_p \rho C_{DH} U_r \left(T_s - T_a\left(z_r\right)\right) \tag{1.4}$$

where c_p is the specific heat of air at constant pressure, ρ is air density, C_{DH} is the aerodynamic transfer coefficient for temperature, U_r is the wind speed at a reference level, T is temperature, and z_r is the reference height (Hartmann, 1994). As before, subscripts s and a indicate values at the surface and air at a reference level.

The rate of cooling due to latent and sensible heat fluxes over land is roughly equal when averaged over the globe. However, latent heat is the bigger player over ocean areas due to large amounts of available moisture. Over the oceans sensible heat accounts for roughly one tenth of the cooling due to latent heat fluxes (Hartmann, 1994). This imbalance accounts for the smaller total energy flux by sensible heat (24W/m^2) versus latent heat (78W/m^2) when averaged over the globe.

Now that the surface energy budget and the fluxes involved (radiative, latent, and sensible) have been explained in detail we can move onto a discussion of specific sources of global mean temperature variability. When possible, the physical processes inherent in sources of global mean temperature variability will be explained in terms of the surface energy budget. Both natural and anthropogenic sources of global mean temperature variability exist. We will begin by reviewing natural sources of variability.

1.2 Natural Sources of Global Mean Temperature Variability

Natural sources of climate variability have been affecting our historical and prehistorical climate record, as diagnosed by climate proxies, before anthropogenic influences are thought to have existed. They are still affecting the climate in addition to today's anthropogenic influences. Natural variables that contribute to variations in global mean temperature include: solar variability, El Niño–Southern Oscillation (ENSO), dynamic variability, volcanic eruptions, sea ice cover, water vapor, precipitation, and clouds.

1.2.1 Solar Variability

Solar radiation is by far the most important incoming form of energy for the earth-atmosphere system (see incoming shortwave radiation in Figure 1.1). Thus, one would assume that changes in solar radiation would influence the global mean temperature time series. Many potential mechanisms for solar forcing of global mean temperature have been proposed, from indirect effects of ultraviolet radiation and indirect effects of galactic cosmic rays, to the influences of orbital cycles, solar cycle variability and direct impacts on top of atmosphere radiation (Lean et al., 2005; Erlykin et al., 2009).

The potential mechanisms for solar forcing are briefly described in the following paragraphs. The indirect effect associated with ultraviolet radiation is hypothesized to occur due to the greater variability of solar irradiance at ultraviolet wavelengths and its interactions with the stratosphere and atmospheric ozone. Increased solar radiation can be assumed to increase stratospheric ozone production, which can have impacts on climate through tropospheric-stratospheric coupling (Lean et al., 1995). Large-scale stratospheric circulation anomalies in the lowermost stratosphere can cause changes in tropospheric circulation; however, the specific mechanism behind this coupling is still under analysis and the exact climatic implications for surface temperature changes are unclear (Baldwin et al., 2001).

As for galactic cosmic rays, their impact on climate is not widely understood or accepted, but they are thought to indirectly affect global mean temperature by impacting cloud cover (Benestad, 2005). Galactic cosmic rays are very energetic particles produced by stellar process in our galaxy (Svensmark, 1998). It is thought that solar variability associated with cosmic rays more strongly influences low clouds, rather than high clouds, and does so through a microphysical process in which aerosol formation is enhanced by ionization due to cosmic rays (Marsh and Svensmark, 2000). If cosmic rays do indeed enhance formation of low clouds they will act to decrease the surface temperature of the earth by causing emission of high temperature longwave radiation and reflection of shortwave radiation to space (Kirby et al., 2011).

Orbital cycles, which explain the movement and position of the earth around the sun, can explain changes in solar radiation received at earth's surface on the order of tens to hundreds of thousands of years. On shorter timescales, solar irradiance records show day-to-week variations associated with the sun's rotation around its axis and longer decadal fluctuations related to the 11-year solar activity cycle. Current solar variability is primarily caused by solar activity: sunspots (dark features in which radiation is lessened) and faculae (bright features in which radiation is enhanced) (Lean et al., 2005). The effect of the faculae is greater than that of the sunspots and thus, periods with large number of sunspots are periods of high solar flux. It has been estimated that earth's surface warms by 0.1°C at solar cycle maxima, which is equivalent to a forcing of $0.2 W/m^2$ (Lean et al., 2005). It is also thought that solar variability has the potential to amplify climate modes such as El-Niño Southern Oscillation and the North Atlantic Oscillation through noise amplifications enabled by weak solar forcing (Lean et al., 2002; Rahmstorf and Alley, 2002).

While solar activity can influence the global surface energy budget, it does not have a large impact on global mean temperature, at least over the last few centuries. For example, in looking at the long–term variability of the 11-year solar cycle the change in total irradiance from the 17th century Maunder Minimum to the current cycle minima is 0.04%, which is an increase of roughly $0.5W/m^2$ out of a total of $1365W/m^2$. This leads to a radiative forcing of only $+0.1W/m^2$, which is small compared to anthropogenic forcing agents over the same period (IPCC Chapter 2, 2007). Models of climate response to solar variability, which have been calibrated to produce the Maunder Minimum, have been used to predict climate change due to solar variability. These models suggest a solar-related surface temperature change of 0.2°C-0.4°C over recent centuries, which is too small to explain the global warming of the past few decades (Rind et al., 1999; Crowley, 2000; Fröhlich and Lean, 2004).

It is interesting to think about the timescales on which each source of variability may influence global mean surface temperature. Figure 1.3 gives an example of the trends in global mean temperature at different temporal scales. Variations that stem from solar variability range from days, to weeks, to thousands of years. Many of the sources of variability discussed below do not cover nearly as large a range of variability timescales as solar influence does. They are generally confined to a particular timescale of variability, i.e. intraannual, interannual, decadal, or greater.

1.2.2 El-Niño Southern Oscillation

The El-Niño Southern Oscillation (ENSO) is a coupled ocean-atmosphere phenomenon in the tropical Pacific. In the 1960's Bjerknes noticed that the zonal gradient in equatorial sea surface temperature (SST) drives the easterlies in the tropical Pacific (Bjerknes, 1969). These easterlies create cold SST anomalies in the eastern portion of the Pacific through upwelling and act to strengthen the SST gradient. While cold SST anomalies occur in the eastern Pacific, warm SST anomalies and increased convection are present in the western Pacific. Bjerknes noticed that there was a positive feedback present in this setup. Stronger SST gradients lead to stronger easterlies, which lead to stronger SST gradients. There is also a positive feedback present during the opposite state, El-Niño, wherein the thermocline relaxes, warm water moves into the eastern tropical Pacific, and the easterlies and upwelling weaken. The Bjerknes positive feedback therefore acts to maintain SST anomalies, warm and cold (Jin, 1997).

How does ENSO relate to global mean temperature variability? Its main interaction stems from the exchange of heat between the subsurface ocean and the atmosphere-ocean mixed layer (the coupled system of the lower atmosphere and the upper well-mixed isopycnal layer of the ocean), primarily in the eastern equatorial Pacific (Thompson et al., 2009). During the ENSO cycle, latent and sensible heat fluxes over the cold, easterly Pacific are enhanced (Yulaleva and Wallace, 1994). This exchange of heat often occurs through ocean evaporation and is realized in the atmosphere as latent heat in precipitation. This diabatic heating is what drives large-scale atmospheric overturning that influences responses in the tropics, subtropics, and many other areas of the globe via teleconnections. In many areas away from the tropical Pacific, the changes in atmospheric circulation that are driven from the tropical Pacific are what influence changes in surface temperature. In these ways, ENSO events are known to contribute to interannual and decadal variations in the global mean temperature record (Trenberth et al., 2002). In looking at Figure 1.3, interannual and decadal variability can be seen in the bottom two panels.

Many estimates of the signal of ENSO in global mean temperature exist. Trenberth et al. (2002) estimate that between 1950-1998 ENSO is responsible for 13.6% of the linear trend in global surface temperature. A more recent paper by Thompson et al. (2009) estimates that ENSO explains 16.8% of the variance in the global mean temperature time series. It is interesting to note, and likely not coincidental, that the warmest years on record to date are also years associated with ENSO events.

1.2.3 Dynamical Variability

Dynamically induced atmospheric variability is thought to account for a large portion of the high frequency variability in global mean temperature (Hurrell, 1995; Wallace et al., 1995). Figure 1.4 from Thompson et al. (2009) clearly shows high frequency, or month-to-month, variability in the land temperature time series (part b). This high frequency variability is also evident in the top panel of Figure 1.3.

These dynamical variations, caused by temporal changes in global circulation, stem mainly from the difference in heat capacity between land and ocean. For example, in some months surface westerlies could be stronger than normal over the middle and subpolar latitudes of the Northern Hemisphere. This results in anomalous warm advection over the Northern Hemisphere landmasses and anomalous cold advection over the oceans (Hurrell, 1995). Since land has a smaller heat capacity than water, temperature anomalies on short timescales are generally larger over land than ocean, as seen in Figure 1.5 (Broccoli et al., 1998). Thus, during times when large positive temperature anomalies occur over Northern Hemisphere landmasses, the global mean temperature rises. This pattern in temperature differences over the continents and oceans is often referred to as the Cold Ocean-Warm Land (COWL) pattern (Wallace et al., 1995; Broccoli et al., 1998). The COWL pattern can shift polarity between months and seasons depending on the relative temperature of the continents and oceans, which explains its association with high frequency surface temperature variability.

Variations due to dynamical variability tend to be most important in the Northern Hemisphere, where a greater percentage of the hemisphere is covered by land than in the Southern Hemisphere, and during the winter months, when surface winds are strongest and land-sea contrasts and surface heat fluxes are enhanced (Wallace et al., 1996; Thompson et al., 2009). Dynamical variability may also relate to snow and ice albedo feedbacks during these months. While variations caused by dynamical variability are important, their tendency to be of high frequency often acts to obscure longer-term trends in the global mean temperature record. Accounting for and removing their variance is helpful in identifying longer-term trends.

1.2.4 Volcanic Eruptions

Volcanic eruptions have a cooling effect on global surface temperatures. They inject sulfur-rich aerosols into the atmosphere and scatter shortwave radiation, while absorbing longwave radiation (Hansen et al., 1978; Stommel and Stommel, 1983; Hansen et al., 1992). The signal of volcanoes in surface temperature records has been described as a linear cooling followed by exponential warming (Wigley 2000; Santer et al. 2001), the pattern of which can be seen in Figure 1.5 (part e). The atmospheric readjustment time following an eruption has been estimated to be about 7 years, as seen in Figure 1.7, which has potentially important implications for global mean temperature variability on such interannual to interdecadal timescales (Hegerl et al., 2003; Thompson et al., 2009).

1.2.5 Sea Ice

Sea ice and its effect on the global surface energy budget can be best categorized as a feedback, rather than a forcing. However, the influence this feedback has is very important for global mean surface temperature. In recent decades, sea ice has been retreating rapidly in the Arctic (Parkinson and Cavalieri, 2008). This retreat has been more rapid during the summer months (Eisenman et al., 2011). Typically, Arctic sea ice reaches its annual minimum in September (Stroeve et al., 2008). Figure 1.8 provides a clear depiction of declining sea ice extent over the Arctic.

As Arctic sea ice decline continues it contributes to the realization of Arctic amplification. Arctic amplification is based on the assertion that surface temperature rises in response to increasing greenhouse gases will be larger in the Arctic in comparison to the Northern Hemisphere as a whole. This amplification has been illustrated in climate model runs by Manabe and Stouffer (1980). The runs show that ice albedo feedbacks are key in the positive feedback mechanism that amplifies warming in the Arctic. As ice recedes, heat fluxes upwards from the Arctic Ocean, albedo decreases, and more ice melts (Holland, and Bitz, 2003; Serreze et al., 2009). In turn, water vapor and cloud feedbacks become involved. In a study by Deser et al. (2010) a general circulation model (GCM) was used to determine the atmospheric response to Arctic sea loss in the future. The model output shows that Arctic sea loss accounts for most of the seasonal, spatial, and vertical structure of high latitude warming in response to greenhouse gas forcing by the end of the twenty-first century. The increasing surface temperature in the Arctic will likely contribute to an increase in global mean surface temperature.

The trends in Antarctic sea ice extent are more stable than those in the Arctic. Observations show little long-term change in Southern Hemisphere sea ice extent, and if anything, a slight increase (Cavalieri and Parkinson, 2008; Eisenman et al., 2011). A smaller snow-albedo effect in the Antarctic may help contribute to sea ice stability in the region (Manabe and Stouffer, 1980). This leads one to believe that Antarctic sea ice does not contribute to the upward trend in global mean temperature and if anything, it may moderate surface temperature increases. Overall, it is expected that changes in Arctic sea ice extent will have the larger impact on global mean temperature trends in the future.

1.2.6 Water Vapor

Water vapor is a natural part of the earth system and its presence in both the troposphere and stratosphere has important implications for climate and global mean surface temperature. This stems mainly from the fact that water vapor is the single most important greenhouse gas in the atmosphere. Greenhouse gases are atmospheric compounds that allow shortwave radiation from the sun to reach earth's surface, but absorb longwave radiation emitted from earth's surface. They cause the atmosphere to emit less longwave radiation back to space and effectively "trap" energy in the lower atmosphere, causing the greenhouse effect.

Water vapor is the principal absorber of solar radiation in the troposphere (Hartmann, 1994). The effect of tropospheric water vapor on global surface temperatures is best understood through the water vapor feedback mechanism. As global surface temperatures increase the atmosphere is able to hold larger amounts of water vapor and humidity increases (Held and Soden, 2006). Larger amounts of greenhouse gas in the atmosphere, in this case water vapor, will further contribute to increasing global surface temperatures (Yang and Tung, 1997).

Recent observations of stratospheric water vapor can be seen in Figure 1.9. Stratospheric water vapor accounts for less than 1% of all water vapor in the atmosphere, but even so, its presence is thought to contribute to stratospheric cooling and tropospheric warming (Forster and Shine, 2002). Stratospheric water vapor concentrations decreased after the year 2000 by roughly 10%. Solomon et al. (2010) argued that this unexplained decrease slowed the rate of increase in global surface temperatures from 2000-2009 by 25% in comparison to that which would have occurred due to carbon dioxide and other greenhouse gases only (Figure 1.10, part a). Thus, it can be concluded that stratospheric water vapor is a potentially important variable to consider when assessing global mean temperature trends.

1.2.7 Precipitation

Held and Soden (2006) predict that precipitation amounts will increase with global mean temperature. However, in this thesis we are more concerned with how that precipitation will affect the global mean surface temperature. The relationship between precipitation and surface temperature is fairly straightforward. Increased precipitation and surface moisture lead to greater evaporation and cooler surfaces due to latent heat fluxes. Moisture acts as an "air conditioner" (Trenberth and Shea, 2005). On the other hand, less precipitation and fewer clouds allow for increased solar radiation at earth's surface. In this case, surface temperatures are expected to rise (Trenberth et al., 2002). As global surface temperatures continue to rise and precipitation increases, according to Held and Soden (2006), then increased evaporation and latent heat fluxes can be expected to moderate global surface temperature increases (Trenberth and Shea, 2005).

1.2.8 Clouds

The way in which clouds interact with radiation is fairly straightforward. They reflect solar radiation, which acts to cool earth's surface. However, they also absorb and emit longwave radiation and thereby reduce longwave radiation flux at the top of the atmosphere, which warms earth's surface. While these basic interactions are simple, the sum of the influence of all clouds on the radiation budget is very difficult to estimate (Trenberth et al., 2009). To complicate matters, clouds at different heights in the atmosphere have different effects on the surface energy budget. Low altitude clouds tend to cool the surface because they have a high albedo and re-emit at a very warm temperature. High clouds have a warming effect on the surface because they have lower albedos and emit longwave radiation at low temperatures (Kiehl and Trenberth, 1997). Figure 1.11 depicts the difference between high clouds and low clouds. Overall, clouds are estimated to have a cooling effect at the surface and act to moderate surface temperature increases (Ramanathan et al., 1989).

1.3 Anthropogenic Sources of Global Mean Temperature Variability

This section describes the sources of global mean temperature variability thought to be due to human activities. While the natural sources of global mean temperature variability previously discussed have been present for thousands to millions of years, the sources discussed below have developed in the last few decades to centuries. Anthropogenic sources of temperature variability can affect the globe on both short and long timescales and will be discussed further below.

1.3.1 Carbon Dioxide

In terms of net radiative forcing, carbon dioxide (CO_2) is the second most important greenhouse gas after water vapor. But it is the most important greenhouse gas in terms of driving long-term changes in global mean temperature

(Figure 1.12). Increases in CO_2 are associated with rising global mean temperature and the concentration of CO_2 is sharply increasing (Figure 1.13a). It rose from a pre-industrial value of 280ppm to 379ppm in 2005 and will have lasting effects on the global mean temperature into the future (IPCC Technical Summary, 2007). These concentrations of CO_2 are largely irreversible on timescales of many centuries (Solomon et al., 2009). Geo-engineering could potentially be used to reverse these concentrations and/or their effect on surface temperature; however, geo-engineering possibilities will not be discussed here. Gillett et al. (2011) illustrate the permanence of CO_2 effects in simulations of global mean temperature for periods following a complete cessation of CO_2 emissions. In these simulations, after the forcing ceases, the global mean temperature remains high and approximately constant through the end of the next millennium. Clearly, CO_2 imparts a large influence on variations in global mean temperature on decadal to century-long timescales.

The largest source of anthropogenic carbon dioxide emissions comes from the combustion of fossil fuels. This includes the combustion of coal, oil, and natural gas in power plants, automobiles, industry, and other sources (Hartmann, 1994). As of 2006, the emissions associated with combustion of fossil fuels were estimated at over 20,000 Tg of carbon dioxide equivalent, which is over 100 times the size of the second largest source of carbon dioxide emissions, the non-energy use of fuels (EPA, 2011). Deforestation also emits carbon dioxide into the atmosphere by releasing carbon dioxide that has been sequestered in trees. The rate of deforestation has decreased since the 1990s, when nearly 1.6 gigatons of carbon per year were released by clearing trees and changing land use, yet deforestation is still a significant source of global CO_2 emissions today (Jacob, 1999).

While low frequency surface temperature variability is often associated with CO_2 emissions, other studies have identified high frequency variability related to CO_2 as well. Andrews and Forster (2008) conducted a study of doubled CO_2 concentrations on seven slab ocean models and identified the semi-direct forcing of CO_2. This semi-direct forcing is analogous to the cloud semi-direct effect. When forced with increasing CO_2, slab ocean general circulation models (GCMs) were found to respond with a rapid reduction in cloud cover. The radiative effect was thus a result of quick tropospheric adjustment. This cloud adjustment acts to increase the positive radiative forcing of CO_2. The separation between cloud feedbacks and the fast-acting cloud semi-direct effect forced by CO_2 is still unclear, but is of utmost importance in establishing accurate climate change predictions.

1.3.2 Other Greenhouse Gases

Other important greenhouse gases include methane (CH_4), nitrous oxide (N_2O), and halocarbons. They impart an influence similar to CO_2 on global mean temperature. CH_4 comes from a variety of sources, including fossil fuel combustion, rice cultivation, biomass burning, and waste management, while N_2O concentrations stem mainly from soil fertilization (Hartmann, 1994). As greenhouse gas concentrations increase they trap more longwave radiation in the lower atmosphere and cause global surface temperatures to increase. The trends in CH_4 and N_2O can be seen in Figure 1.13b and 1.13c. Changes in concentrations of these gases are likely to increase in the future as fossil fuel combustion and fertilization continue. Thus, they will be expected to account for some variability in the global mean temperature.

1.3.3 Surface Albedo Effect

The albedo, or reflectivity, of earth's surface varies across the globe. Deserts, dry vegetation, and polar areas with sea ice cover and snow pack have high albedos, roughly 25 out of 100 and above. Surfaces such as forests, moist soil, asphalt, and water tend to have lower albedos, generally below 20 (Hartmann, 1994). The surface albedo can very easily be influenced by anthropogenic activity and consequently impact the surface energy budget. Humans often alter the properties of surface cover, whether it is through changing croplands and pastures, to deforestation, or aiding in desertification. Humans also impact the reflectivity of white surfaces (like snow and ice) through emissions of substances like black carbon. Overall, the albedo of earth's surface has been estimated to rise in response to anthropogenic activity (IPCC Chapter 2, 2007). The negative radiative forcing associated with the albedo effect can be seen in Figure 1.12. However, it should be noted that these estimates are still fairly uncertain.

1.3.4 Sulfur Emissions and Aerosol Effects

While fossil fuel combustion produces carbon emissions, it also produces sulfurous emissions. Nearly 72% of atmospheric sulphate aerosol stems from emission of sulfur dioxide (SO_2) from fossil fuel burning, with a small contribution coming from biomass burning as well (IPCC Technical Summary, 2007). Sulfur emissions and sulphuric aerosols emitted by industrial areas tend to have a cooling effect on the climate. They produce a cooling by the direct and indirect aerosol effect. In the direct aerosol effect, aerosols themselves scatter and absorb solar radiation.

Several forms of the indirect effect exist, namely the Twomey Effect and the Cloud Lifetime Effect. In the Twomey Effect, or Cloud Albedo Effect, greater amounts of aerosols lead to more and smaller cloud droplets, which increase the amount of solar radiation the cloud reflects. More reflective clouds generate a negative forcing to Earth's radiation budget (Twomey, 1977). The second indirect effect, the Cloud Lifetime Effect, also rests on the fact that more aerosols lead to more and smaller cloud droplets. However, it explains that the smaller cloud droplets do not collide as efficiently as larger ones. Thus, drizzle formation decreases and the lifetime of the cloud increases (Lohmann, 2006). Longer-lasting clouds result in greater reflection of solar radiation and a negative impact on the surface radiation budget.

The size of the negative radiative forcing enacted by sulfur-containing compounds and clouds can be seen in Figure 1.12 in the total aerosol effect. At this time it is very difficult to assess what the combined forcing of all of the aerosol effects might be and current estimates are uncertain (Connolly et al., 2006 and Lohmann, 2006). It is interesting to note that global sulfur emission is currently decreasing due to changes in policy. SO_2 has an atmospheric lifetime of 1-2 weeks in the troposphere, and a much longer lifetime in the stratosphere due to lack of precipitation (Jacob, 1999). The combination of decreasing sulfur emissions and the short lifetime of SO_2 in the troposphere is expected to impart a positive radiative forcing on the climate system in the future. Like variability associated with sea ice, variability associated with sulfur tends to have a larger influence on the Northern Hemisphere, as emissions are concentrated over the highly populated and industrialized Northern Hemisphere continents. The changes in regional and global emission of sulfur undoubtedly play a part in variations in global mean surface temperature through their influence on albedo and clouds.

1.4 Objectives

The global mean surface temperature has increased in response to anthropogenic forcing over the past century. However, the signal of anthropogenic forcing in the global mean temperature time series is imposed on considerable natural variability on month-to-month, interannual, and decadal timescales. Large scatter in the monthly global mean temperature time series acts to obscure the effects of anthropogenic forcing and introduces large uncertainty into estimates of current trends (Wallace et al., 1995).

In theory the anthropogenic signal in global mean temperature could be isolated if all forms of natural variability are identified, quantified, and removed from the record of global mean temperature. As discussed earlier, several studies have attempted to remove the know variations associated with ENSO, internal atmospheric variability, and volcanic eruptions from global mean temperatures. The goal of this thesis is to extend such analyses by exploring the signatures of dynamical variability on a range of timescales and of sea ice in global mean temperatures. Chapter 2 reviews the data and methods used in the thesis. Chapter 3 focuses on the patterns that contribute to global mean temperature variability on various timescales. Chapter 4 examines the relationship between mean surface temperatures and sea ice cover.

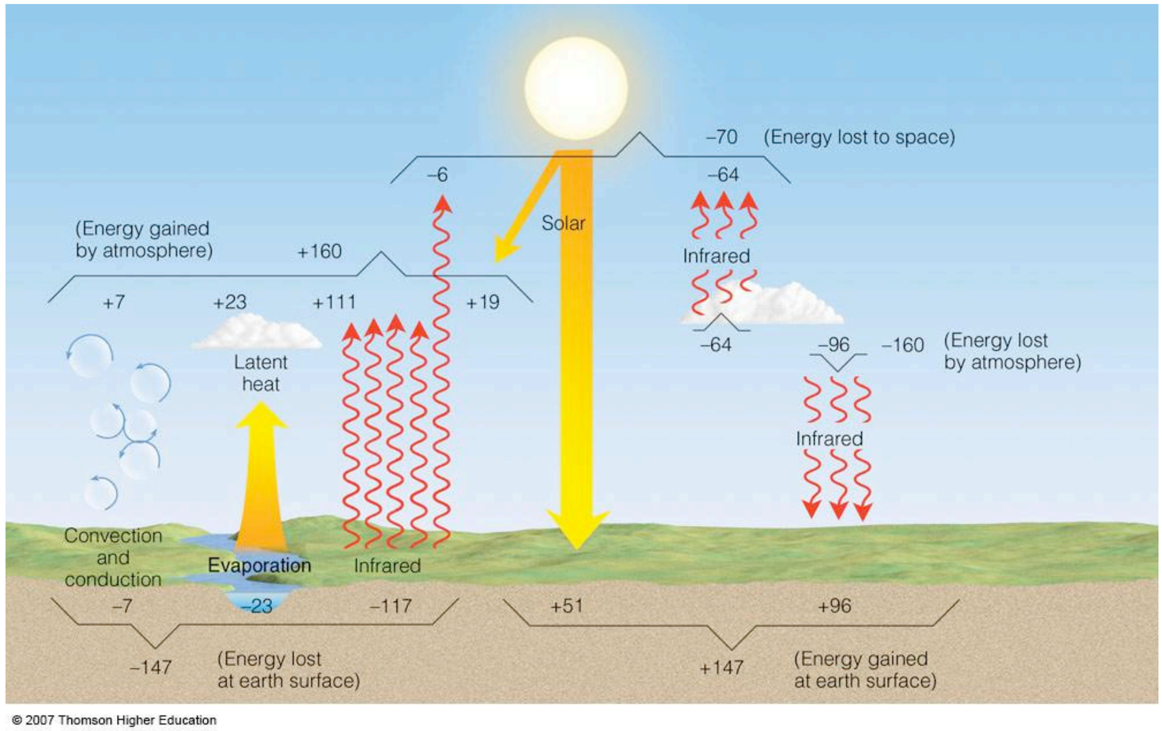

Figure 1.1 The global surface energy budget (Ahrens, 2009).

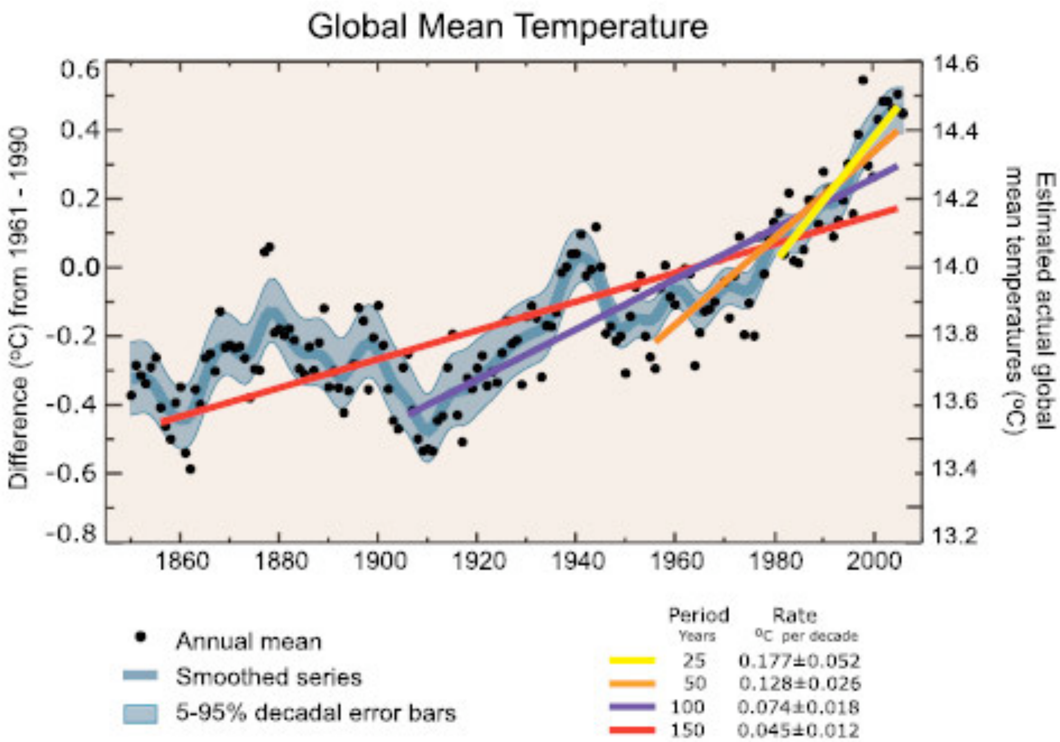

Figure 1.2 From IPCC Chapter 3 (2007). Annual global mean observed temperatures (black dots) along with simple fits to the data. Linear trend fits to the last 25 (yellow), 50 (orange), 100 (purple) and 150 years (red) are shown, and correspond to 1981 to 2005, 1956 to 2005, 1906 to 2005, and 1856 to 2005, respectively. Note that for shorter recent periods, the slope is greater, indicating accelerated warming. The blue curve is a smoothed depiction to capture the decadal variations. To give an idea of whether the fluctuations are meaningful, decadal 5% to 95% (light grey) error ranges about that line are given (accordingly, annual values do exceed those limits). Results from climate models driven by estimated radiative forcings for the 20th century suggest that there was little change prior to about 1915, and that a substantial fraction of the early 20th-century change was contributed by naturally occurring influences including solar radiation changes, volcanism and natural variability.

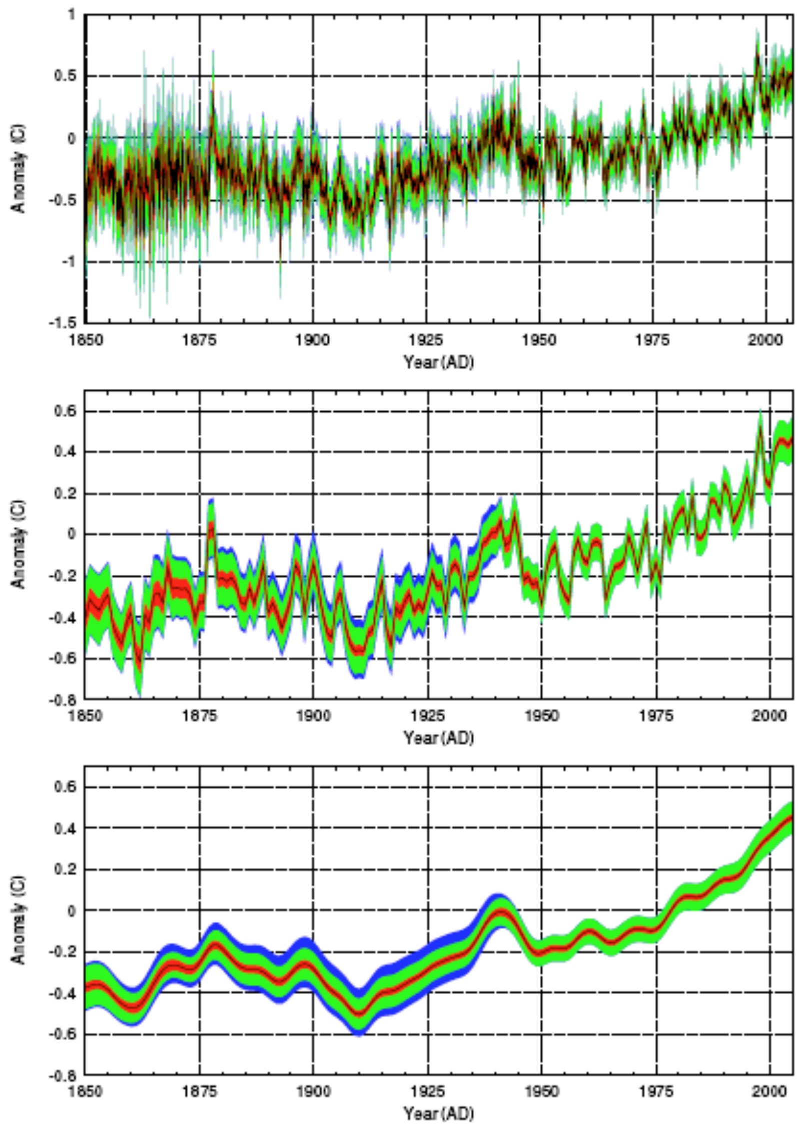

Figure 1.3 From Brohan et al. (2006). HadCRUT3 global temperature anomaly time series (°C) at monthly (top), annual (center), and smoothed annual (bottom) resolutions. The solid black line is the best estimate value; the red band gives the 95% uncertainty range caused by station, sampling and measurement errors; the green band adds the 95% error range due to limited coverage; and the blue band adds the 95% error range due to bias errors.

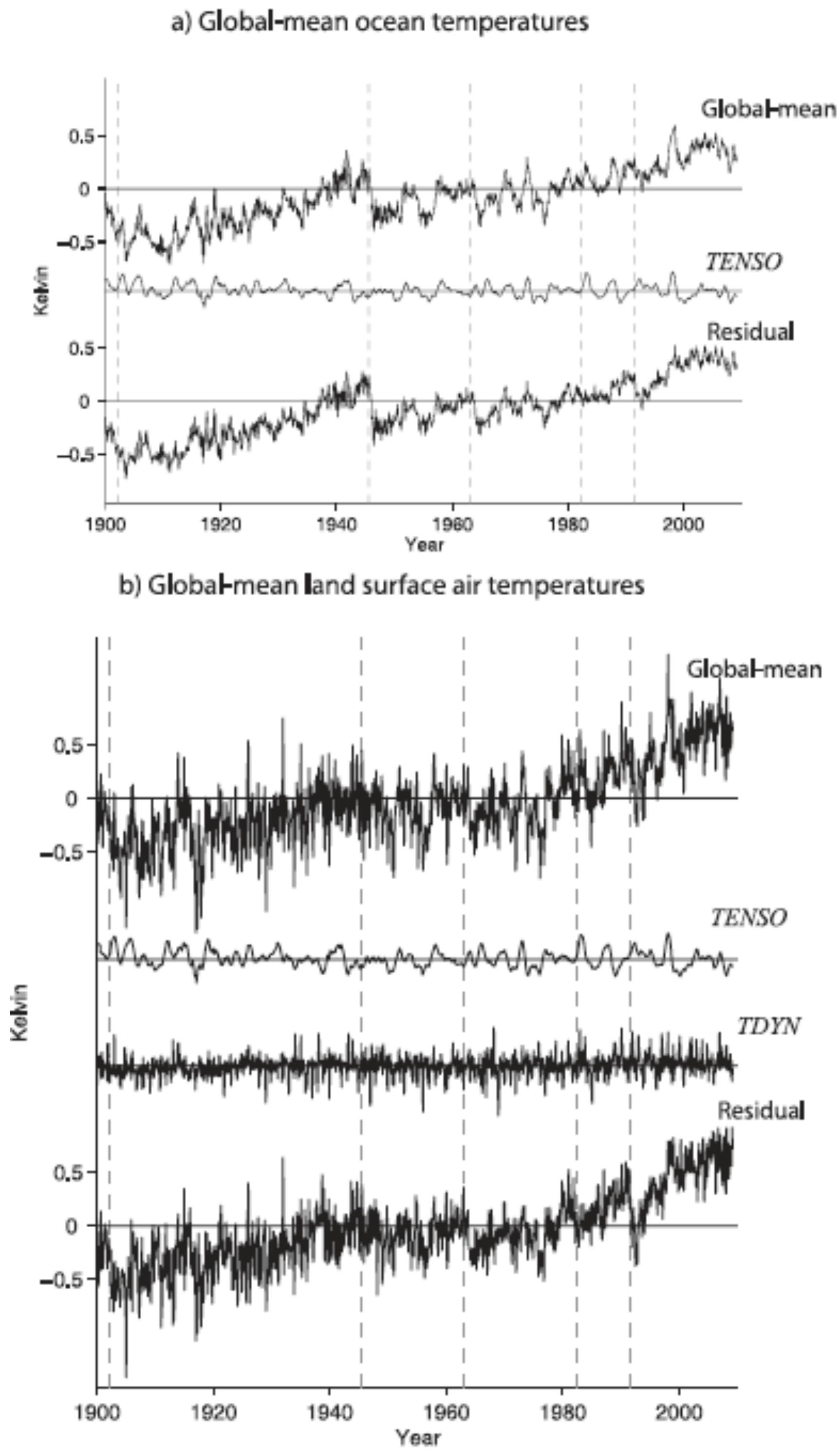

Figure 1.4 From Thompson et al. (2009). (a) global-mean SSTs from the HadSST2 dataset and (b) the global-mean surface land data from the CRUTEM3 dataset. Note that Tdyn is not significantly correlated with the global-mean SST time series and hence is not filtered from the SST data.

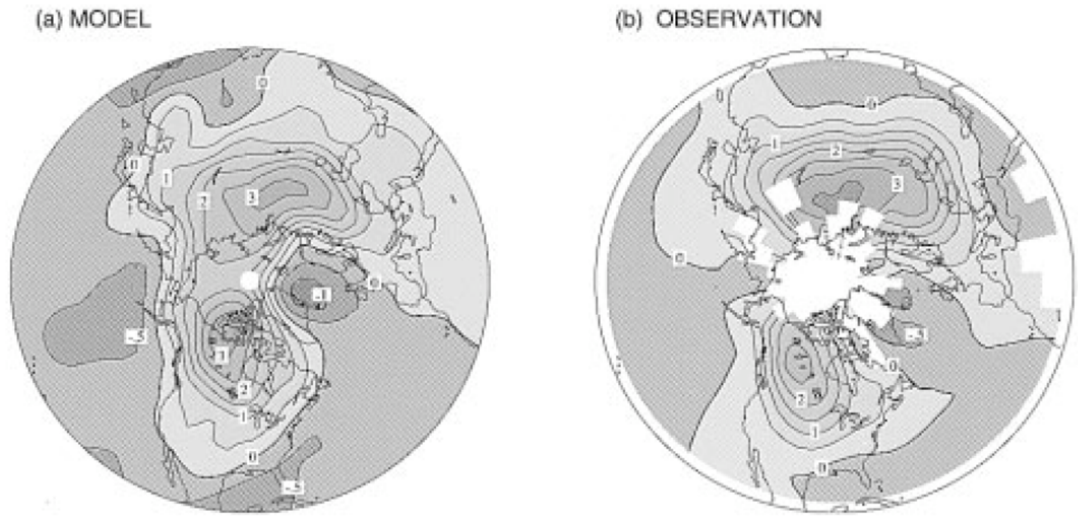

Figure1.5 From Broccoli et al. (1998). Distribution of the structure function for surface air temperature from (a) the 1000-yr coupled model integration, and (b) observations during the 1900–95 period. In both cases, the spatial domain of the analysis is restricted to land north of 20°N. Contour interval is 0.5 dimensionless units.

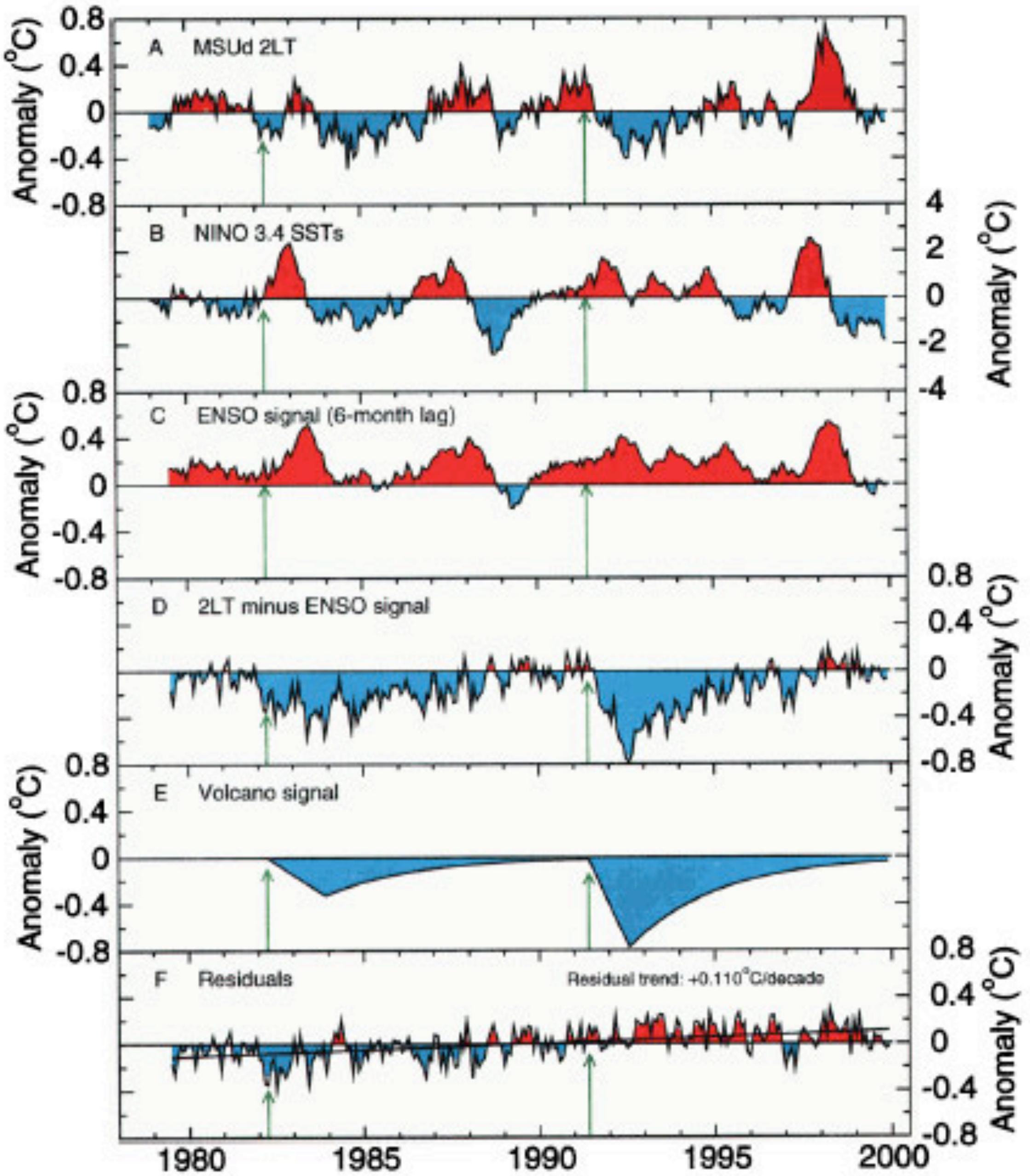

Figure 1.6 From Santer et al. (2001). Estimated ENSO and volcanic signals in observed (MSUd 2LT) monthly mean lower tropospheric temperatures. (a) MSUd 2LT temperature, (b) Nifio3.4 time series, (c) Regression-based estimate of the ENSO effect on 2LT. Subtraction of the ENSO signal from the raw 2LT data yields the residuals in Plate 1d. These were used to estimate the volcanic signal (Plate 1e). The residuals after subtraction of ENSO and volcanic signals from the raw 2LT data are plotted in Plate 1f. All panels except 1e show both unfiltered results (black lines) and data smoothed with a five-term binomial filter (color fill). Results are for the 252-month period January 1979 through December 1999. Green vertical lines mark the times of the El Chichon and Pinatubo eruptions.

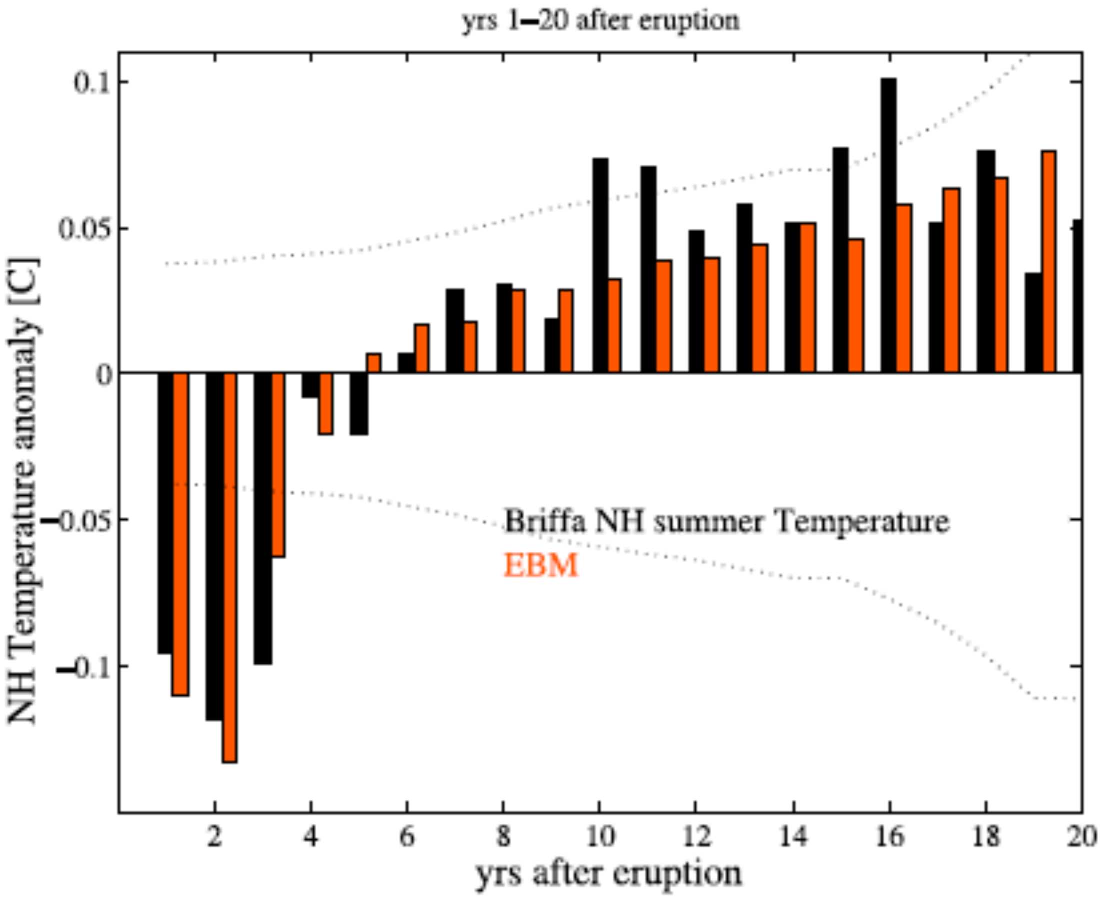

Figure 1.7 From Hegerl et al. (2003). Comparison of the average response to volcanic eruptions in the energy balance model and the Briffa et al. (2001) reconstruction from the year of the eruption (year 1) to the next major eruption. 5–95% uncertainty ranges for the observed response are given by the dotted lines (note that sample size decreases with time).

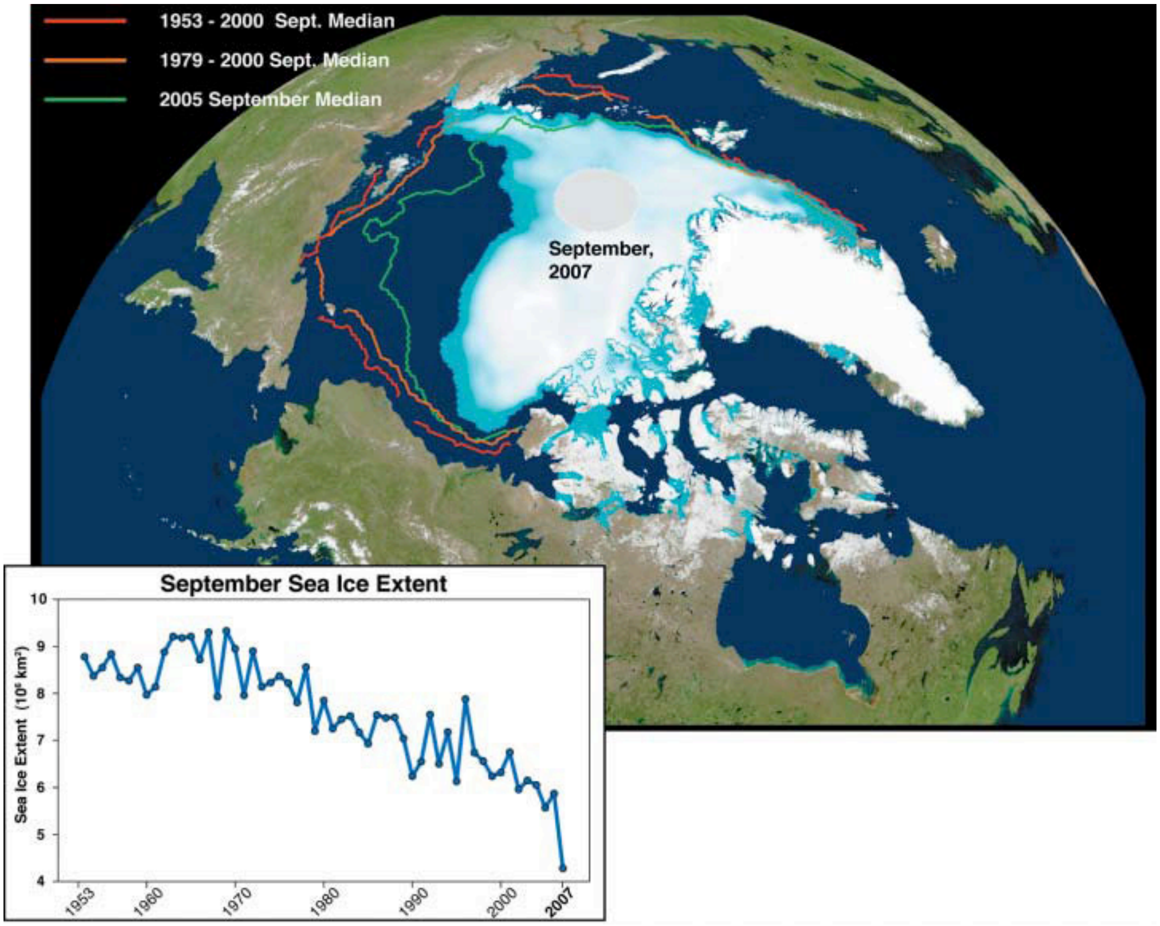

Figure 1.8 From Stroeve et al. (2008). Sea ice concentration for September 2007, along with Arctic Ocean median extent from 1953 to 2000 (red curve), from 1979 to 2000 (orange curve), and for September 2005 (green curve). September ice extent time series from 1953 to 2007 is shown at the bottom.

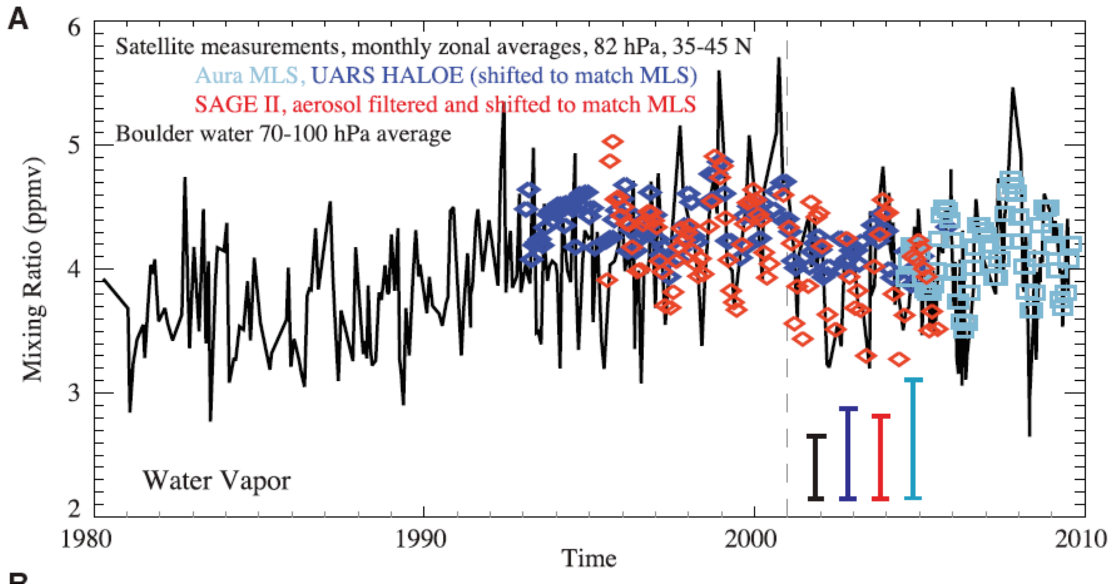

Figure 1.9 From Solomon et al. (2010). Observed changes in stratospheric water vapor. (A) Balloon measurements of water vapor, taken near Boulder, Colorado (40°N, 105.25°W) along with zonally averaged satellite measurements in the 35° to 5° latitude range at 82 hPa from the Aura MLS (turquoise squares), UARS HALOE (blue diamonds), and SAGE II instruments (red diamonds). The SAGE II and HALOE data have been adjusted to match MLS during the overlap period from mid-2004 to the end of 2005. Representative uncertainties are given by the colored bars; for the satellite data sets, these show the precision as indicated by the monthly standard deviations, while for the balloon data set this is the estimated uncertainty provided in the Boulder data files.

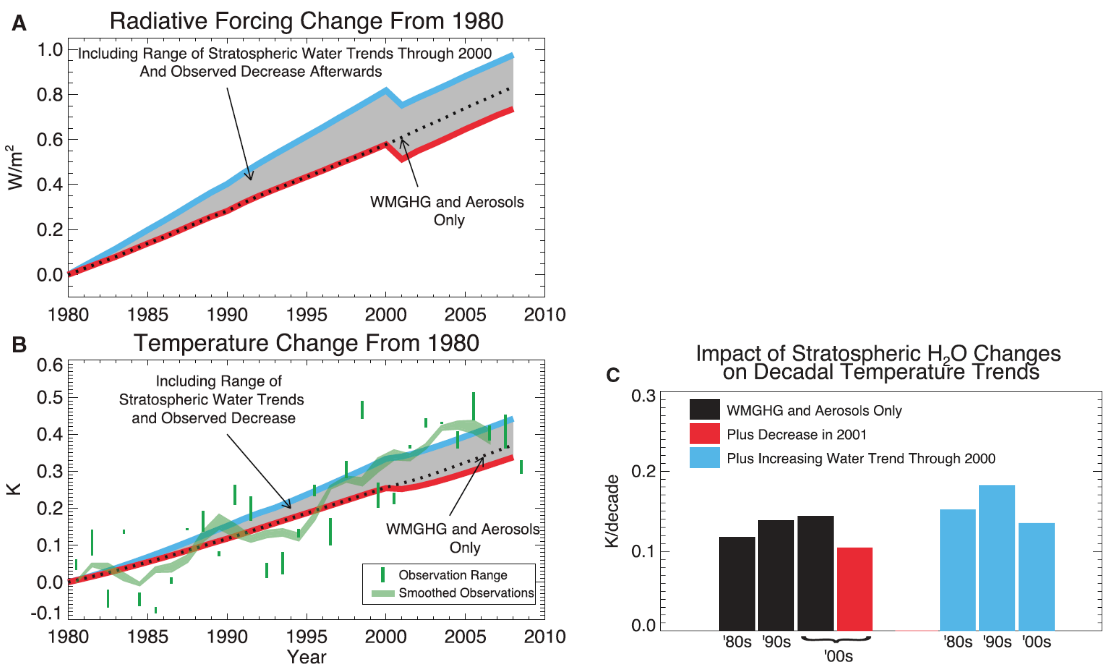

Figure 1.10 From Solomon et al. (2010). Impact of changes in stratospheric water vapor on surface climate. (A) Time series of the changes in radiative forcing since 1980 due to well mixed greenhouse gases (WMGHG), aerosols, and stratospheric water vapor. The forcings of CO2, CH4, and N2O are obtained from historical mixing ratios. The forcing of the Montreal Protocol gases is calculated from their radiative efficiencies and observed mixing ratio time series. The time dependence of the tropospheric aerosol forcing is taken from Goddard Institute for Space Studies (GISS) model input (http://data.giss.nasa.gov/modelforce/RadF.txt), but scaled so that total aerosol radiative forcing from 1985 to 2004 is –1.1 W m–2. The shaded region shows the stratospheric water contribution calculated from an assumed range of decadal trends from 1980 to 2000 of 0 (red line) to 0.5 ppmv per decade (blue line) along with the observed decline prescribed after 2000. (B) Measured and modeled temperature changes relative to 1980. Three different observed global temperature records were used [from the National Climate Data Center (NCDC), Climatic Research Unit (CRU), and GISS records], with the green markers indicating the range across the three data sets in each year. The green shaded line shows the range of the 5-year running mean of the three data sets. (C) Decadal warming rates arising from (i) the WMGHG and aerosols alone (black), as well as (ii) that obtained including the stratospheric water decline after 2000 (red) and (iii) including both the stratospheric water vapor decline after 2000 and the increase in the 1980s and 1990s (cyan). Smooth lines show the warmings calculated by the Bern intermediate complexity climate model, which does not simulate internal variability from one year to another. Volcanoes have not been included in the radiative forcing. The climate sensitivity of the model used is 3°C for a doubling of atmospheric CO2, and the transient climate response is 1.7°C, slightly less than the mean of the range of models assessed by the IPCC. The colors of the bars in (C) correspond to the respective lines shown in (A) and (B).

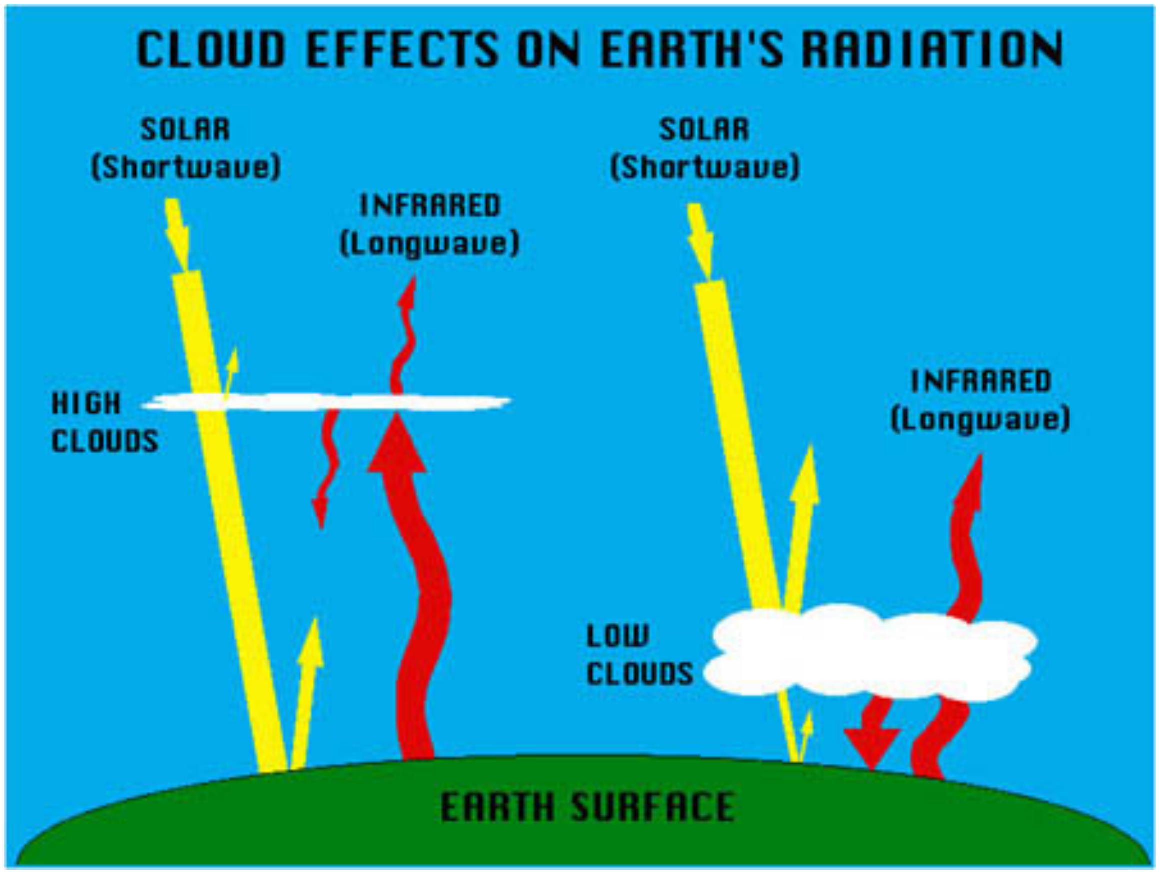

Figure 1.11 From NASA (2004). High clouds and low clouds have different influences on the earth's radiation budget. High clouds are often thin and do not reflect very much. They let lots of solar radiation in. While they are not good at blocking solar radiation they are very good at blocking longwave radiation. High clouds are also colder than low clouds. This means that they radiate less energy into space than the lower, warmer clouds. Therefore, high clouds work to "trap" more energy than the low clouds and will cause a warming of the Earth's surface. Low clouds are often quite thick and reflect lots of solar radiation back to space. But, they don't stop much longwave energy from escaping to space. Therefore, low clouds help to cool the Earth.

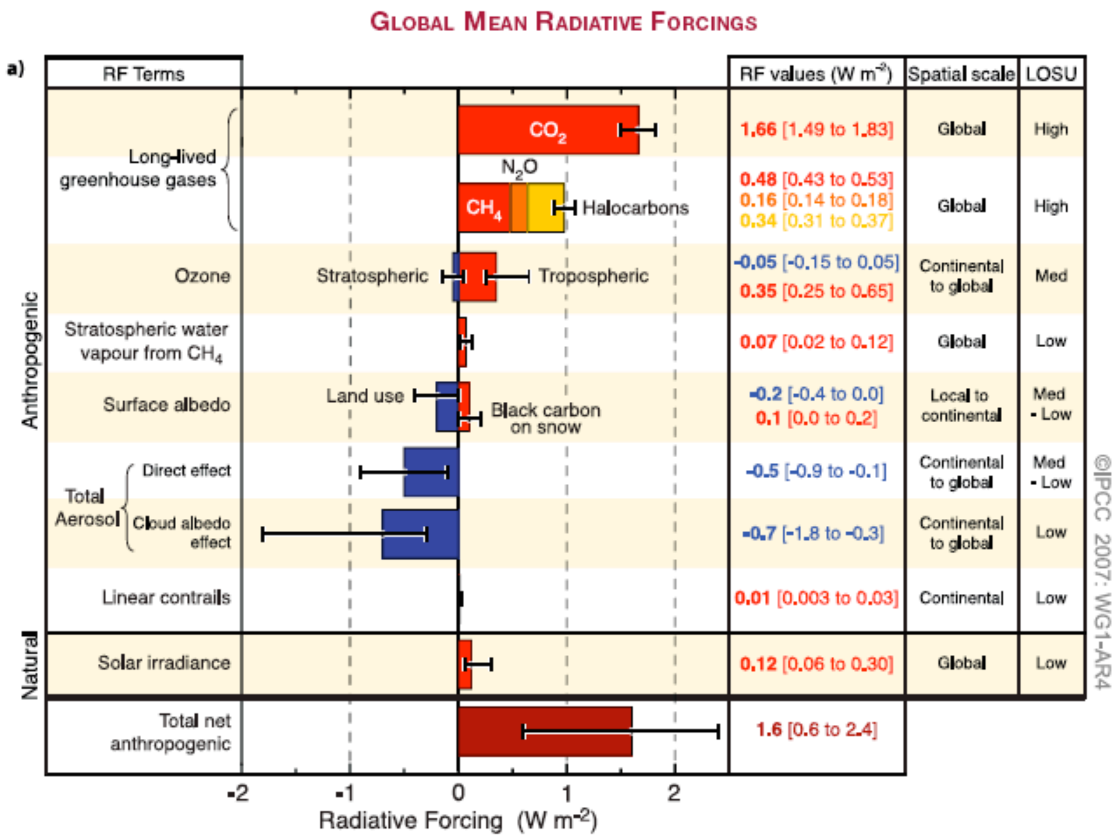

Figure 1.12 From IPCC Technical Summary (2007). Global mean radiative forcings (RF) and their 90% confidence intervals in 2005 for various agents and mechanisms. Columns on the right-hand side specify best estimates and confidence intervals (RF values); typical geographical extent of the forcing (spatial scale); and level of scientific understanding (LOSU) indicating the scientific confidence level. Errors for CH4, N2O, and halocarbons have been combined. The net anthropogenic radiative forcing and its range are also shown. Best estimates and uncertainty ranges cannot be obtained by direct addition of individual terms due to the asymmetric uncertainty ranges for some factors; the values given here were obtained from a Monte Carlo technique. Additional forcing factors not included here are considered to have a very low LOSU. Volcanic aerosols contribute an additional form of natural forcing but are not included due to their episodic nature. The range for linear contrails does not include other possible effects of aviation on cloudiness.

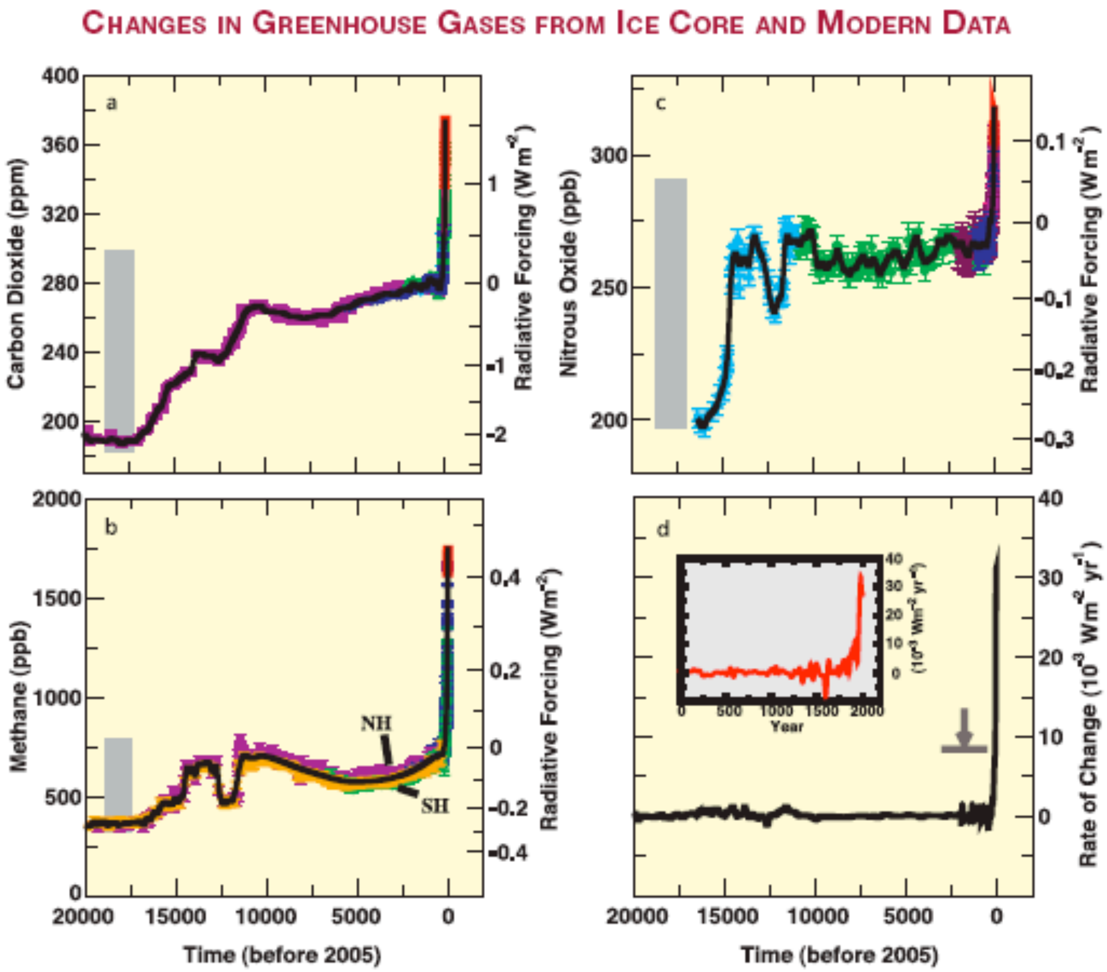

Figure 1.13 From IPCC Technical Summary (2007). The concentrations and radiative forcing by (a) carbon dioxide (CO2), (b) methane (CH4), (c) nitrous oxide (N2O), and (d) the rate of change in their combined radiative forcing over the last 20,000 years reconstructed from Antarctic and Greenland ice and firn data (symbols) and direct atmospheric measurements (panels a, b, c, red lines). The grey bars show the reconstructed ranges of natural variability for the past 650,000 years. The rate of change in radiative forcing (panel d, black line) has been computed from spline fits to the concentration data. The width of the age spread in the ice data varies from about 20 years for sites with a high accumulation of snow such as Law Dome, Antarctica, to about 200 years for low-accumulation sites such as Dome C, Antarctica. The arrow shows the peak in the rate of change in radiative forcing that would result if the anthropogenic signals of CO2, CH4, and N2O had been smoothed corresponding to conditions at the low-accumulation Dome C site. The negative rate of change in forcing around 1600 shown in the higher-resolution inset in panel d results from a CO2 decrease of about 10 ppm in the Law Dome record.

CHAPTER TWO

Data and Methodology

2.1 Data

2.1.1 Temperature Data

Temperature data used throughout this thesis come from HadCRUT3, the monthly mean combined land and marine surface temperature anomaly data set maintained by the Climatic Research Unit (CRU) at the University of East Anglia (UEA). HadCRUT3 provides temperature anomalies on a 5° by 5° latitude/longitude grid from 1850 to present (Brohan et al., 2006; Rayner et al., 2006). The anomalies are a result of *in situ* measurements of land and marine surface temperature and are calculated from mean of the base period 1961-1990. In the following paragraphs we first describe the data in further detail and then briefly review the process of combining the land and marine observations.

HadCRUT3 is a combination of gridded land-surface data from the CRUTEM3 data set and gridded SST data from the HadSST2 data set. The structure of the available data in CRUTEM3 and HadSST2 is the same. Each dataset contains monthly mean temperature anomalies, measurement and sampling error estimates, and bias error estimates for each 5° by 5° latitude/longitude gridbox (Brohan et al., 2006).

CRUTEM3 data is a collection of monthly-average temperature observations derived from a system of over four thousand homogenized, quality-controlled land surface stations around the globe. The station data has been compared with the European Center of Medium Range Weather Forecast (ECMWF) Numerical Weather Prediction (NWP) model Re Analysis (ERA-40) to isolate potentially erroneous measurements. Of more than 3.7 million monthly station values, the ERA-40 comparison resulted in the identification of only 10 gridboxes containing doubtful measurements. Visual inspection of the data records was also conducted to identify outlying values. Only 270 monthly outliers were identified and the bad values were either corrected or removed. Additionally, a check of duplicate stations has been conducted and all duplicates from the previous version of CRUTEM, 53 in total, were merged.

The HadSST2 data set contains monthly mean SST observations. SST measurements are a good surrogate for marine air temperature. They supply more useful data than marine air temperature and have smaller sampling errors (Parker et al., 1994). HadSST2 is constructed from raw *in situ* ship and buoy (moored and drifting) observations from the International Comprehensive Ocean-Atmosphere data set (ICOADS) (Diaz et al., 2002).

Large-scale bias corrections are used to adjust for inhomogeneities in the SST data. These inhomogeneities are largely due to changes in instrumentation used for SST measurements over the years (i.e. insulated wooden buckets versus uninsulated (canvas) buckets versus engine room intake measurements). In the nineteenth and early twentieth centuries uninsulated bucket measurements were largely used to measure SST. From 1939-1941 United States (US) Merchant Marine ships switched from uninsulated bucket measurements to engine room intake measurements (Folland and Parker, 1995). Thompson et al. (2008) also discovered a large-scale change in the nationality of ships at sea, and therefore the method of SST measurement utilized, related to World War II. From 1942 to August of 1945, 80% of SST observations were taken by US ships, which relied mainly on engine room intake measurements. Between late 1945 and 1949, US measurements accounted for only 30% of recorded measurements, while United Kingdom (UK) ships made up 50% of the measurements. UK ships made use of the uninsulated bucket measurement technique and thus, their measurements biased cool relative to the US engine room intake observations. Bias corrections have been made to HadSST2 to account for some but not all of these inhomogeneities over the years.

The land station data and SST data must be combined to achieve global coverage and to create the HadCRUT3 data set. The combination of these two types of data is completed in the following manner: in land-only gridboxes the land value is used, in ocean-only gridboxes the SST value is used, and in coastal and island gridboxes the land and SST values are blended (Brohan et al., 2006). Historically, these values have been blended by weighting the data by the fractional area of land and ocean in a given gridbox. The goal of this method was to place more weight on the more reliable data source; however, this method does not always result in the more reliable data source being favored.

The current data set, HadCRUT3, blends the data in a way that minimizes the uncertainty of the blended mean. This method ensures that the more reliable data source is utilized by scaling according to the uncertainty, or the combination of measurement errors and sampling errors, of both land and SST data (Brohan et al., 2006). Variance is inherent in weighting by uncertainty due to changes in data availability in time and location. However, this method more accurately allows the SST data to be favored in areas where it is expected to be reliable (i.e. the North Atlantic and North Pacific coasts, where SST observations are abundant) and allows the land data to be favored in areas where it is more reliable (i.e. in Indonesia and in the South Pacific, where SST observations are few and far between).

2.1.2 Sea Level Pressure Data

The pressure variable used throughout this thesis is monthly mean surface pressure. These data were produced by the National Centers for Environmental Prediction – National Center for Atmospheric Research (NCEP-NCAR) reanalysis project (Kalnay et al., 1996; Kistler et al., 2001). The reanalysis makes use of quality-controlled land surface, ship, rawinsonde, pibal, aircraft, satellite, and other data to produce a research quality data set. The main goal of the reanalysis project is to use a frozen analysis/forecast system and data assimilation to produce a record of global atmospheric variables. The assimilation system uses the T62 28-level NCEP global spectral model to interpolate data and is frozen from 1957-1996 to eliminate climatic jumps resulting from changes in the assimilation system over time.

The NCEP reanalysis mean surface pressure data is available from 1948 to the present on 2.5° by 2.5° latitude/longitude gridboxes. The atmospheric variables included in the reanalysis were separated into four classes based on the degree to which they were influenced by observations and/or the model. Class A variables are the most reliable and are strongly influenced by observed data. Upper-air temperature and wind are good examples of Class A variables. Class B variables are directly affected by observational data, but are also strongly influenced by the model. Humidity and surface temperature are good examples of Class B variables. Class C variables are not directly affected by observations. Alternatively, they are derived exclusively from model fields forced by data assimilation. Examples of Class C variables include: clouds, precipitation, and surface fluxes. Finally, Class D variables are climatological and do not depend on the model at all. Surface roughness is a good example of a Class D variable. Surface pressure falls into the Class B categorization. Careful interpretation of the results should be utilized for any analysis using Class B and Class C variables since model input is involved.

2.1.3 Sea Ice Data

The final data set used in this thesis is that for sea ice concentration. Global sea ice content was obtained from the HadISST ICE, Version 1.1 database, provided by the Met Office Hadley Centre. HadISST ICE, Version 1.1, contains monthly 1° by 1° grids of SST and sea ice concentration, given as a percent coverage out of 100%, from 1870 to the present. The sea ice concentration data will be the focus of this discussion. Both *in situ* observations and satellite-derived estimates of sea ice concentration are present in the data.

Prior to 1978, historical sea ice extent and concentration charts form the basis of HadISST ICE. The following digitized sea ice charts were combined in the data set: the Walsh Northern Hemisphere Sea Ice Concentration Charts (Walsh, 1978), the Great Lakes Fields (Assel, 1983), the Antarctic Atlas Climatologies (Deutsches Hydrographisches Institute, 1950; Tolstikov, 1966), and the National Ice Center Charts for Both Hemispheres (Knight, 1984). Some of these charts include measures of sea ice extent (total areal coverage by sea ice), while others contain sea ice concentrations (the relative fraction of sea ice per gridbox). The sea ice concentration measure is more applicable in climate studies; thus, in some cases climatological seasonal sea ice gradients and interpolations were used to translate sea ice extent into sea ice concentration for the HadISST ICE data set (Rayner et al., 2003).

After 1978 passive microwave retrievals and surface observations are blended in HadISST ICE (Rayner et al, 2003). Satellites used for this data collection are operational under the Defense Meteorological Satellite Program (DMSP). Retrievals from the Scanning Multichannel Microwave Radiometer (SMMR) are available every other day from October 25, 1978 until July/August 1987 and retrievals from the Special Sensor Microwave/Imager (SSM/I) are available thereafter. The SSM/I is a seven-channel passive microwave radiometer that operates at four frequencies and dual-polarization. Sea ice concentration datasets formed from these retrievals will have different characteristics depending on the algorithm used and the method for filtering out weather noise. The algorithm used in HadISST ICE is the NASA Team Algorithm from the Goddard Space Flight Center (GSFC). The NASA Team Algorithm gives a long, homogenized, and readily available record of sea ice concentration for both hemispheres (Rayner et al., 2003).

The sea ice concentration data sets have many inconsistencies. Most of these inconsistencies are caused by large differences in methods and locations of sea ice data collection and are concentrated in the earlier part of the record. By the late 1970s, once satellite measurements were introduced, the inconsistencies in sea ice data were greatly minimized and the record was homogenized. However, it is important to note that satellite measurements are not free of errors or bias. A distinct disadvantage to using satellites is that they are unable to gather data at the surface in cloudy regions. Satellite retrievals often present a cold bias in partly cloudy regions, due to the colder temperature of cloud tops in comparison to the surface. These biases can be lessened, but not completely removed. *In situ* measurements thus become very important for validation and calibration of satellites. The combination of both types of observations, *in situ* and satellite-based, results in more accurate surface data records. Sea ice concentrations used throughout this thesis will be focused on the more reliable combination of *in situ* and satellite data from 1979 onward.

It should be noted that as of December 2010 a significant degradation in performance in the SSM/I satellite was discovered. The month of January 2009 was most affected and likely resulted in an underestimate of ice extent and concentration (Met Office, 2006). SSM/I products were suspended as of November

2009 and have been replaced with Special Sensor Microwave Imager Sounder (SSMIS) satellite data. As of December 3, 2010, the Met Office Hadley Centre has reprocessed data from January 2009 to the present; however, the switch in data may cause a discontinuity in the record at the beginning of 2009.

2.2 Methodology

Our analysis investigates variability in global mean temperatures on a range of timescales, including trends in temperature for both the Northern (30°-90°N) and Southern Hemisphere (30°-90°S). In hemispheric-specific sections the analysis may be limited to smaller latitudinal restrictions (i.e. 40°-90°, 50°-90°, 60°-90°, and 70°-90°) to verify trends. The analysis will focus on trends from temperature data from 1979 to December 2010. These dates were chosen because data used for comparison (i.e. sea level pressure and sea ice concentration) are partially derived from satellite observations, which are available beginning in 1979.

In all analyses the seasonal cycle has been removed from the data (temperature, surface pressure, and sea ice concentration) by subtracting the monthly mean over the period of analysis from each data point. Correlations are therefore not due to the shared seasonal cycle in the time series. Temperatures were originally given in anomaly form. However, new temperature anomalies are formed to correspond with the period of record that is under analysis, most often 1979-2010. Since observational data is not available at every gridpoint during every month the statistics tools used for analysis will only be used at gridpoints where fifty percent or more of the data are available over the period of analysis.

We explore variability in global mean temperature by investigating variability on different timescales and by isolating variability in the Northern and Southern Hemispheres. To identify such variability we will make extensive use of statistical tools such as filtering, regressions, and correlations, each of which will be described in further detail below.

2.2.1Temporal Filtering

The goal of filtering is to remove or retain certain frequencies from a time series. A low pass filter acts to retain low frequencies and a high pass filter acts to retain high frequencies. Intermediary frequencies can be isolated by a band pass filter. The general idea of filtering comes from spectral analysis (which is based on interpreting a time or space series as a summation of contributions form harmonic functions, each with unique temporal or spatial scales). In spectral analysis,

$$y(t) = \bar{y} + \sum_{k=1}^{N/2} C(\omega_k) \bullet \cos(2\pi k \frac{t}{T} - \phi_k)\ , \qquad (2.1)$$

where t is time, T is the period of record, N is the number of time steps (which is one time step longer than T), k is the wavenumber, $\frac{N}{2}$ is the Nyquist frequency (or highest resolvable frequency), $\bar{y}$ is the mean of the function from wavenumber $k \rightarrow \frac{N}{2}$, C is the sum of the amplitudes of the harmonic functions as a function of

ω_k (frequency), and ϕ_k is a red noise power spectrum. The filtered version of $y(t)$ is as follows,

$$y(t) = \bar{y} + \sum_{k=1}^{N/2} R(\omega_k) \bullet C(\omega_k) \bullet \cos(2\pi k \frac{t}{T} - \phi_k), \qquad (2.2)$$

where all variables remain the same as in equation 2.1. The only additional variable in equation 2.2 is the response function ($R(\omega_k)$) of the filter. The response function is equal to the amplitude of the filtered time series at a given frequency (ω) over the amplitude of the input time series at the same frequency (ω).

Filtering in the time domain involves use of the centered weighting method, where a time series is subjected to a weighted running average. This means that a data point is a weighted mean of the surrounding data points. The operation in equation 2.3 is a low-pass filter.

$$g(t) = \sum_{i=-J}^{+J} f(t + i\Delta t) \bullet w(i) \qquad (2.3)$$

In equation 2.3, *g* is the output, or the low pass filtered time series, *J* is the length of the window, *t* is time, Δt is the time resolution of the data, *f* is the input time series, and *w* is the weighting function in the time domain (centered weighting). The high pass filtered time series can be found by subtracting the low pass filtered series (g) from the input series (f).

The Butterworth Filter is the filter of choice for this thesis. The Butterworth Filter is a recursive filter, which means that the weighting function used acts on both prior values of the input and filtered data. Like many recursive filters the Butterworth Filter yields response functions with sharp cutoffs for relatively short weighting functions. The response function for the Butterworth Filter can be seen in equation 2.4.

$$\left|R^2(\omega)\right| = R(\omega) \bullet R^*(\omega) = \frac{1}{1+\left(\frac{\omega}{\omega_c}\right)^{2N}} \tag{2.4}$$

In the above, $\left|R^2(\omega)\right|$ represents the amplitude of the response function, $R(\omega)$ is the response function, $R^*(\omega)$ is the complex conjugate of the response function, ω is the frequency, ω_c is the cut-off frequency, and N+1 is the number of weights. Higher values of N result in a sharper cut-off frequency, which is desirable because it lessens spectral leakage. Note that the response function operates in the frequency domain while the weighting function operates in the time domain. The two are a Fourier transform pair.

2.2.2 Linear Regression

The basic idea behind regression analysis is to estimate a variable *y* based on known values of another variable *x*. Regression analysis results in the slope of a line and is represented by a_1 in the following equation, $\hat{y} = a_1 x + a_0$, where $\hat{y}$ is the estimate of the observed *y* based on a linear relationship with the independent variable *x*. This slope (a_1) is the slope that produces the smallest error in estimating the observed data. To solve for a_0 and a_1 a second equation is needed. An error function (*Q*) can be defined using the least squares method, where $Q = \sum_{i=1}^{N}\left(\hat{y}_i - y_i\right)^2 = \sum_{i=1}^{N}\left(a_1 x_i + a_0 - y_i\right)^2$. When *Q* is minimized, two equations with two unknowns (a_0 and a_1) are left. Solving for a_1 leaves the slope of a line, or the regression coefficient, which is the covariance over the variance in x:

$$a_1 = \frac{\overline{x'y'}}{\overline{x'^2}} \qquad (2.5)$$

2.2.3 Correlation

The correlation coefficient measures the interdependence of two variables. The correlation coefficient *r* is equal to the square root of the fraction of variance in *y* explained by *x*:

$$r = \frac{\overline{x'y'}}{\sigma_x \sigma_y} \qquad (2.6)$$

The correlation coefficient *r* varies from -1 to 1, with -1 being perfectly anti-correlated, 0 being uncorrelated, and 1 being perfectly correlated. The correlation coefficient (*r*) is only valid for linear relationships. It will not reveal quadrature relationships since the correlation between sine and cosine is zero. To elucidate these sorts of relationships lag correlations must be used. It is also important to note that correlations do not reveal cause and effect. Theoretical understanding must be used to interpret the meaning of a correlation. The square of the correlation coefficient, r^2, is the explained variance by the linear fit to *x* ($a_1x + a_0$) over the total variance in *y*, or in other words, the variance in the estimate $\hat{y}$ over the total variance in *y* (r^2 varies from 0 to 1).

CHAPTER THREE

Filtering the Global Mean Temperature Time Series

The primary objective of this thesis is to extend previous analyses that have removed sources of known variance from the record of global mean temperature. It is known that variance in global mean temperature is present on many different temporal scales. Before we remove a specific source of variance in the following chapter we first explore the amount of variance that is present in the global mean temperature time series on scales of less than one year, one to ten years, and greater than 10 years.

3.1 Filtering the Global Time Series

We will look at variability in global mean temperature at different timescales and will isolate variability in both the Northern (NH) and Southern (SH) Hemispheres.

3.1.1 Decomposing Global Mean Temperature into 3 Frequency Bands

To begin the analysis a global mean temperature time series was formed for the years 1850-2010. This was done by cosine-weighting the monthly mean HadCRUT3 temperature anomalies by latitude and finding the global mean temperature for each month. The global mean temperature time series is shown in Figure 3.1 (top time series).

After calculating the global mean temperature time series for 1850-2010, we wish to investigate the time series of global mean temperature at different temporal scales. Thus, a Butterworth Filter was run over the global mean temperature series. A low-pass filter with a cut-off frequency of 1/120 cycles per year was used to isolate global mean temperature variations on scales greater than 10 years. Another filter, which we will refer to as the band-pass filter, with a cut-off frequency of 1/12 cycles per year, was used to isolate variations in global mean temperature for timescales great than 1 year.

With the aforementioned filters, time series of global mean temperature containing variation with periods of greater than 10 years, 1-10 years, and less than 1 year were formed. The global mean temperature time series for periods of greater than 10 years was formed directly from the low-pass filter of the global mean temperature time series. The time series for periods of 1-10 years was found by taking the difference between the full global mean temperature series minus the low-pass filtered global mean temperature and the full global mean temperature minus the band-pass filtered global mean temperature. And finally, the time series for periods less than 1 year was found by subtracting the band-pass filtered series from the full global mean temperature time series.

Figure 3.1 shows the results of the filtering of global-mean temperature. Note that the long-term upward trend in global mean temperature is – by construction - only visible in the time series that includes variations of 10 years and more. Also by construction, the time series for 1-10 years contains interannual variations, and the bottom time series, which contains variations of less than a year, exhibits the highest frequency variations.

Tables 3.1 and 3.2 display the correlation coefficients and variance explained for the times series in Figure 3.1 as they relate to the full global mean surface temperature time series. Tables are located after figures at the end of the chapter. The time series that retains interdecadal variations (greater than 10 years) is most highly correlated with the full global mean temperature time series (r=0.86). These time series explain 75% of the variance (r^2= 0.75) in one another. The following two filtered time series, which contain interannual and intraannual variations respectively, explain roughly 12% of the total variance in global mean temperature each, and vice versa. The standard deviation of each of these time series can be seen in Table 3.3 under the global heading. The standard deviation of the interdecadal time series is nearly as large as the full time series, while the standard deviations of the two remaining series are much less.

3.1.2 Correlations of Surface Temperature with Global Mean Temperature

We will now examine the patterns of surface temperature variability associated with variations in global mean temperature on the frequency bands used in Figure 3.1. To do this we correlate global surface temperature anomalies with global mean temperature at each gridpoint for the period 1979-2010. This time period was chosen since 1) the data are most complete over the past few decades, and 2) we will later be comparing results with those derived from satellite observations, which are only available beginning in 1979.

Figure 3.2 shows the results of correlating global surface temperature anomalies with the full global mean temperature time series in the top of Figure 3.1. There are high positive correlations in the NH, particularly over the continents and the North Atlantic. Most ocean areas show a neutral or negative correlation between surface temperature anomalies and global mean temperature. This general pattern in temperature difference between land and ocean is expected due to the large difference in heat capacity between landmasses and ocean. The pattern that results from the difference in heat capacity between land (low heat capacity) and ocean (high heat capacity) is often referred to as the Cold Ocean-Warm Land (COWL) pattern, as discussed in the introduction. As circulation patterns change, for example, in different phases of the North Atlantic Oscillation, the surface temperature field is influenced by advection (Hurrell, 1995; Wallace et al., 1995; Wallace et al., 1996). The low heat capacity of land allows the continents to respond rapidly and strongly to advection; the relatively high heat capacity of the oceans renders them less sensitive to temperature advection. Thus, months characterized by anomalous warm advection over land and cool advection over the oceans are marked by anomalously high global mean temperatures, and vice versa.

In addition to displaying the COWL pattern Figure 3.2 displays attributes of other climatic patterns and phenomena. The warming in the North Atlantic indicates that variability in this area is likely important for long-term SST variability. The area of contrasting temperatures in the North Pacific shows signs of the Pacific

Decadal Oscillation (PDO), an El Niño-like climate pattern that occurs on interdecadal timescales and will be discussed in more detail below (Mantua et al., 1997; Zhang et al., 1997). No signatures of El Niño–Southern Oscillation (ENSO) are apparent across the equatorial Pacific in Figure 3.2.

Distinct differences were seen in the patterns in Figure 3.2 when the global mean temperature time series was filtered before calculating the correlation coefficients. To see what each of the timescales (greater than 10 years, 1-10 years, and less than 1 year) explains in the patterns seen in Figure 3.2 we calculated correlations between surface temperature anomalies with each of the three filtered global mean temperature time series. The resulting patterns can be seen in Figure 3.3. There are nine map views in Figure 3.3. Each column contains one map, but from three different views: North Pole, global, and South Pole. The first column contains data that was correlated with global mean temperature containing variability greater than 10 years. The second column contains data correlated with global mean temperature containing variability from 1-10 years. And the third column contains data that was correlated with global mean temperature containing variability of less than 1 year.

The patterns in Figure 3.3 help to explain what is seen in the full global mean temperature correlations in Figure 3.2 more clearly. While looking at Figure 3.3, it should be noted that the correlations that involve decadal variations in global mean temperature are based on relatively fewer degrees of freedom than the other correlations for shorter timescales with more frequent sampling. It is easiest to describe the most important map features in Figure 3.3 by looking at each of the three correlation maps one at a time. For surface temperature anomalies correlated with filtered global mean temperature the most noticeable features are discussed for each scale of variability below.

- Greater than 10 years: The interdecadal timescale contains some of the highest positive correlations across all maps, which is noteworthy since this is also the scale at which the signature of anthropogenic warming presents itself. The high positive correlations are located over the North Atlantic. This strong surface temperature warming suggests that the North Atlantic is very important in terms of long-term SST variability, and therefore, in global mean temperature variability. There is also potential for this warming to be a sign of the Atlantic Multidecadal Oscillation (AMO), an interdecadal mode of variability in the SST field. We are currently in a warm phase of the AMO (Schlesinger et al., 1994).

  The interdecadal timescale also shows a large area of warming over the western Pacific and cooling over the eastern Pacific. This cooling over the eastern Pacific is the opposite of what one would expect from ENSO. It is likely a result of the ENSO-like pattern of climate variability called the PDO, which occurs on interdecadal timescales (Mantua et al., 1997; Zhang et al., 1997). The PDO is a pattern of ocean-atmosphere climate variability in the midlatitude Pacific Ocean. The PDO switches polarity roughly every 20-30 years and the most recent epoch has been characterized by lower sea level pressure (SLP) over the North Pacific. The lower SLP has been associated with stronger westerlies at 40°N, which favors enhance sea-air fluxes and lower SST (Mantua et al., 1997).

- 1-10 years: While ENSO was not evident in Figure 3.2 it is quite obvious in Figure 3.3. The large area of warming in the equatorial Pacific is a signature of ENSO. ENSO releases heat into the atmosphere in the tropical Pacific through latent and sensible heat fluxes (Yulaleva and Wallace, 1994). From 1950-1998 ENSO accounted for 0.06°C of the global surface temperature increase (Wigley, 2000; Santer et al., 2001; Trenberth et al., 2002). The typical ENSO period ranges from 3-8 years, which coincides nicely with global mean temperature variability from 1-10 years (Blanke et al., 1997; Trenberth et al., 2002).
- Less than 1 year: While some warming over the continents is noticeable in the first column, where filtered global mean temperature with variability greater than 10 years is used, most of the continental warming is present on the shortest timescale. Positive correlations, or warming, are confined almost exclusively to continental areas in the third column in Figure 3.3, where global mean temperature variability of less than 1 year is used. These patterns are a signature of the difference in heat capacity between land and water, or the COWL pattern, which mainly develops on intraannual timescales (Wallace et al., 1995; Broccoli et al., 1998). These patterns can also be related to snow cover and a resultant albedo effect.

It is interesting to note that the out of phase signals in the Pacific, i.e. the ENSO signal in the 1-10 year timescale and the PDO signal in the greater than 10 year timescale, act to cancel each other out for the most part. This is the reason why the ENSO signal is obscured in the full correlation in Figure 3.2.

3.1.3 Correlations of Sea Level Pressure with Global Mean Temperature

Here we examine the patterns of variability in SLP associated with variability in global mean temperature in a manner similar to that done above. SLP is closely tied to patterns of surface temperature variability because it describes the near surface circulation. Gradients in SLP create wind that advects air of different temperatures from place to place. Conversely, SLP can also be influenced by temperature advection. Areas of higher temperature, or higher thickness, are generally associated with rising air and lower surface pressure, while areas of colder temperature, or lower thickness, are associated with sinking air and higher surface pressure.

Figure 3.4 illustrates the results of correlating SLP anomalies with global mean temperature. The patterns involved are similar to those seen in Figure 3.2; however, most correlations are opposite in sign to those in Figure 3.2 due to the relationship between temperature and pressure. It seems that one may cause or influence the other, i.e. SLP indicates the direction of surface flow and thus the advection of air of differing temperature. Notice that the correlations over the NH continents are now largely negative, as opposed to positive in Figure 3.2. This is likely due to the fact that the warming over the NH continents is driving low surface pressure. The ocean areas are generally neutral or positively correlated with global mean temperature.

As was done with surface temperature we also examine how the patterns of correlations of SLP with global mean temperature change on different temporal scales. Figure 3.5 shows the results of these correlations. As in Figure 3.3, each column contains one map, but from three different views: North Pole, global, and South Pole. The first column contains data that was correlated with global mean temperature containing variability greater than 10 years. The second column contains data correlated with global mean temperature containing variability from 1-10 years. And the third column contains data that was correlated with global mean temperature containing variability of less than 1 year. For SLP anomalies correlated with filtered global mean temperature with variability . . .

- Greater than 10 years: The interdecadal timescale accounts for some of the positive correlations in the Pacific in the global map in Figure 3.4. The large positive correlations over the eastern Pacific are indicative of the PDO. This area of high pressure, which stretches up the coast of North America helps explain the large area of cooler surface temperatures present in the Pacific on the interdecadal surface temperature correlation map in Figure 3.3.
- 1-10 years: The SLP correlations on timescales of 1-10 years clearly show signs of ENSO, with a large dipole in pressure variations across the equatorial Pacific (Blanke et al., 1997; Yulaleva and Wallace, 1994; Trenberth et al., 2002). Lower pressures accompany warm water in the eastern equatorial Pacific and higher pressures can be seen in the cooler western equatorial Pacific. This pressure configuration aids latent and sensible heat fluxes in the eastern Pacific and contributes to surface temperature increases in that area

(Yulaleva and Wallace, 1994). It is also interesting to notice that the lower pressure over North America is fairly evenly split between interannual and intraannual scales. This suggests that ENSO teleconnections play a role in North America.

- Less than 1 year: The intraannual timescale appears to be the largest contributor to negative SLP correlations over Eurasia. This is consistent with the surface temperature correlation results, where most of the continental warming is present on the shortest timescale. The location of the negative SLP correlations over Eurasia is ideal for warm air advection over the region. As in Figure 3.3, where warming was confined almost exclusively to continental areas, the area of low pressure in the intraannual scale in Figure 3.5 is largely confined to the NH continents. These configurations represent the COWL pattern (Wallace et al., 1995; Broccoli et al., 1998).

3.2 Filtering the Time Series by Hemisphere

The analyses in Section 3.1 focus exclusively on global mean surface temperature. Here we examine variability in surface temperature and SLP and how they relate to mean temperature by hemisphere. Thus, a NH mean temperature time series and SH mean temperature time series were created in the same fashion as the global mean temperature time series in Section 3.1. We used HadCRUT3 temperature anomalies from 30°-90°N to form a NH mean temperature time series and temperature anomalies from 30°-90°S to form SH mean temperature anomalies. Butterworth filters with the same cut-off frequencies for low and band-pass filters, 1/120 and 1/12 respectively, were used and filtered times series for periods of greater than 10 years, 1-10 years, and less than 1 year were formed for both the NH and SH.

3.2.1 Northern Hemisphere

The NH time series and filtered NH time series can be seen in Figure 3.6. The general features in the time series are similar to those seen in Figure 3.1. The NH mean temperature series filtered to include variations over 10 years clearly shows warming over the length of the available data and explains the overall trend. The third and fourth time series show variations on interannual and intraannual scales, respectively. The intraannual time series explains more of the variability in the full NH mean temperature series than either of the other filtered time series. Correlation coefficients and variance explained for the NH mean temperature time series can be seen in Table 3.1 and 3.2. The intraannual time series explains 43% of the variance in the full NH time series, while the interdecadal time series explains 35% and the interannual time series explains 17% of the variance. The standard deviation of each of these time series can be seen in Table 3.3 under the NH heading.

It is interesting to look at how closely correlated the global mean temperature time series and NH mean temperature time series are with each other. Table 3.4 shows that they have a correlation of 0.81. Thus, the NH mean temperature time series and global mean temperature time series explain 65% of the variance in one another (Table 3.5). The interdecadal time series are the most highly correlated with r=0.94. This means that the NH mean temperature time series filtered for variability greater than 10 years explains 89% of the variance in its filtered counterpart for the global mean temperature time series. Conversely, the global mean temperature time series explains 89% of the variance in the NH mean temperature time series.

3.2.2 Correlations of Surface Temperature with NH Mean Temperature

Figure 3.7 shows the correlation between surface temperature anomalies and the NH mean temperature time series. Use of the NH mean temperature time series highlights the warming over the NH landmasses. Correlations in Figure 3.7 are much higher than those found using the global mean temperature time series in Figure 3.2, especially over Eurasia. The negative correlations off of the western coast of North America are similar in magnitude in both Figure 3.2 and 3.7.

In looking at the maps in Figure 3.8 it can be seen that much of the high positive correlations are found in the far right column, which shows the map for correlations with NH mean temperature containing intraannual variability. This means that surface temperatures are correlated most closely with NH mean temperature on intraannual scales. This is a distinct signature of the COWL pattern (Wallace et al., 1995; Broccoli et al., 1998). It is interesting to note that ENSO signals are not apparent in Figure 3.8 as they are in Figure 3.3. ENSO does not have a noticeable impact on large-scale temperatures when the NH mean temperature is used as a baseline; however, it does play a role when the entire globe is considered. And finally, the map retaining interdecadal NH mean temperature variability shows a large area of cooling over the Pacific. This cooling appears to be in the opposite sense of ENSO and is a signal of the PDO (Mantua et al., 1997). The North Atlantic shows warming that is reminiscent of the interdecadal map in Figure 3.3. This indicates that the North Atlantic long-term SST variability is important even if only the NH mean temperature time series is considered.

3.2.3 Correlations of Sea Level Pressure with NH Mean Temperature

NH mean temperature correlations with SLP are shown in Figure 3.9. As expected, the negative correlations over Eurasia are larger in comparison to the global mean temperature maps in Figure 3.4. The correlations in Figure 3.9 are high and indicate areas of warm temperature advection over much of northern Asia. When the NH mean correlations are filtered in Figure 3.10 it becomes evident that a majority of the variability in SLP over the NH continents stems from variability on periods of less than one year, as is the case for surface temperature in Figure 3.8. This pressure pattern leads to the advection of warm air over Eurasia, which is seen as an area of large positive correlations in Figure 3.8. These configurations are consistent with the COWL pattern.

The map relating SLP to NH mean temperature in Figure 3.9 shows more amplitude in the equatorial Pacific than the map using global mean temperature in Figure 3.4. The large area of positive correlations over the eastern equatorial Pacific in Figure 3.9 mostly stems from decadal variability, as can be seen in the first column in Figure 3.10, and is indicative of the PDO. There is a very weak signal, and arguably no signal, of ENSO in the interannual timescale map. This reinforces the findings from Figure 3.8 that large-scale temperatures, or pressures in this case, are not impacted by ENSO when the NH mean temperature is used as a baseline.

3.2.4 Southern Hemisphere

Just as temperatures were isolated for the NH mean, we also isolate and examine temperatures for the SH mean. The time series of SH mean temperature can be seen at the top of Figure 3.11 followed by the filtered SH mean temperature time series. The general features, like those for the NH, are similar to those seen in Figure 3.1. The SH mean temperature times series filtered to include variations over 10 years shows warming over the length of the available data and by construction includes the overall trend. The third and fourth time series show variations on interannual and intraannual scales, respectively. The intraannual time series contains the highest frequency variability. Unlike the NH mean temperature time series, the interdecadal time series explains most of the variability in the full SH mean temperature series. The interdecadal global mean temperature time series and SH mean temperature time series explain 72% of the variability in one another, which is similar to the full global mean temperature case. This finding is consistent with the fact that the SH contains more ocean than the NH and thus, has less intraannual variability. As before, correlation coefficients and variance explained for the SH mean temperature time series can be seen in Table 3.1 and 3.2. The other two time series, interannual and intraannual, explain 10% and 19% of the variability in SH mean temperature, respectively. The standard deviation of each of these time series can be seen in Table 3.3 under the SH heading.

It is interesting to look at how closely correlated the global mean temperature time series and SH mean temperature time series are with each other. Table 3.4 shows that they have a correlation of 0.72. Thus, the SH mean temperature and global mean temperature time series explain 51% of the variance in one another (Table 3.5). The interdecadal time series are the most highly correlated with r=0.89. This means that the SH mean temperature time series filtered for variability greater than 10 years explains 79% of the variance in its filtered counterpart for the global mean temperature time series, and vice versa. Overall, the SH mean temperature time series is less well correlated with global mean temperature than the NH mean temperature time series is. Now that both NH and SH mean temperature time series and their filtered time series have been calculated the hemispheric time series can be compared with each other. These results can be seen in Table 3.6 and 3.7.

3.2.5 Correlations of Surface Temperature with SH Mean Temperature

Figure 3.12 shows the correlation between surface temperature anomalies and the SH mean temperature time series. The maximum correlations found using the SH mean temperature time series are lower than those seen in the NH case. The most obvious area of interest in Figure 3.12 is the area over the eastern Pacific. The largest magnitude correlations are located there and they are negative. This area of negative correlation is also present in Figure 3.2 and 3.7, where the magnitude of the correlation is somewhat larger. Thus, while SH mean temperature is most closely correlated with this area of the Pacific, the NH mean temperature is even more closely correlated with surface temperature changes in this region.

The three filtered SH mean temperature time series and their correlations with surface temperature are shown in Figure 3.13. It can be seen that the area of negative correlation in the Pacific stems mainly from variations on decadal scales. Again, this is likely the signature of the PDO (Mantua et al., 1997). It is interesting to note that ENSO signals are not evident in the SH mean temperature correlations, nor were they in NH mean temperature correlations. ENSO does not have a noticeable impact on large-scale temperatures when the NH or SH mean temperature is used as a baseline; however, it does play a role when the entire globe is considered. There are no noticeable areas of interest on the map containing variability for less than a year. It is likely that a COWL pattern does not present itself here due to the lack of land sea-contrast in the SH.

3.2.6 Correlations of Sea Level Pressure with SH Mean Temperature

SH mean temperature correlations with SLP can be seen in Figure 3.14. The largest correlations in this map are found in the Pacific region. Positive correlations are present in the eastern Pacific and negative correlations are present in the western Pacific. These correlations stem largely from variations on decadal timescales, likely related to the PDO (Mantua et al, 1997). This can be seen more clearly in the first column of Figure 3.15, which was created by using SH mean temperature with variability greater than 10 years. The area of positive correlation indicates increasing pressure with increasing temperature, and the negative correlation indicates falling pressure with increasing temperature. There are also areas of fairly high correlations, both positive and negative, over Antarctica in the interdecadal map. The other timescales, interannual and intraannual, show fairly low correlations across the globe.

3.3 Summary of Results

This chapter has taken an in-depth look at the structures that drive global mean temperature variability on a range of timescales. To conclude the chapter, we will discuss a few key points.

- **Global mean temperature variability is linked to various climate patterns and phenomena that occur on many different timescales.** Throughout this chapter we identified signatures of the PDO, ENSO, and the COWL pattern. Each of these patterns occurs on a distinct timescale and appeared in the appropriately filtered correlation map. For example, the PDO, which has a timescale of 20-30 years, always appeared most strongly in the interdecadal correlation maps. ENSO, which has a period of 3-8 years, presented itself in the interannual maps. And the COWL pattern, which occurs on smaller timescales related to advection, was ever present in the intraannual maps.

  It is important to analyze the different timescales of global mean temperature variability, because some sources of variability are missed in the full correlations maps. For example, the PDO and ENSO signatures often canceled each other out in correlations using the full global mean temperature time series.

- **The NH continents have the potential to greatly influence global surface temperatures on high frequency timescales, more so than any other region of the globe.** The strongest positive correlations in this chapter were found between NH mean temperature and surface temperature over the NH continents. The strongest negative correlations were found between NH mean temperature and SLP over the NH continents. These correlations were strongest for periods of less than one year, or on intraannual scales. While these correlations were highest when the NH mean temperature time series was used as a baseline, they were still present when global mean temperature was used.
- **Some sources of temperature variability are only influential on the global scale.** ENSO is a well-known atmospheric phenomenon and only presented itself in global correlation maps. When the NH and SH mean temperature correlations were calculated the ENSO signal was absent.

As we move into the next chapter we will look more closely at sea ice and global temperatures to see if patterns similar to those found here present themselves.

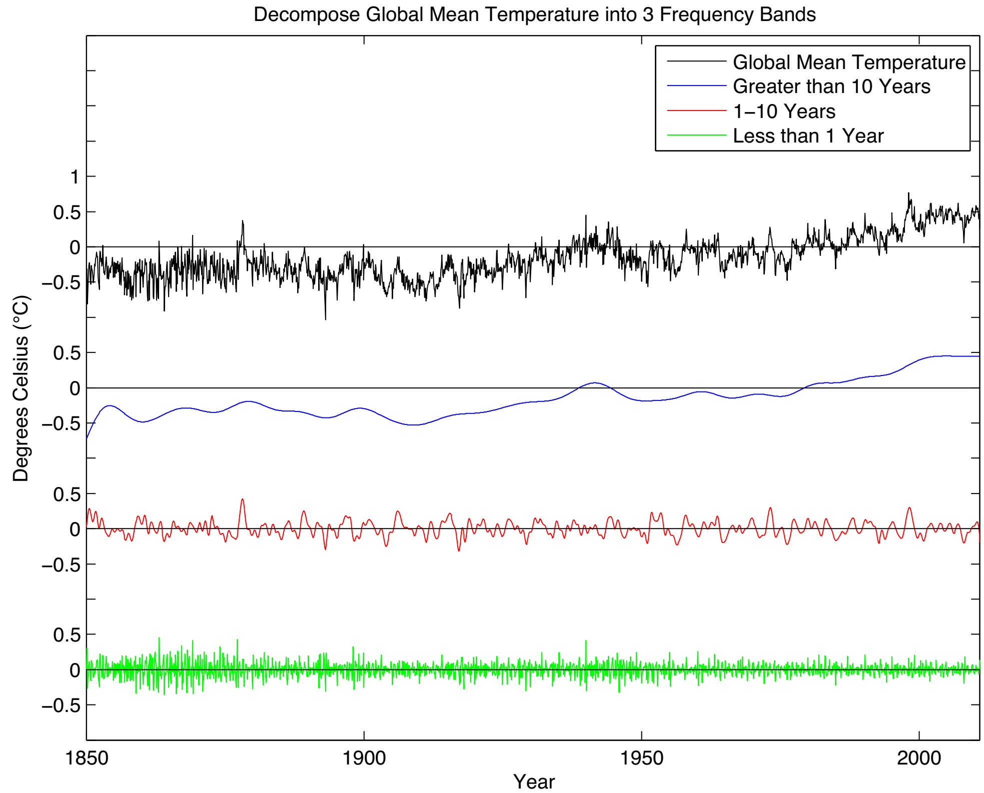

Figure 3.1 Time series of global mean temperature from 1850-2010 (top). The bottom three series are time series of filtered global mean temperature showing variability on scales of greater than 10 years, 1-10 years, and less than one year, respectively.

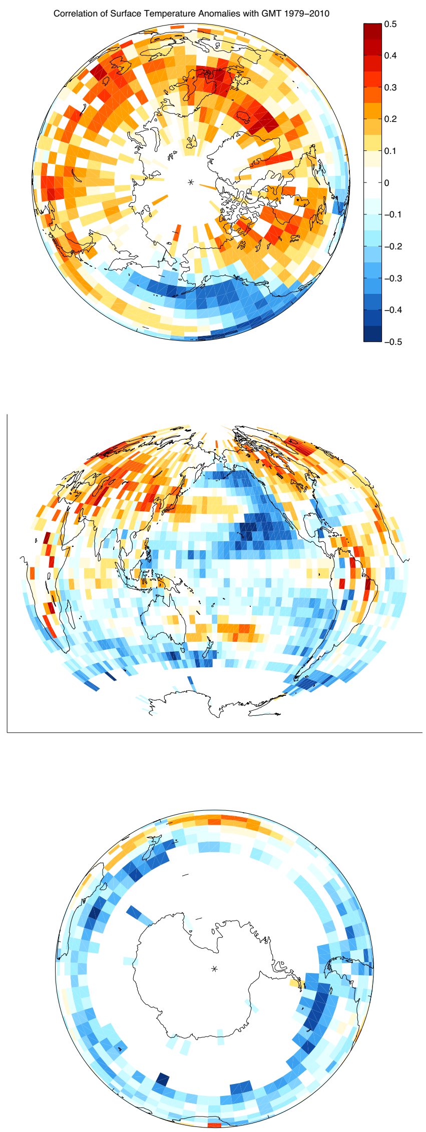

Figure 3.2 Correlation by gridspace of surface temperature anomalies with global mean temperature from 1979-2010. From top to bottom views include polar (north), global, and polar (south). Correlations can range from -1 to 1.

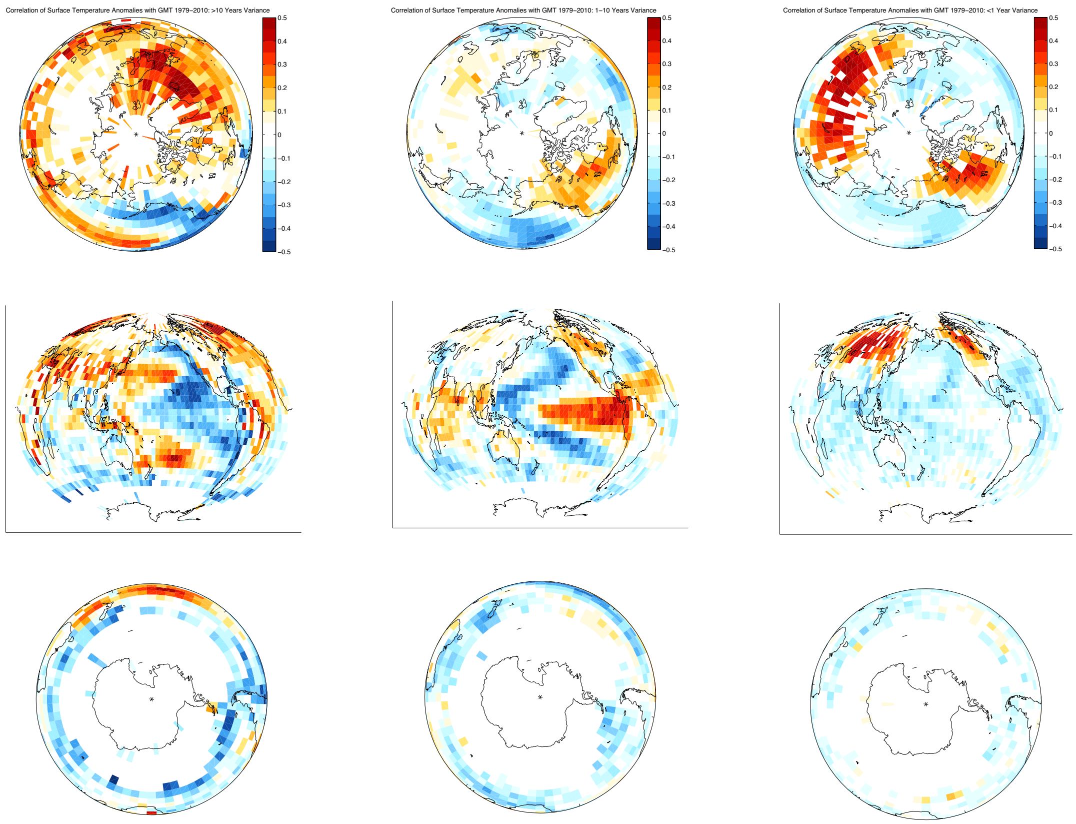

Figure 3.3 Correlation by gridspace of surface temperature anomalies with filtered global mean temperature from 1979-2010. The first column shows the correlation of filtered global mean temperature with variability greater than 10 years, the second column with variability from 1-10 years, and the third colum with variability of less than one year. From top to bottom views include polar (north), global, and polar (south). Correlations can range from -1 to 1.

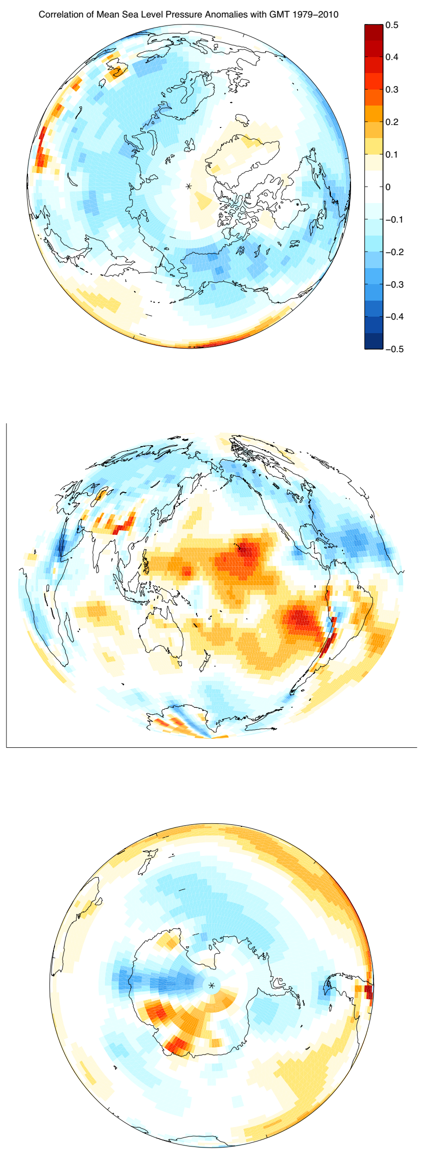

Figure 3.4 Correlation by gridspace of sea level pressure anomalies with global mean temperature. From top to bottom views include polar (north), global, and polar (south). Correlations can range from -1 to 1.

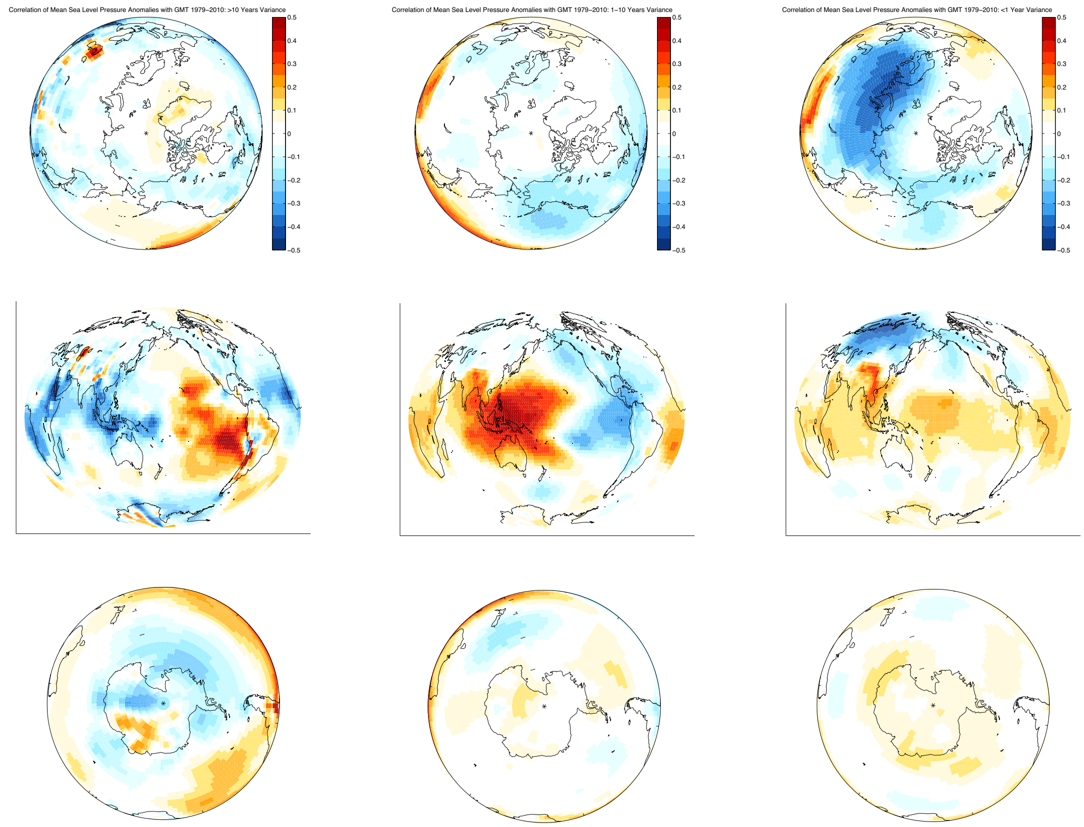

Figure 3.5 Correlation by gridspace of sea level pressure anomalies with filtered global mean temperature from 1979-2010. The first column shows the correlation of filtered global mean temperature with variability greater than 10 years, the second column with variability from 1-10 years, and the third colum with variability of less than one year. From top to bottom views include polar (north), global, and polar (south). Correlations can range from -1 to 1.

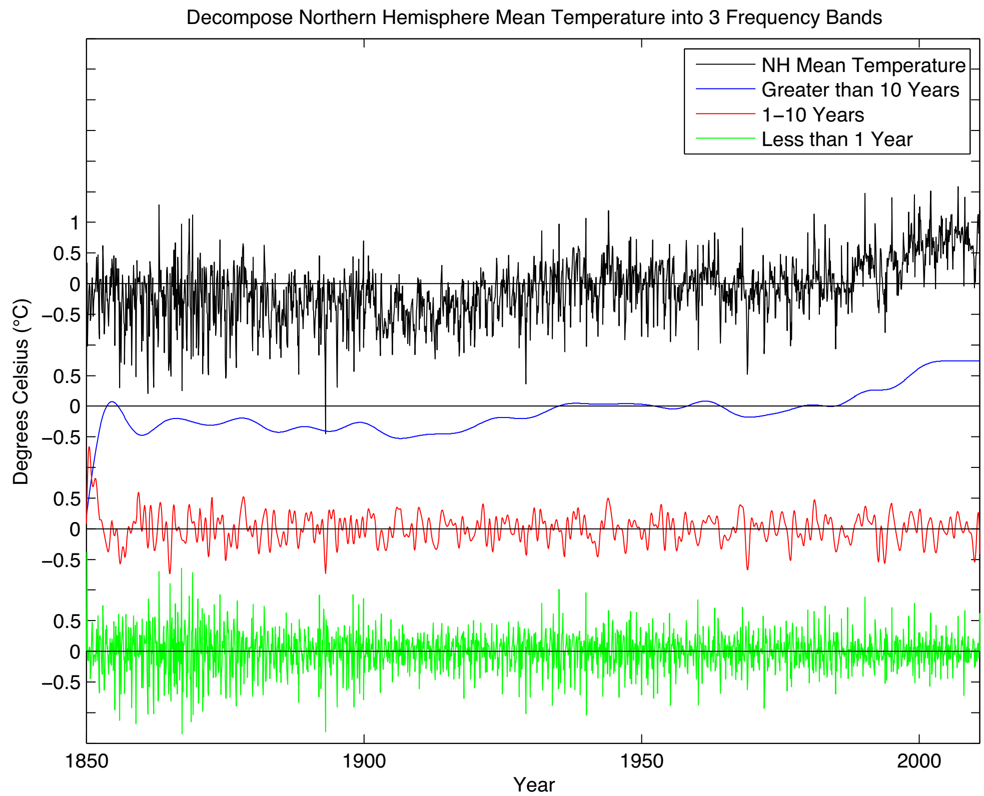

Figure 3.6 As in Figure 3.1, but for northern hemisphere (30°-90°N) mean temperature.

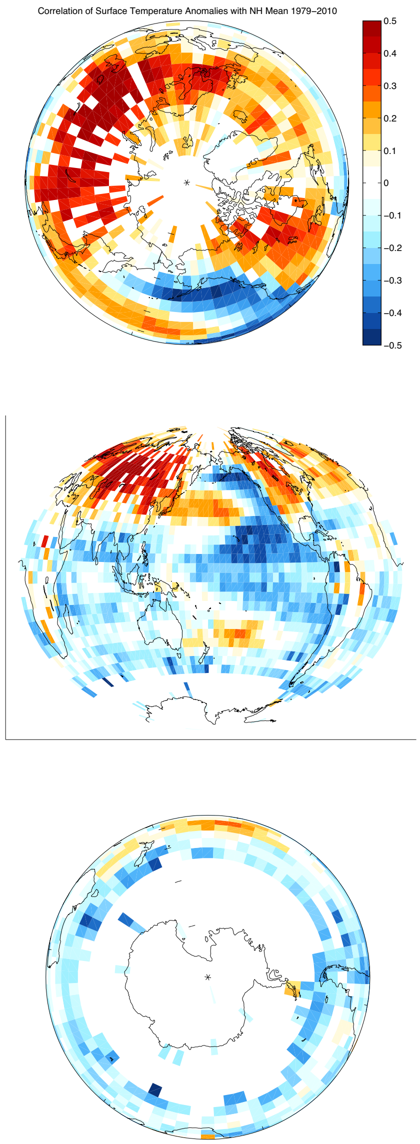

Figure 3.7 As in Figure 3.2, but for correlation of surface temperature anomalies with northern hemisphere (30°-90°N) mean temperature.

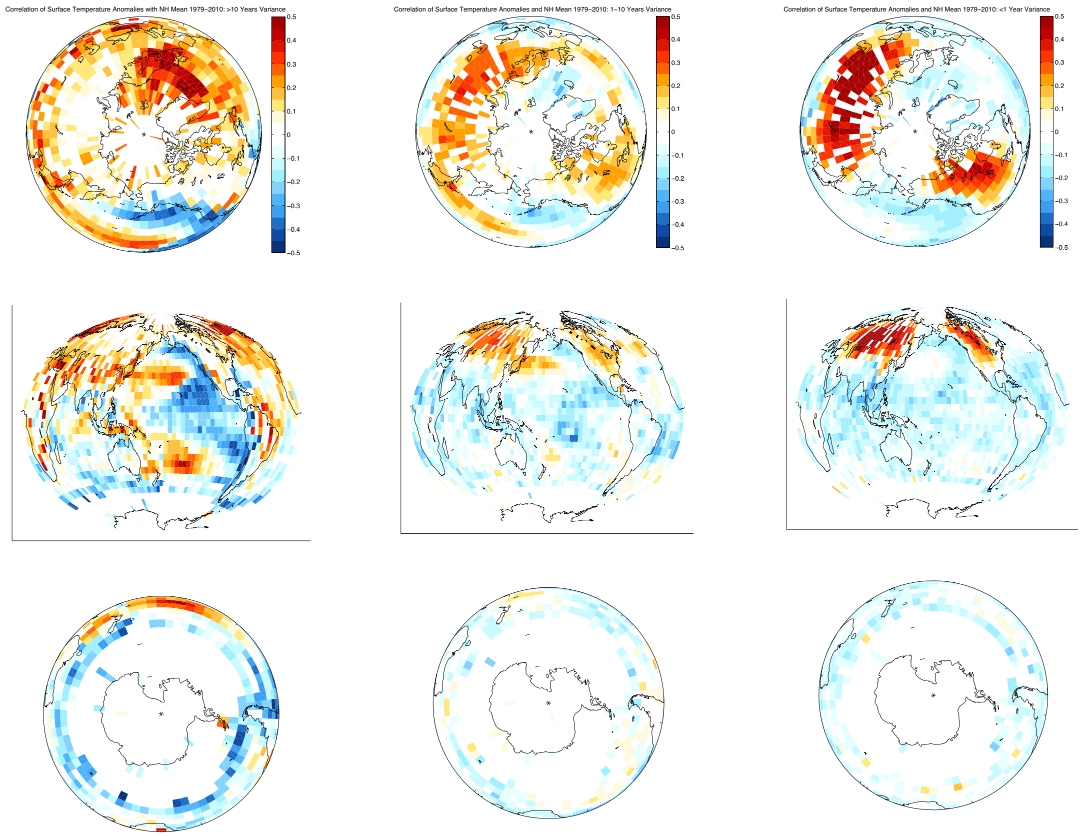

Figure 3.8 As in Figure 3.3, but for correlation of surface temperature anomalies with filtered northern hemisphere (30°-90°N) mean temperature.

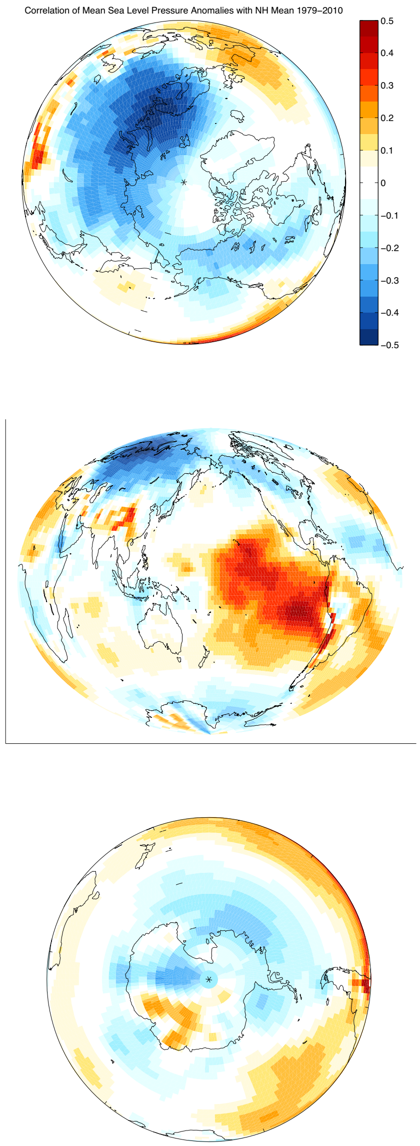

Figure 3.9 As in Figure 3.4, but for correlation of sea level pressure anomalies with northern hemisphere (30°-90°N) mean temperature.

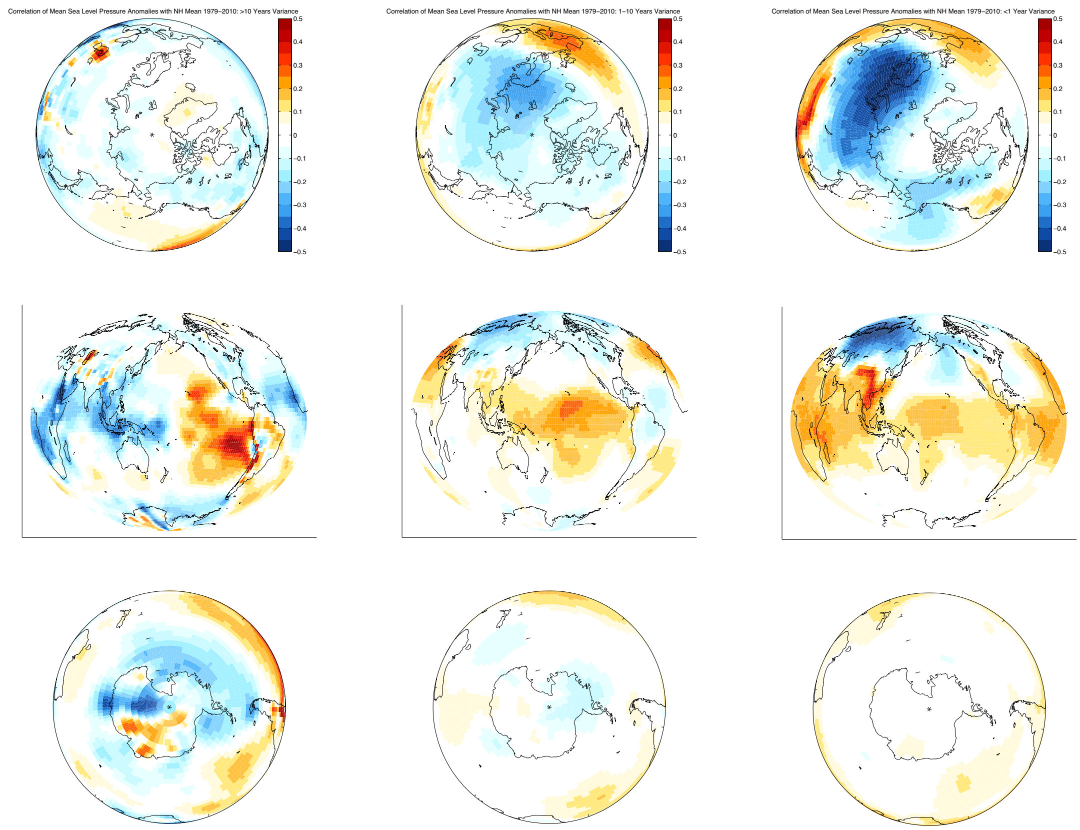

Figure 3.10 As in Figure 3.5, but for correlation of sea level pressure anomalies with filtered northern hemisphere (30°-90°N) mean temperature.

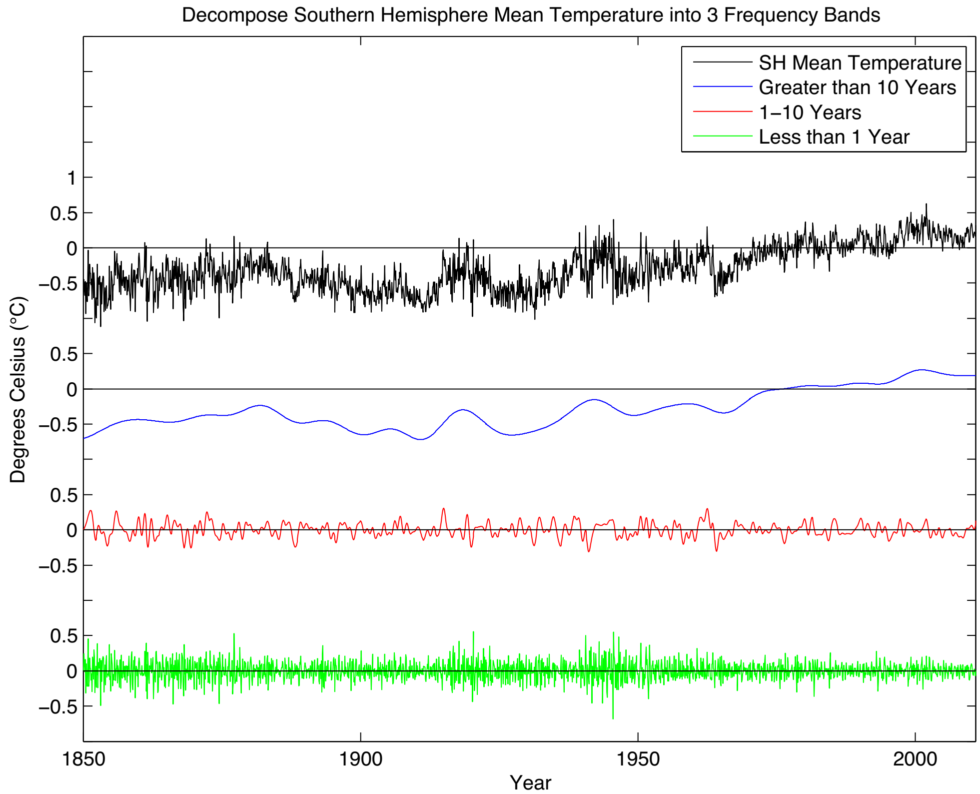

Figure 3.11 As in Figure 3.1, but for southern hemisphere (30°-90°S) mean temperature.

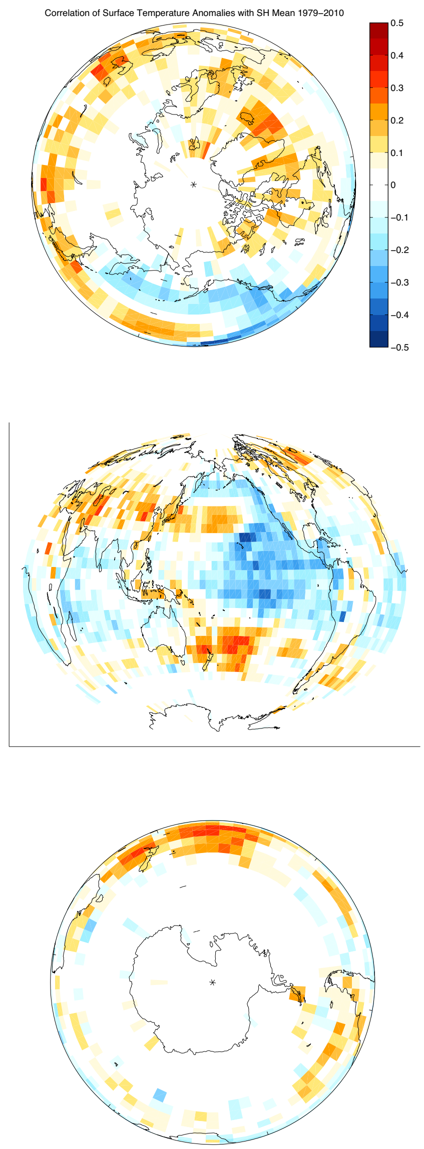

Figure 3.12 As in Figure 3.2, but for correlation of surface temperature anomalies with southern hemisphere (30°-90°S) mean temperature.

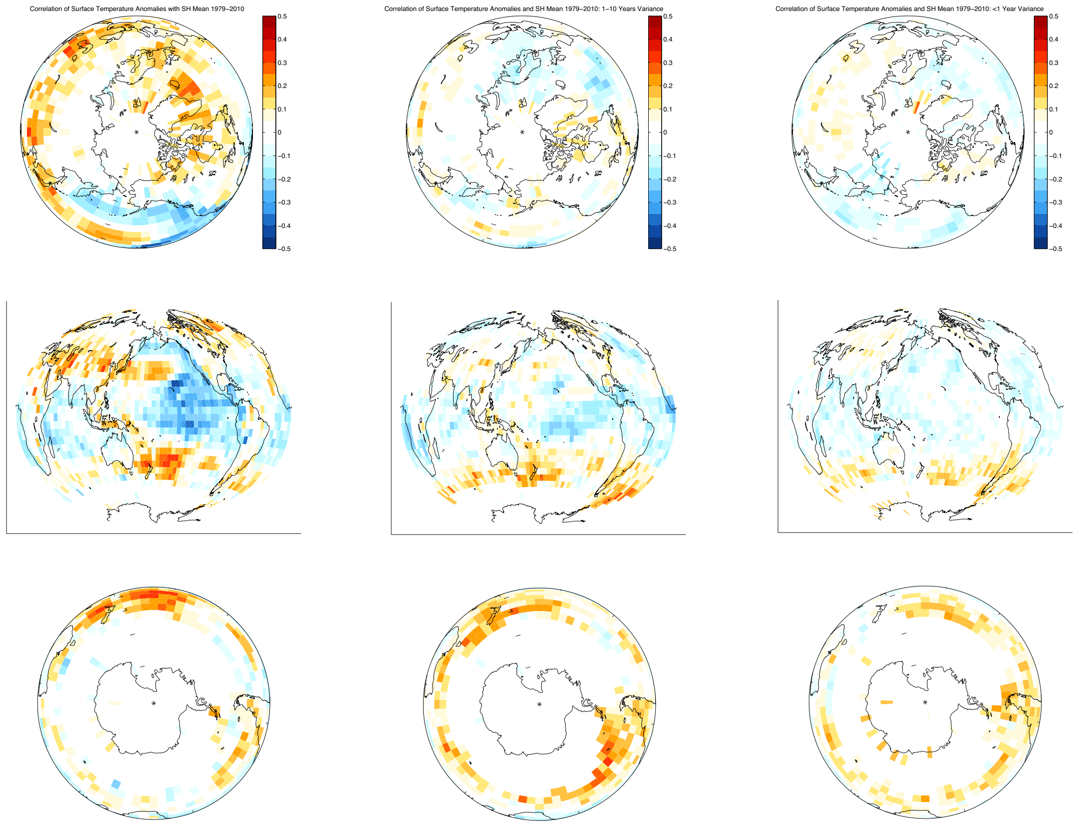

Figure 3.13 As in Figure 3.3, but for correlation of surface temperature anomalies with filtered southern hemisphere (30°-90°S) mean temperature.

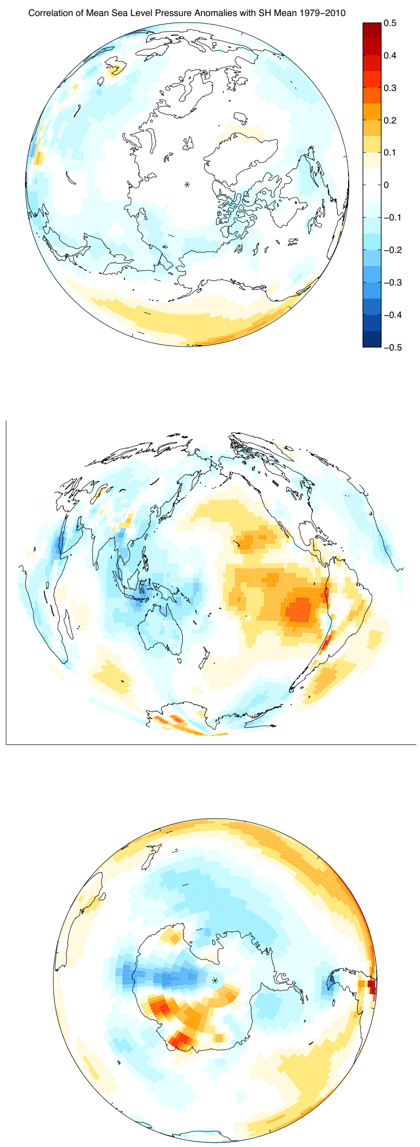

Figure 3.14 As in Figure 3.4, but for correlation of sea level pressure anomalies with southern hemisphere (30°-90°S) mean temperature.

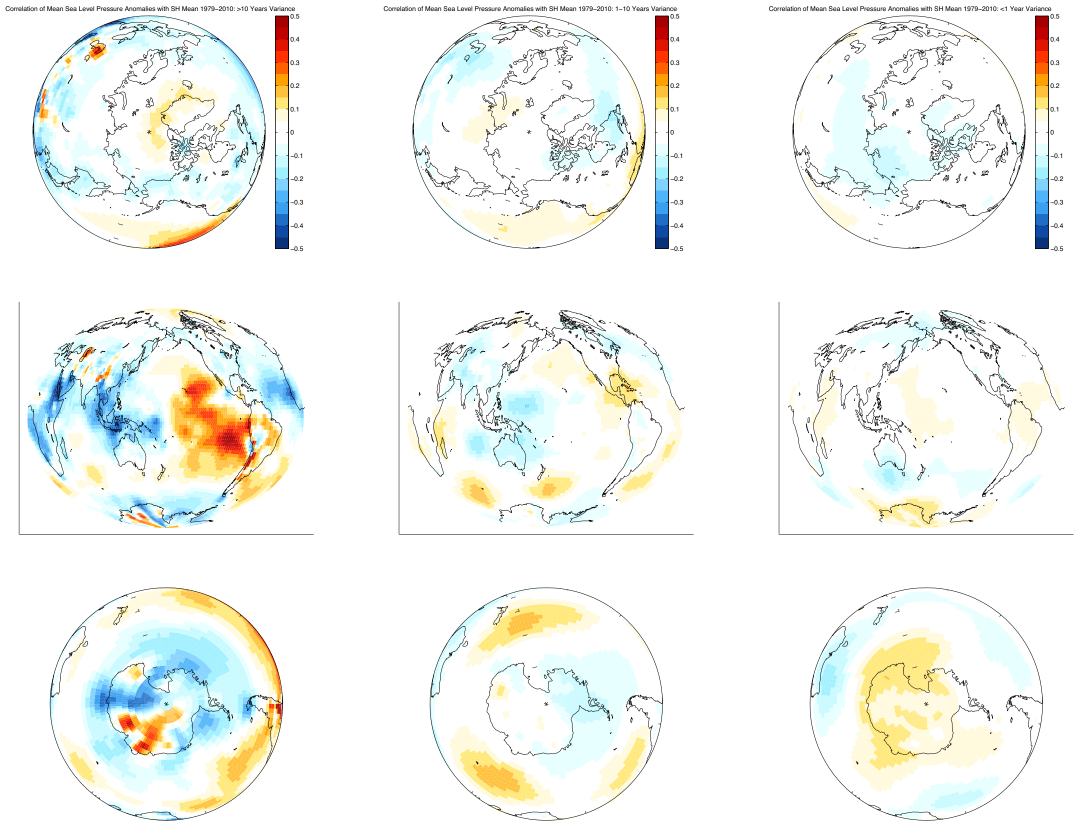

Figure 3.15 As in Figure 3.5, but for correlation of sea level pressure anomalies with filtered southern hemisphere (30°-90°S) mean temperature.

Table 3.1 Correlations of Surface Temperature and Filtered Surface Temperature Time Series			
TIME SERIES	GLOBAL (Figure 3.1)	NH (Figure 3.6)	SH (Figure 3.11)
1 - Unfiltered	1	1	1
2 - Greater than 10 Years	0.8670	0.5916	0.8462
3 - 1-10 Years	0.3425	0.4099	0.3147
4 - Less than One Year	0.3442	0.6562	0.4329

Table 3.2 Variance Explained: Surface Temperature & Filtered Surface Temperature Time Series			
TIME SERIES	GLOBAL (Figure 3.1)	NH (Figure 3.6)	SH (Figure 3.11)
1 - Unfiltered	100%	100%	100%
2 - Greater than 10 Years	75.17%	35.00%	71.61%
3 - 1-10 Years	11.73%	16.80%	9.90%
4 - Less than One Year	11.85%	43.06%	18.74%
Total (2+3+4)	98.75%	94.86%	100.25%

Table 3.3 Standard Deviations of Surface Temperature Time Series			
TIME SERIES	GLOBAL (Figure 3.1)	NH (Figure 3.6)	SH (Figure 3.11)
1 - Unfiltered	0.2888	0.4942	0.3123
2 - Greater than 10 Years	0.2543	0.3337	0.2667
3 - 1-10 Years	0.1047	0.2329	0.0969
4 - Less than One Year	0.0947	0.3071	0.1299

Table 3.4 Correlations between Global and Hemispheric Surface Temperature Time Series			
TIME SERIES	GLOBAL (Figure 3.1)	NH (Figure 3.6)	SH (Figure 3.11)
1 - Unfiltered	1	0.8068	0.7170
2 - Greater than 10 Years	1	0.9441	0.8915
3 - 1-10 Years	1	0.6192	0.2182
4 - Less than One Year	1	0.8576	0.3269

Table 3.5 Variance Explained: Global and Hemispheric Surface Temperature Time Series				
TIME SERIES	GLOBAL (Figure 3.1)	NH (Figure 3.6)	SH (Figure 3.11)	TOTAL (NH+SH)
1 - Unfiltered	100%	65.09%	51.41%	116.50%
2 - Greater than 10 Years	100%	89.13%	79.48%	168.61%
3 - 1-10 Years	100%	38.34%	4.76%	43.10%
4 - Less than One Year	100%	73.55%	10.69%	84.23%

Table 3.6 Correlations between NH and SH Surface Temperature Time Series	
TIME SERIES	NH Correlated with SH
1 - Unfiltered	0.4385
2 - Greater than 10 Years	0.7942
3 - 1-10 Years	0.1133
4 - Less than One Year	0.0460

Table 3.7 Variance Explained: NH and SH Surface Temperature Time Series	
TIME SERIES	NH Correlated with SH
1 - Unfiltered	19.23%
2 - Greater than 10 Years	63.08%
3 - 1-10 Years	1.28%
4 - Less than One Year	0.21%

CHAPTER FOUR

Surface Temperature and Sea Ice Concentration

The previous chapter examined the different temporal scales of variance in global mean temperature. This chapter will first look more closely at the relationship between hemispheric mean surface temperature and sea ice concentration through lag correlations. Past studies have analyzed global mean temperature by removing the variance associated with specific physical influences, such as ENSO, dynamical variability, and volcanoes. In the second half of this chapter hemispheric time series of sea ice concentration are used to remove the variance associated with sea ice concentration from the hemispheric mean temperature time series, and vice versa. In these ways we aim to better understand the relationship between mean surface temperature and sea ice concentration in both the Northern Hemisphere (NH) and Southern Hemisphere (SH).

4.1 Forming Hemispheric Mean Sea Ice Concentration Time Series

To remove the variance associated with sea ice concentration from mean surface temperature, or vice versa, a time series for sea ice concentration must be formed. This was done for each hemisphere (30°-90° latitude) by cosine-weighting the monthly mean HadISST sea ice concentration anomalies by latitude and finding the hemispheric mean for each month. The time series were formed for 1979-2010 to ensure that the more reliable satellite data was utilized.

The resultant NH and SH sea ice concentration time series are shown in Figure 4.1 (bottom) and Figure 4.5 (bottom), respectively. The trend in the NH time series is negative, at -0.47% ice concentration anomaly/decade, meaning that NH sea ice cover is declining with time. This value is larger in magnitude than that found for the global decrease in sea ice concentration (-0.01% ice concentration anomaly/decade), by over thirty times, and is in line with current estimates. Parkinson and Cavalieri (2008) estimated the trend in Arctic sea ice concentration to be -3.7±0.4% anomaly/decade for the period 1979-2006, which does not include large decreases in sea ice concentration over the past few years. The trend in the SH is positive, at 0.24% ice concentration anomaly/decade, meaning that SH sea ice cover is increasing with time. This trend is also consistent with recent estimates. Cavalieri and Parkinson (2008) explain that the total Antarctic sea ice cover has been gradually increasing since the mid-1970s and estimate the trend to be 0.96±0.61% anomaly/decade. Both hemispheric sea ice concentration trends are significant to the 99.99% level.

The hemispheric mean temperature time series are the same time series used in Chapter 3, just reduced to the years 1979-2010. The trends in the NH and SH mean temperature time series are positive, at 0.29°C/decade and 0.06°C/decade, respectively. The hemispheric temperature trends are both significant to the 99.99% level. It is interesting to note that during the time period of analysis hemispheric mean temperature is increasing in both hemispheres while sea ice concentration is decreasing in the NH, but increasing in the SH. Decadal trends and standard deviations for the sea ice concentration time series can be found in Table 4.1 and 4.2 at the end of the chapter.

4.2 Hemispheric Lag Correlations

The goal of this section is to take a closer look at the relationship between mean surface temperature and sea ice concentration by calculating lag correlations on a hemispheric basis.

4.2.1 Northern Hemisphere

Lag correlations were calculated between the NH sea ice concentration time series and NH mean surface temperature time series for 1979-2010. Overall, the best lag was found when the NH mean surface temperature led sea ice concentration by 3 months, as can be seen in Figure 4.2.

In Figure 4.3 we examine these lags as a function of calendar month. The sea ice concentration time series was used as a base and NH mean surface temperatures were lagged ±6 months around the sea ice concentration. Only the cold months were used for the NH sea ice concentration base (October through March). Correlations at negative lag denote surface temperature leading sea ice, and vice versa. Near zero correlations extend along a diagonal from the upper left hand to lower right hand sides of the figure. The correlations below this line are large and negative. A secondary area of large negative correlations is also found in the upper part of the figure for surface temperatures in the months of boreal spring and early summer, April through June.

To understand Figure 4.3 consider the results using November and February as a base month for sea ice concentration. The large negative correlations during November extend from lags -6 to 0, and thus, signify that surface temperatures during the previous summer and contemporaneous fall months are highly correlated with the amount of sea ice that forms during any given November. In contrast, the negative correlations for February are limited to lags -3 to -6, and thus, signify that February sea ice concentration is linked to temperatures during the previous fall, but not winter temperatures. The negative correlations at positive lags suggest that winter ice concentration is linked to NH mean spring temperatures.

The bimodal pattern in correlations between negative and positive lags in Figure 4.3 indicates a potential sea ice concentration feedback: for example, temperature forces ice and ice forces temperature. We expect that the surface temperature in months preceding October might affect sea ice concentration: colder summers should lead to colder ocean temperature and thus earlier ice formation.

It is less expected that the months following October should be highly negatively correlated with sea ice concentration. One possible mechanism for ice forcing temperatures is via its role in insulating the atmosphere from the underlying ocean. This feedback is based on the principle that sea ice cover decreases air-sea heat exchange by limiting oceanic sensible and latent heat losses to the atmosphere (National Research Council, 2003). Once sea ice has receded from an area it is difficult for it to return due to increased heat exchange and warmer surface temperatures. Another potential feedback is the ice albedo feedback. The albedo of ice is much higher than that of the ocean. As sea ice concentration decreases areas of open water and lower albedo increase. These ocean areas absorb more solar radiation and contribute heat to the climate system. The ice albedo feedback in a warming climate induces a positive perturbation to the surface energy budget (National Research Council, 2003).

In the analysis thus far we have focused on the NH, defined as 30°-90°N latitude. Figure 4.4 shows the same type of correlation results as Figure 4.3, but limited to the following areas: 30°-90°N, 40°-90°N, 50°-90°N, and 60°-90°N. (Note that limiting the area of the analysis affects the temperature time series but not the ice time series, since sea ice is limited to polar regions). Overall, the same general pattern remains across all latitude-restricted areas. Thus, the apparent lead/lag relationship between hemispheric mean temperature and sea ice are 1) robust to changes in the analysis domain; and 2) as expected – derive primarily from the polar regions.

4.2.2 Southern Hemisphere

Analogous lag correlations were calculated between the SH sea ice concentration time series and SH mean surface temperature time series for 1979-2010 and are shown in Figure 4.6. As in Figure 4.3 the sea ice concentration time series was used as a base and SH mean surface temperatures were lagged ±6 months around the sea ice concentration. Again, only the cold months have been used for the SH sea ice concentration base (April through September). The results in Figure 4.6 are very different from those for the NH. In general, there is no evidence that SH warm season temperatures lead SH winter sea ice concentration. Nor is there any evidence that SH winter sea ice concentration leads SH spring temperature.

Figure 4.7 extends the results in Figure 4.6 to smaller polar areas to minimize midlatitude influences. The areas used were: 30°-90°S, 40°-90°S, 50°-90°S, and 60°-90°S. (Note that including data equatorward of 60° latitude can only hurt the amplitude of the correlation results, since temperature and sea ice concentration linkages are largely limited to high latitude temperatures). In general the results are more similar to those for the NH when the temperature time series is limited to high latitudes. Thus, cold summer temperatures lead to positive sea ice anomalies. There is no evidence of winter sea ice anomalies forcing spring temperatures.

4.3 Removing Sea Ice Concentration Variance and Mean Temperature Variance by Hemisphere

Similar to the analysis done for global mean temperatures in Chapter 3, we wish to remove the variance associated with sea ice concentration from the hemispheric mean temperature time series, and vice versa. Seeing the results of the lag correlations above we examined the relationship between: 1) winter sea ice concentration and preceding fall temperatures, and 2) winter sea ice concentration and following spring temperatures. This was done using four-month seasonal segments. Each segment begins during the month when the seasonal equinox or solstice occurs and continues through the next three months. For example, winter in the NH was defined as December/January/February/March, while winter in the SH was defined as June/July/August/September. Fall in the NH was defined as September/October/November/December and spring was defined as March/April/May/June. Using this mode of selection, fall and spring each have one overlapping month with winter data. Similar month selection for the SH left fall as March/April/May/June and spring as September/October/November/December.

4.3.1 Northern Hemisphere

To begin we looked at NH winter sea ice concentration and NH mean fall temperature. These two time series can be seen in Figure 4.8. Since our lag correlation results from above lead us to believe that fall temperatures force winter sea ice concentration we will remove the variance associated with mean surface temperature in the fall from winter sea ice concentration. When these two time series are clipped to four-month segments as described above it is found that NH fall temperatures lead winter sea ice concentration by 2 months.

The NH mean surface temperature time series was fitted to NH winter sea ice concentration and a residual was calculated. These three time series can be seen in Figure 4.9. The residual shows the NH winter sea ice concentration with the influence of NH mean fall surface temperature variance removed. The correlation between the sea ice concentration time series (top) and the fitted (middle) time series is 0.54, which means that NH mean fall surface temperatures explain 29% of the variance in NH winter sea ice concentration. This is a substantial fraction of explained variance, especially compared to global numbers in which global sea ice concentration and mean surface temperature only explain 1.3% of the variance in one another. This suggests that the relationship between sea ice concentration and mean surface temperature plays a larger role in the NH than the rest of the globe. The correlation between the sea ice concentration time series (top) and the residual (bottom) is 0.84, which means that factors other than NH mean fall surface temperatures account for 71% of the variance in NH winter sea ice concentration. These results can be seen in Table 4.7. Note that the warming of the NH during summer/fall accounts for much of the wintertime trend in sea ice concentration.

Next we looked at NH winter sea ice concentration and NH spring mean surface temperature. These two time series can be seen in Figure 4.10. Our lag correlation results from Section 4.2 lead us to believe that winter sea ice concentration forces spring temperature, hence we removed the variance associated with winter sea ice concentration from the spring mean surface temperature time series. The results can be seen in Figure 4.11. The residual shows the NH spring temperature with the influence of NH winter sea ice concentration variance removed. The correlation between the spring mean surface temperature time series and the fitted winter sea ice concentration is 0.48, which means that winter sea ice concentration explains 23% of the variance in spring temperatures.

4.3.2 Southern Hemisphere

Similar analyses were done in the SH. The fall mean surface temperature was removed from the winter sea ice concentration, and the winter sea ice concentration was removed from spring mean surface temperature. As Figure 4.6 led us to believe the lead and lag relationships in the SH are much weaker than those found in the NH. The results were not robust and will be left out of further discussion here.

4.4 Summary of Results

The goal of this chapter was to explore lag correlations between hemispheric mean temperature and hemispheric sea ice concentration variance. The primary results are:

1) In the NH, summer and fall temperatures are highly and significantly correlated with wintertime sea ice concentrations. Cold summers are followed by anomalously high sea ice concentrations, and vice versa.

2) In the NH, wintertime sea ice concentration is significantly correlated with spring areal-averaged temperatures. Winters with high sea ice concentration are followed by cool springs.

3) The warming of the NH during summer and fall appears to account (linearly) for most of the sea ice declines during NH winter.

4) The linkages between SH sea ice concentration and temperature are limited to temperatures over the polar regions and are generally much weaker than those found in the NH.

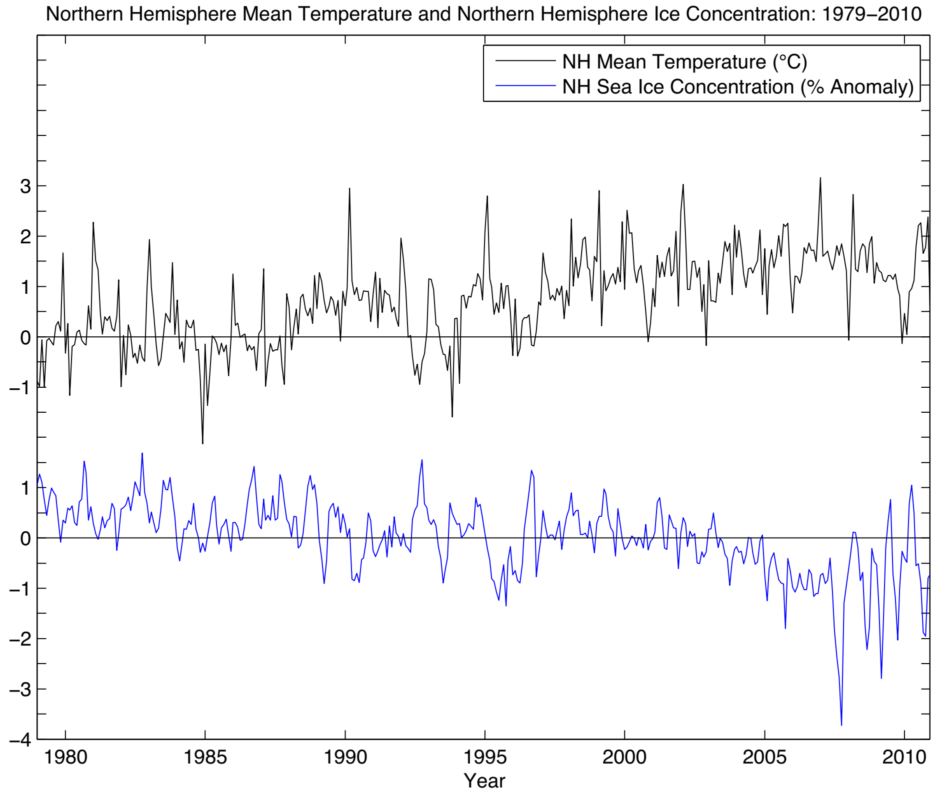

Figure 4.1 Time series of northern hemisphere mean temperature (top) and northern hemisphere sea ice concentration (bottom) from 1979-2010. Temperature is given in units of degrees Celsius, while sea ice concentration is given in units of percent anomalies in sea ice concentration (the percentage of a gridbox covered with ice). Note: the temperature time series has been multiplied by 2 to make the variability easier to visualize. Thus, a mark of 1 on the axis corresponds to 0.5°C.

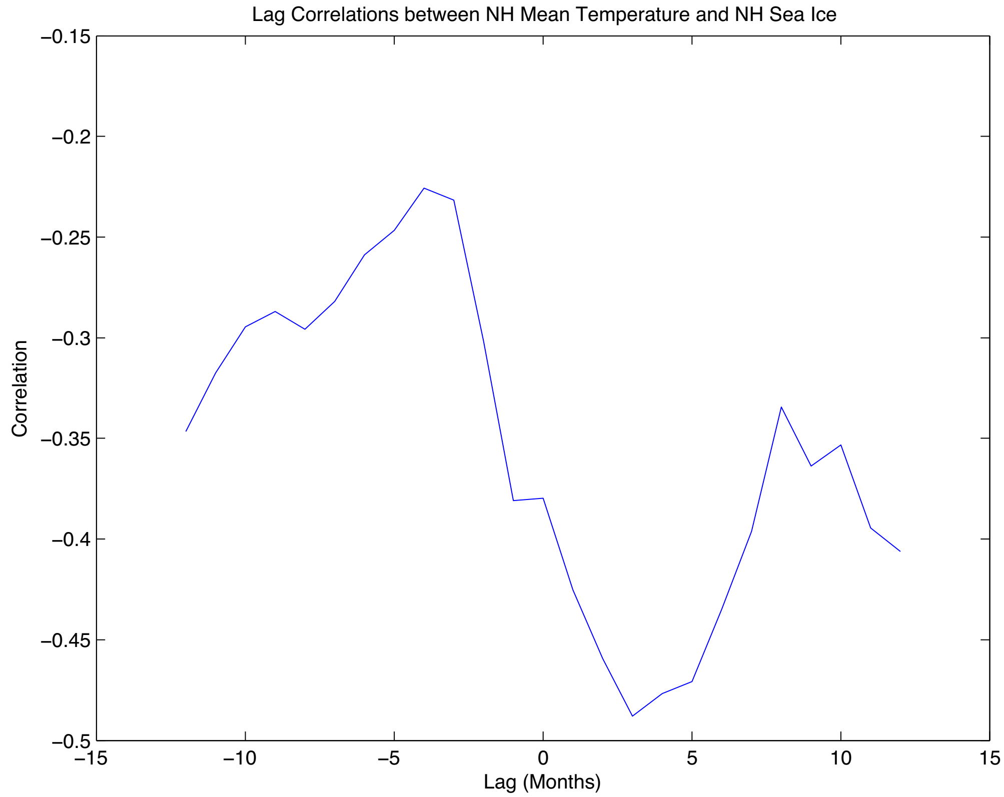

Figure 4.2 Lag correlations between northern hemisphere mean temperature and sea ice concentration from 1979-2010. The largest correlation (by absolute value) of -0.4879 exists at +3. This indicates that northern hemipshere mean temperature leads northern hemisphere sea ice concentration by 3 months.

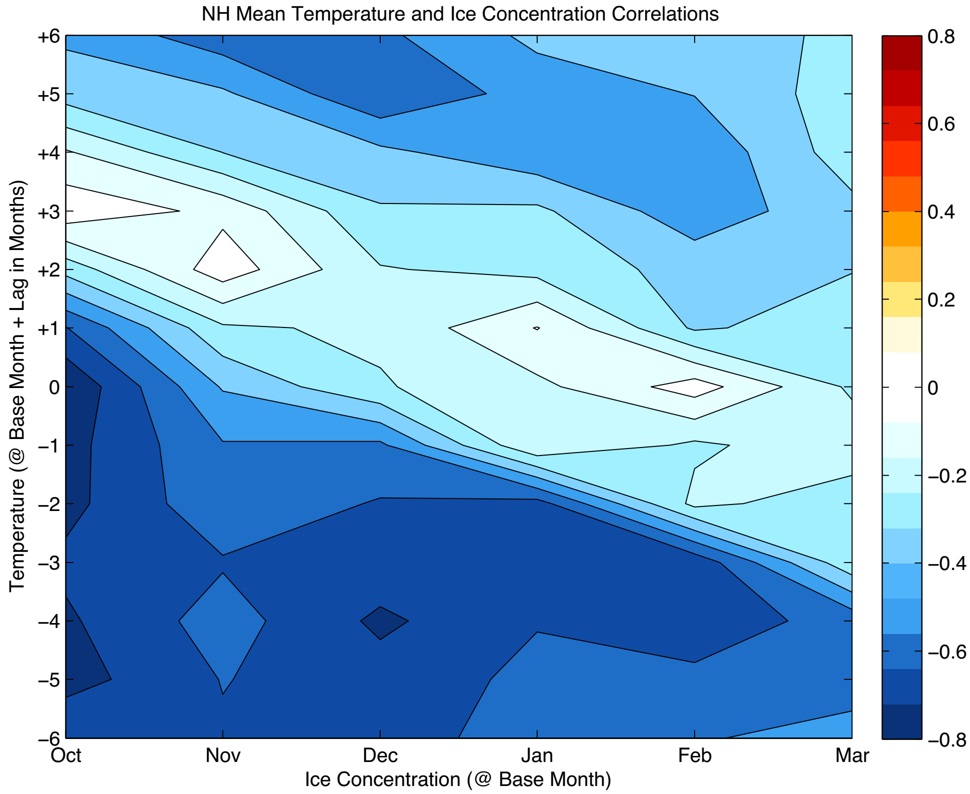

Figure 4.3 Lag correlations of northern hemisphere sea ice concentration (using cold season months as the base months) and northern hemisphere mean temperatures from 1979-2010. Correlations can range from -1 to 1.

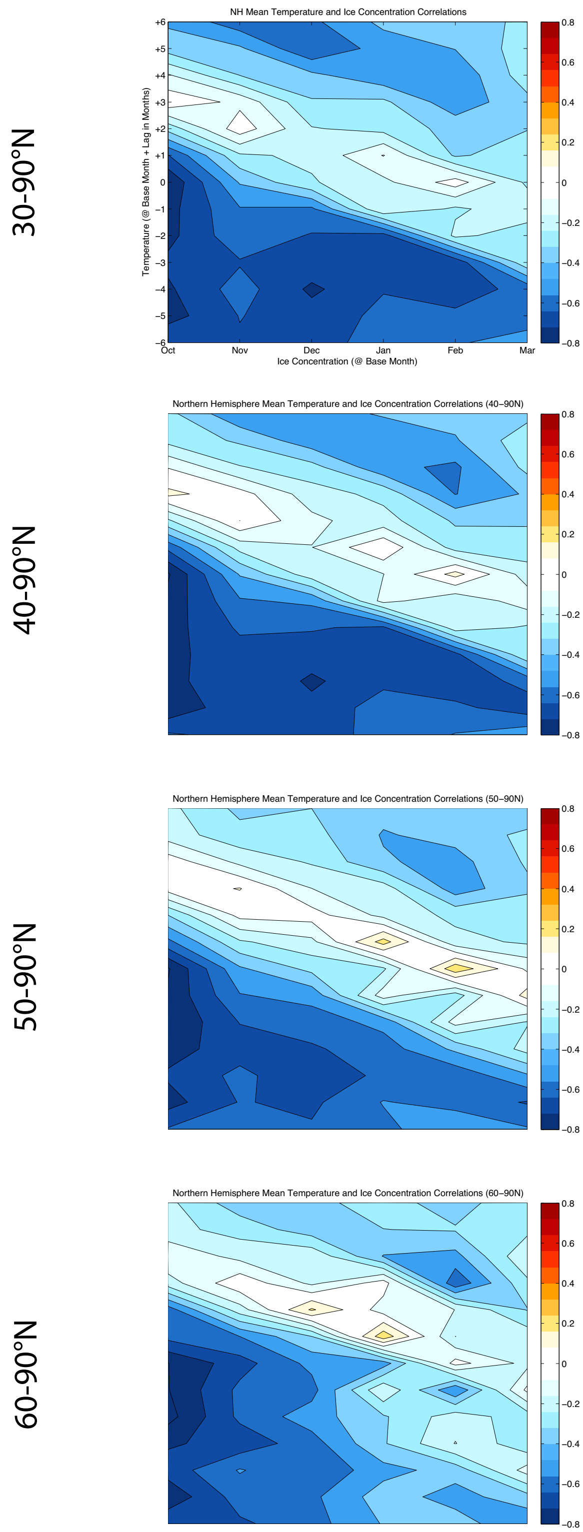

Figure 4.4 Lag correlations of northern hemisphere sea ice concentration (using cold season months as the base months) and northern hemisphere mean temperatures from 1979-2010 for various latitude restrictions. Correlations can range from -1 to 1.

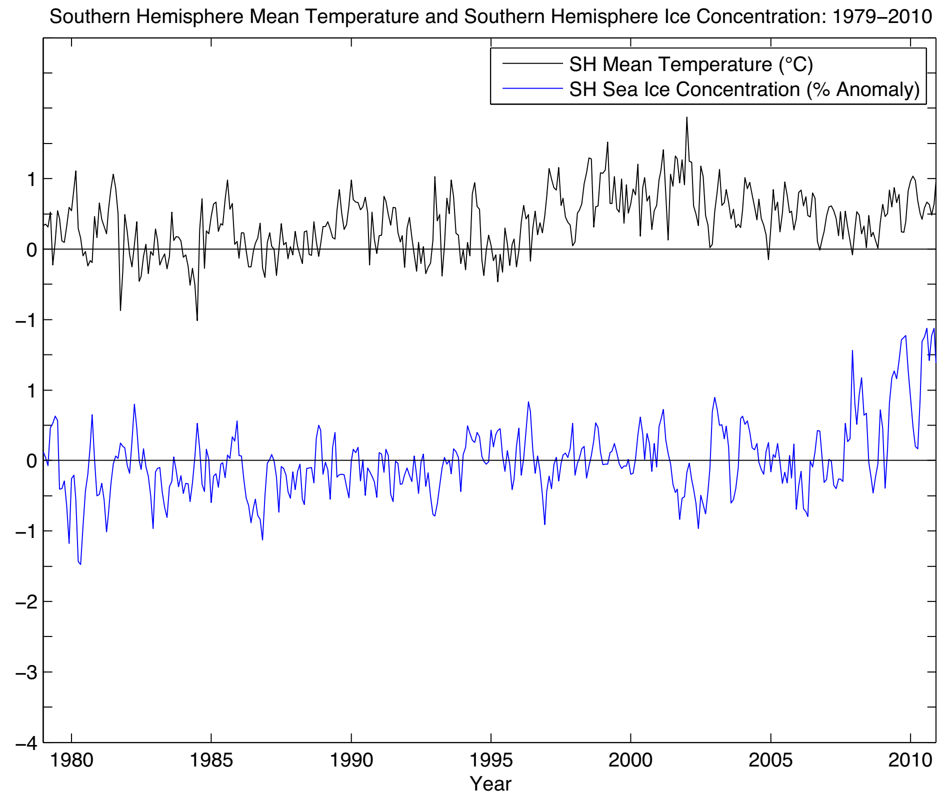

Figure 4.5 Time series of southern hemisphere mean temperature (top) and southern hemisphere sea ice concentration (bottom) from 1979-2010. Temperature is given in units of degrees Celsius, while sea ice concentration is given in units of percent anomalies in sea ice concentration (the percentage of a gridbox covered with ice). Note: the temperature time series has been multiplied by 3 to make the variability easier to visualize. Thus, a mark of 1 on the axis corresponds to 0.33°C.

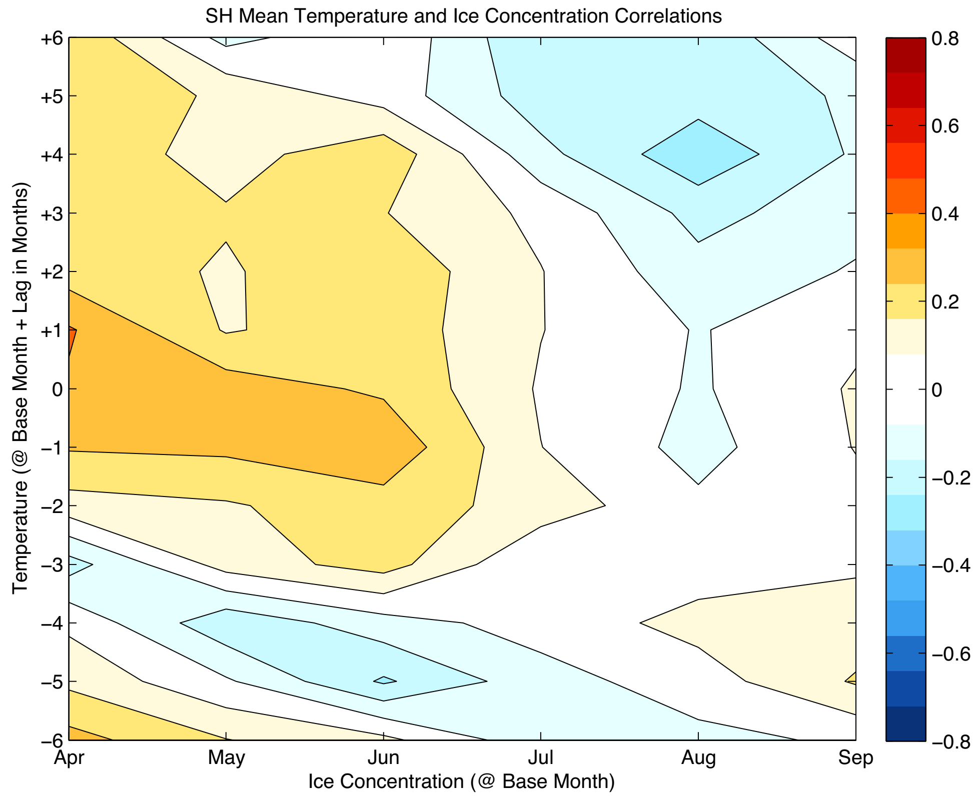

Figure 4.6 Lag correlations of southern hemisphere sea ice concentration (using cold season months as the base months) and southern hemisphere mean temperatures from 1979-2010. Correlations can range from -1 to 1.

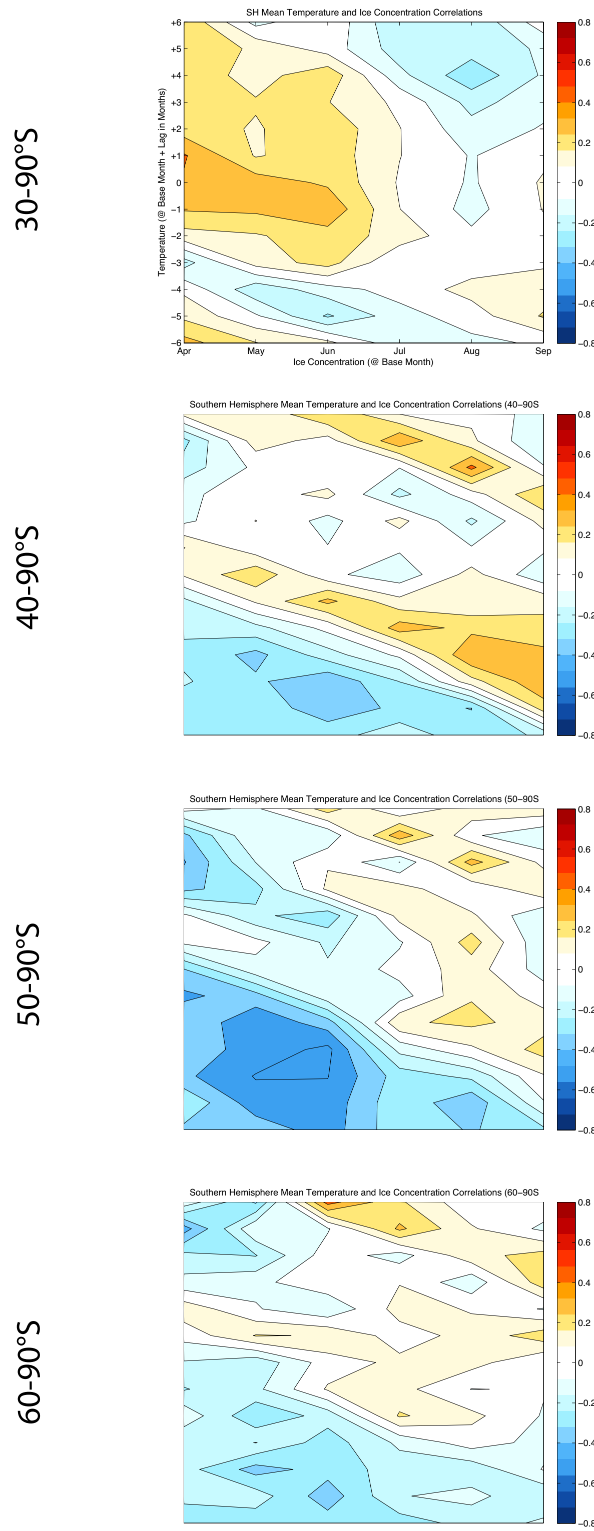

Figure 4.7 Lag correlations of southern hemisphere sea ice concentration (using cold season months as the base months) and southern hemisphere mean temperatures from 1979-2010 for various latitude restrictions. Correlations can range from -1 to 1.

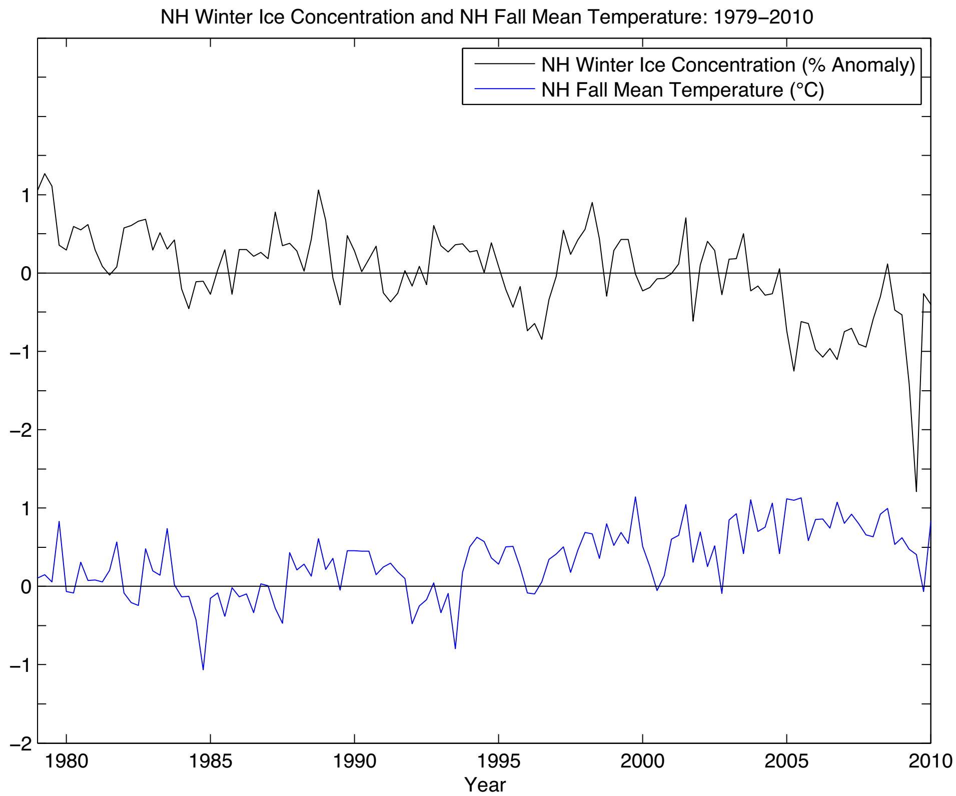

Figure 4.8 Time series of northern hemisphere winter sea ice concentration (top) and northern hemisphere fall mean temperature (bottom) from 1979-2010. Temperature is given in units of degrees Celsius, while sea ice concentration is given in units of percent anomalies in sea ice concentration (the percentage of a gridbox covered with ice).

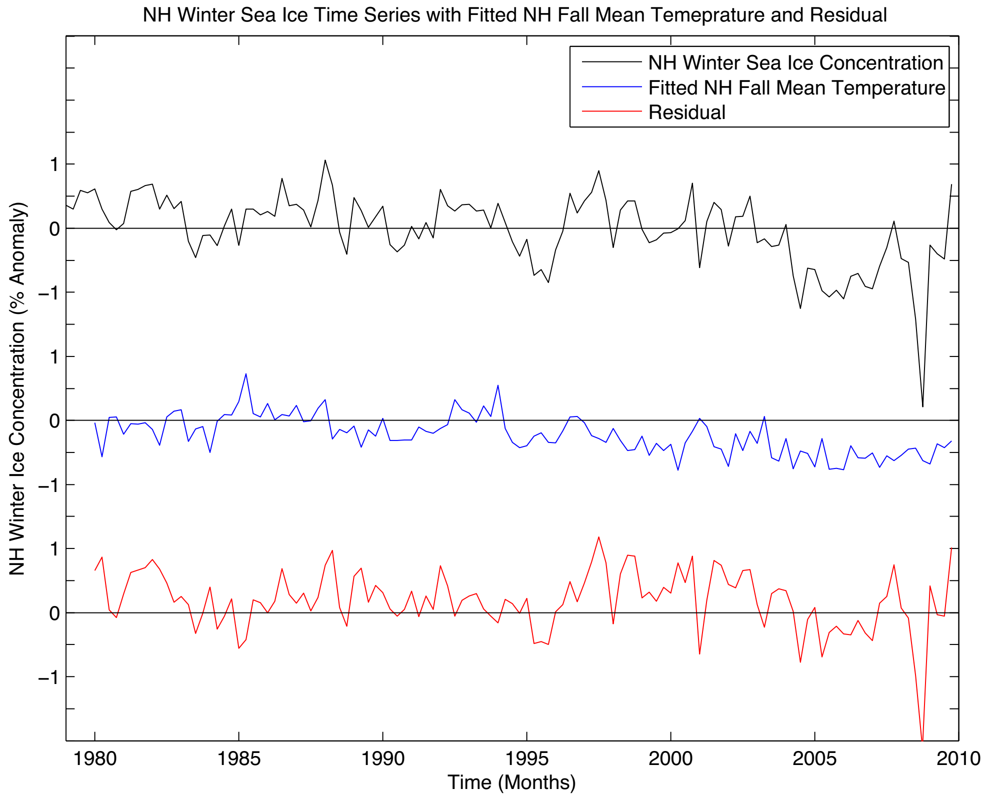

Figure 4.9 Time series of northern hemisphere winter sea ice concentration (top), fitted northern hemisphere fall mean temperature (middle), and the residual (bottom) from 1979-2010. Units are percent anomalies in sea ice concentration (the percentage of a gridbox covered with ice).

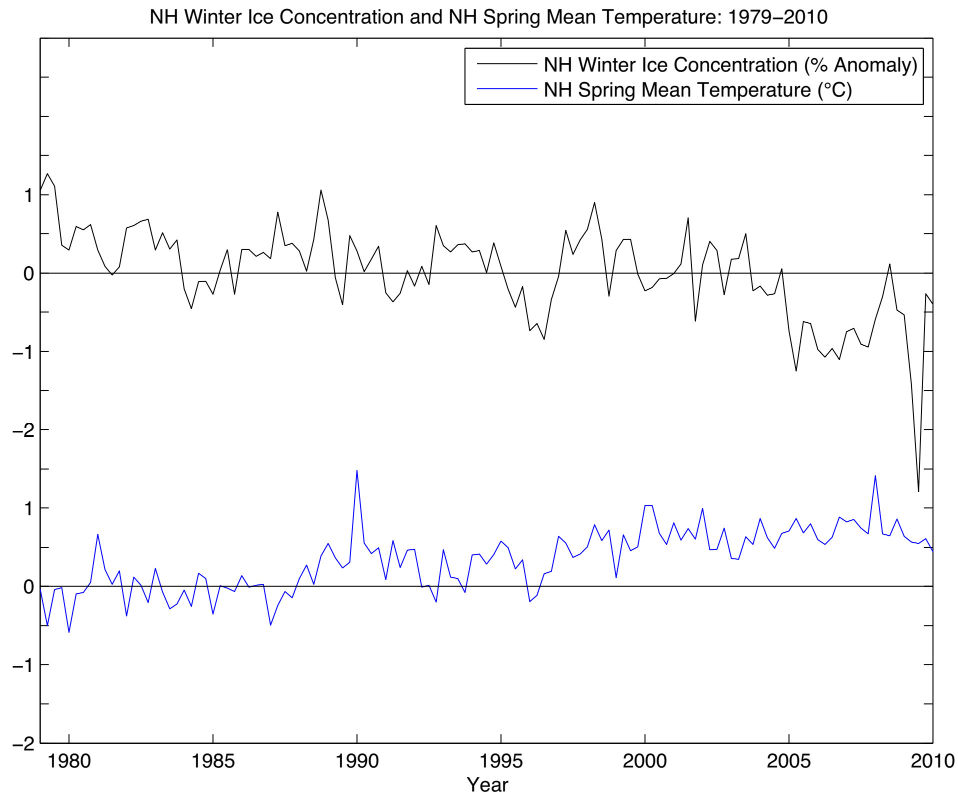

Figure 4.10 Time series of northern hemisphere winter sea ice concentration (top) and northern hemisphere spring mean temperature (bottom) from 1979-2010. Temperature is given in units of degrees Celsius, while sea ice concentration is given in units of percent anomalies in sea ice concentration (the percentage of a gridbox covered with ice).

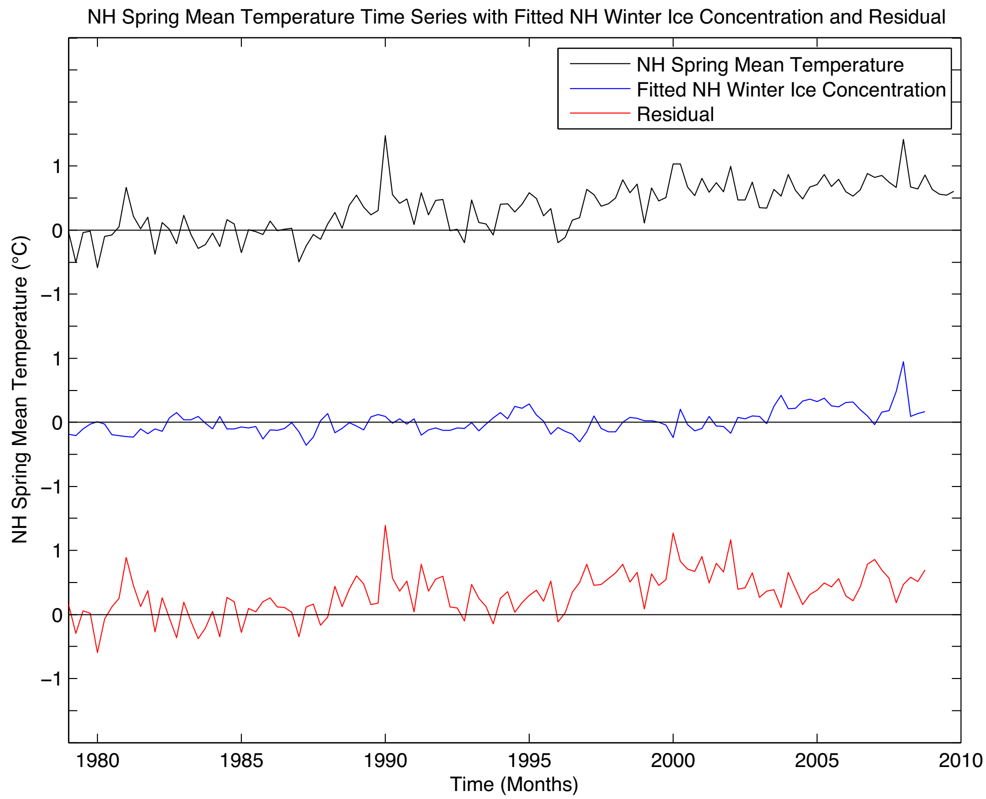

Figure 4.11 Time series of northern hemisphere spring mean temperature (top), fitted northern hemisphere winter sea ice concentration (middle), and the residual (bottom) from 1979-2010. Units are degrees Celsius.

Table 4.1 Decadal Trends in Hemispheric Mean Surface Temperature and Sea Ice Concentration Time Series		
TIME SERIES	NH (Figure 4.1)	SH (Figure 4.5)
Mean Surface Temperature (°C/decade)	0.288	0.062
Sea Ice Concentration (% Anomaly/decade)	-0.468	0.240
Note: all trends are significant at the 99.99% level.		

Table 4.2 Standard Deviation of Hemispheric Mean Surface Temperature and Sea Ice Concentration Time Series		
TIME SERIES	NH (Figure 4.1)	SH (Figure 4.5)
Surface Temperature (°C)	0.4309	0.1412
Sea Ice Concentration (% Anomaly)	0.7254	0.5186

Table 4.3 Decadal Trends in Seasonal Hemispheric Mean Surface Temperature and Sea Ice Concentration Time Series	
TIME SERIES	NH (Figure 4.8,4.10)
Fall Mean Surface Temperature (°C/decade)	0.292
Spring Mean Surface Temperature (°C/decade)	0.304
Winter Sea Ice Concentration (% Anomaly/decade)	-0.360

Table 4.4 Standard Deviation of Seasonal Hemispheric Mean Surface Temperature and Sea Ice Concentration Time Series	
TIME SERIES	NH (Figure 4.8,4.10)
Fall Mean Surface Temperature (°C/decade)	0.4339
Spring Mean Surface Temperature (°C/decade)	0.3857
Winter Sea Ice Concentration (% Anomaly/decade)	0.5726

Table 4.5 Decadal Trends and Standard Deviations for the NH Winter Sea Ice Concentration Time Series, Fitted Surface Temperature, and Residual (Figure 4.9)		
TIME SERIES	Decadal Trend (% Anomaly/decade)	Standard Deviation
Winter Sea Ice Concentration	-0.328	0.5493
Fitted NH Fall Mean Surface Temperature	-0.216	0.2962
Residual	-0.112	0.4662

Table 4.6 Decadal Trends and Standard Deviations for the NH Spring Mean Surface Temperature Time Series, Fitted Sea Ice Concentration, and Residual (Figure 4.11)		
TIME SERIES	Decadal Trend (°C/decade)	Standard Deviation
Spring Mean Surface Temperature	0.320	0.3881
Fitted NH Winter Ice Concentration	0.120	0.1863
Residual	0.220	0.3456

Table 4.7 Correlations and Variance Explained for Seasonal Sea Ice Concentration and Seasonal Mean Surface Temperature Time Series		
TIME SERIES	Correlation	Variance Explained
Northern Hemisphere		
Winter Sea Ice Concentration and Fitted Fall Mean Surface Temperature	0.5375	28.89%
Winter Sea Ice Concentration and Residual	0.8433	71.12%
Spring Mean Surface Temperature and Fitted Winter Sea Ice Concentration	0.4753	22.59%
Spring Mean Surface Temperature and Residual	0.8873	78.73%

CHAPTER FIVE

Conclusions

In this chapter we will summarize and discuss the key results of the thesis and offer suggestions for future work.

Research on global mean temperature can be approached in many different ways. Some researchers create models to predict future temperature trends, while some analyze radiation at the top of the atmosphere, and others focus on surface energy budgets. This thesis focuses on factors that influence the surface energy budget, since the surface most strongly controls changes in global mean surface temperature.

Over the past century the global mean temperature has increased in response to anthropogenic forcing. The extent of anthropogenic warming is difficult to accurately quantify as the global mean temperature time series is superposed on much natural variability on intraannual, interannual, and decadal timescales. Past studies have focused on removing known natural sources of variance from the global mean temperature. The purpose of this study is to extend previous research by exploring signatures of dynamical variability on multiple timescales and signatures of sea ice in global mean temperature.

In this thesis we first examined global mean temperature variability by filtering the global mean temperature time series using the Butterworth Filter. The three time series that were created contained variability on intraannual (< 1 year), interannual (1-10 years), and decadal (>10 years) scales and were correlated with surface temperature and sea level pressure to assess dynamical variability. The analysis then transitioned to sea ice. Hemispheric sea ice concentration time series were created and the relationship between sea ice and hemispheric mean surface temperature was assessed. The central findings of these analyses are discussed below:

1) Variability in global mean temperature is linked to various climate processes that occur on many different timescales. In Chapter 3 we were able to identify signatures of the PDO and possibly the AMO on decadal scales, ENSO on interannual scales, and the COWL pattern on intraannual scales. These timescales are typical of each of these patterns. The PDO is known to occur on 20-30 year cycles, ENSO occurs every 3-8 years, and the COWL pattern occurs on shorter timescales related to advection (Wallace et al., 1995; Mantua et al., 1997; Trenberth et al., 2002).

2) Analyzing different timescales of global mean temperature variability is extremely useful and necessary. This became apparent when we found that signatures of climatic patterns can be hidden in the full global mean temperature time series, as evidenced in Figure 3.2. The correlations in Figure 3.2, which are calculated for the full global mean temperature time series (all frequencies included), do not show an ENSO signal. However, when the global mean

temperature is filtered before calculating the correlations, as in Figure 3.3, the ENSO signal is obvious and visible in the middle column, on the interannual scale. The structure of the PDO also becomes readily visible in the filtered global mean temperature correlations in the left column, on the decadal timescale. The signatures of ENSO and the PDO are largely opposite and when the full global mean temperature is used in the correlations, as in Figure 3.2, they cancel one another out. This implies that the PDO and ENSO have opposing effects on global mean surface temperature. Additionally, areas of contrasting correlations between land and ocean, a sign of the COWL pattern, become overwhelmingly apparent in correlations with the highest frequency global mean temperature time series and cannot be seen in the correlations with full global mean temperature.

3) The North Atlantic Ocean appears to play a role in long-term global temperature variability. This region was repeatedly highlighted by strong positive correlations between mean surface temperature and surface temperature anomalies in global and NH analyses. The North Atlantic is an important area for the thermohaline circulation, which is associated with large latent and sensible heat fluxes and North Atlantic Deep Water formation. These processes are likely linked to the warming in this region on decadal scales.

4) The NH continents possess the ability to greatly influence global surface temperature on intraannual timescales, more so than any other region in the world. While the global and SH mean temperature time series filtered for variability on decadal scales are most strongly correlated with the full global mean temperature time series, the intraannual time series is most highly correlated with the full global

mean temperature time series in the NH. This stems from the fact that the NH contains more land-sea contrast than the SH, which allows the COWL pattern to have a larger impact on NH surface temperatures.

5) Overall, there are no clear structures that contribute to variability in SH mean surface temperature. Correlations in Figures 3.12 and 3.13 are much smaller in amplitude than those in the NH and global figures. There is a slight signature of the PDO in Figure 3.13, but otherwise the figure is lacking signs of ENSO, the COWL pattern, or any other substantial structure. The high fraction of ocean area in the SH likely moderates temperature changes in this hemisphere.

6) Some sources of global surface temperature variability are only influential on global scales. ENSO is a prime example. In Figure 3.3, the ENSO signature is quite clear in the middle column for interannual variability. However, in NH and SH surface temperature correlations, Figures 3.8 and 3.13, there is no ENSO signature. This suggests that ENSO is a large-scale global phenomenon that has little to no impact on global mean temperature variability on hemispheric scales.

7) Variability in sea ice concentration is drastically different in the NH and SH. The difference in the trends for each of these cases can be seen in Table 4.1. Sea ice concentration is decreasing in the NH (-0.47% ice concentration anomaly/decade) and is increasing in the SH (0.24% ice concentration anomaly/decade). The global trend in sea ice concentration is -0.01% ice concentration anomaly/decade. These differences can have important implications in relation to mean surface temperature.

8) A distinct difference in the sea ice concentration - mean surface temperature relationship exists with regards to forcing. In the NH the mean surface temperature in the fall forces the winter sea ice concentration and a sea ice feedback is present. In the SH the results are not significant. These differences likely help explain why the trends in sea ice concentration are opposite in sign between the NH and SH.

While the information herein works to further our understanding of global mean temperature variability, much work remains to be done. A primary goal for the future is to continue to work towards quantifying as many natural sources of variability as possible. The influence of ENSO and volcanoes on global mean temperature variability is fairly well understood, but other sources discussed in the introduction to this thesis, such as solar variability, water vapor, precipitation, and clouds are less well understood. The more natural variability that can be removed from the global mean temperature time series, the clearer the signature of anthropogenic warming will become.

It was shown that dynamical variability on intraannual timescales is highly correlated with NH mean temperature, which has important implications for global mean temperature. Other modes of variability are very active in the NH as well. Structures of variability in the SH are less clear and contain lower amplitudes than those in the NH. This difference is due to the larger fraction of ocean area in the SH; however, it would be helpful to identify the most important mode of variability present in the SH.

The difference between the sea ice concentration trends in the NH and SH is clear and intriguing. Why does sea ice concentration increase in one hemisphere and decrease in another when global surface temperatures are increasing? Research focused on solidifying the mechanisms behind sea ice concentration processes in both the NH and SH and explanations for why differences exist between the hemispheres will be important in understanding the sea ice-climate relationship in the future.

REFERENCES

Ackerman, S. A., and J. A. Knox, 2002: *Meteorology: Understanding the atmosphere*. Pacific Grove, CA: Brooks/Cole-Thomson Learning. xxiii, 486p.

Ahrens, C.D., 2009: *Meteorology Today: An Introduction to Weather, Climate and the Environment*. Brooks/Cole, 624 p.

Andrews, T., P. M. Forster, 2008: CO_2 forcing induces semi-direct effects with consequences for climate feedback interpretations. Geophys. Res. Lett., 35, doi:10.1029/2007GL032273.

Assel, R. A., 1983: Description and analysis of a 20-year (1960–79) digital ice-concentration database for the Great Lakes of North America. Ann. Glaciol., 4, 14–18.

Baldwin, M. P., and T. J. Dunkerton, 2001: Stratospheric Harbingers of Anomalous Weather Regimes. Science, 294, 581-584, doi:10.1126/science.1063315.

Benestad, R. E., 2005: A review of the solar cycle length estimates. Geophys. Res. Lett., 32, L15174, doi:10.1029/2005GL023621.

Bjerknes, J.,1969: Atmospheric teleconnections from the equatorial Pacific. Mon. Wea. Rev., 97, 163-172.

Blanke, B., J. D. Neelin, and D. Gutzler, 1997: Estimating the Effect of Stochastic Wind Stress Forcing on ENSO Irregularity. J. Climate, 10, 1473-1486.

Briffa, K. R., T. J. Osborn, F. H. Schweingruber, I. C. Harris, P. D. Jones, S. G. Shiyatov, and E. A. Vaganov, 2001: Low-frequency temperature variations from a northern tree ring density network. J. Geophys. Res., 106, 2929– 2941.

Broccoli, A. J., N. Lau, and M. J. Nath, 1998: The Cold Ocean-Warm Land Pattern: Model Simulation and Relevance to Climate Change Detection. J. Climate, 11, 2743-2763.

Brohan, P., J. J. Kennedy, I. Harris, S.F.B. Tett, and P. D. Jones, 2006: Uncertainty estimates in regional and global observed temperature changes: a new dataset from 1850. J. Geophys. Res., 111, D12106, doi:10.1029/2005JD006548.

Cavalieri, D. J., and C. L. Parkinson, 2008: Antarctic sea ice variability and trends, 1979-2006. J. Geophys. Res., 113, doi:10.1029/2007JC004564.

Connolly, P. J., T. W. Choularton, M. W. Gallagher, K. N. Bower, M. J. Flynn, and J. A. Whiteway, 2006: Cloud-resolving simulations of intense tropical *Hector* thunderstorms: Implications for aerosol-cloud interactions. Quar. J. Royal Meteor. Soc., 132, 3079-3106.

Crowley, T. J., 2000: Causes of Climate Change Over the Past 1000 Years. Science, 289, 270-277.

Deser, C., R. Tomas, M. Alexander, and D. Lawrence, 2010: The Seasonal Atmospheric Response to Projected Arctic Sea Ice Loss in the Late Twenty-First Century. J. Climate, 23, 333-351.

Deutsches Hydrographisches Institute, 1950. Atlas of ice conditions in the North Atlantic Ocean and general charts of the ice conditions of the North and South Polar regions. Publ. 2335, Hamburg, Germany.

Diaz, H., C. Folland, T. Manabe, D. Parker, R. Reynolds, and S. Woodruff, 2002: Workshop on Advances in the Use of Historical Marine Climate Data. WMO Bulletin, 51, 377-380.

Eisenman, I., T. Schneider, D. Battisti, and C. Bitz, 2011: Consistent changes in the sea ice seasonal cycle in response to global warming. J Climate, accepted.

EPA, 2003: *National Air Quality and Emissions Trends Report, 2003 Special Studies Edition*. Publication No. EPA 454/R-03-005, U.S. Environmental Protection Agency, Washington, DC, 190pp, http://www.epa.gov.air.airtrends/aqtrnd03/.

EPA, 2011: Human-Related Sources and Sinks of Carbon Dioxide. U.S. Environmental Protection Agency, Washington, DC, http://www.epa.gov/climatechange/emissions/co2_human.html.

Erlykin, A. D., T. Sloan, and A. W. Wolfendale, 2009: Solar activity and the mean global temperature. Environ. Res. Lett., 4, 014006, doi:10.1088/1748-9326.

Folland, C. K., and D. E. Parker, 1995: Correction of instrumental biases in historical sea surface temperature data. Quar. J. Roy. Meteor. Soc., 121, 319–367.

Forster, P. M. de F., and K. P. Shine, 2002: Assessing the climate impact of trends in stratospheric water vapor. Geophys. Res. Lett., 29, 1086-1089.

Fröhlich, C., and J. Lean, 2004: Solar radiative output and its variability: evidence and mechanisms. Astron. Astrophys. Rev., 12, 273-320.

Gillett, N.P., V. K. Arora, K. Zickfeld, S. J. Marshall, and W.J. Merryfield, 2011: Ongoing climate change flowing a complete cessation of carbon dioxide emissions. Nature Geoscience, 4, 83-87.

Hansen, J. E., W. C. Wang, and A. A. Lacis, 1978: Mount Agung provides a test of a global climatic perturbation. Science, 199, 1065-1068.

Hansen, J. E., A. Lacis, R. Ruedy, and M. Sato, 1992: Potential climate impact of Mount Pinatubo eruption. Geophys. Res. Lett., 19, 215-218, doiL10.1029/91GL02788.

Hansen, J. E., M. Sato, and R. Ruedy, 1997: Radiative forcing and climate response. J. Geophys. Res.,102, 6831-6864.

Hartmann, D.L., 1994: *Global Physical Climatology*. Academic Press, 411p.

Hegerl, G. C., T. J. Crowley, S. K. Baum, K. Kim, and W. T. Hyde, 2003: Detection of volcanic, solar and greenhouse gas signals in paleo-reconstructions of Northern Hemisphere temperature. Geophys. Res. Lett., 30, doi:10.1029/2002GL016635.

Held, I. M., and B. J. Soden, 2006: Robust Responses of the Hydrological Cycle to Global Warming. J. Climate 19, 5686-5699.

Holland, M. M., and C. M. Bitz, 2003: Polar amplification of climate change in coupled models. Climate Dynamics, 21, 221-232, doi:10.1007/s00382-003-0332-6.

Hurrell, J. W., 1995: Decadal Trends in the North Atlantic Oscillation: Regional Temperatures and Precipitation. Science, 269, 676-679.

IPCC Chapter 2 & 3, 2007: *Climate Change 2007: The Physical Science Basis. Contribution of Working Group I to the Fourth Assessment Report of the Intergovernmental Panel on Climate Change*. Cambridge Univ. Press, 2007.

Jacob, D.J., 1999: *Introduction to Atmospheric Chemistry*. Princeton University Press, 266pp.

Jin, F., 1997: An Equatorial Ocean Recharge Paradigm for ENSO. Part I: Conceptual Model. J. Atmos. Sci., 54, 811-829.

Kalnay, E., M. Kanamitsu, R. Kistler, W. Collins, D. Deaven, L. Gandin, M. Iredell, S. Saha, G. White, J. Woollen, Y. Zhu, M. Chelliah, W. Ebisuzaki, W. Higgins, J. Janowiak, K. C. Mo, C. Ropelewski, J. Wang, A Leetmaa, R. Reynolds, R. Jenne, and D. Joseph, 1996: The NCEP/NCAR 40-Year Reanalysis Project. Bull. Amer. Meteor. Soc., 77, 437-471.

Kiehl, J. T., and K. E. Trenberth, 1997: Earth's Annual Global Mean Energy Budget. Bull. Amer. Meteor. Soc., 78, 197-208.

Kirby, J., J. Curtis, J. Almeida, E. Dunne, J. Duplissy, S. Ehrhart, A. Franchin, S. Gagne, L. Ickes, A. Kuerten, A. Kupc, A. Metzger, F. Riccobono, L. Rondo, S. Schobesberger, G. Tsagkogeorgas, D. Wimmer, A. Amorim, F. Bianchi, M. Breitenlechner, A. David, J. Dommen, A. Downard, M. Ehn, and R. C. Flagan, 2011: Role of sulphuric acid, ammonia and galactic cosmic rays in aerosol nucleation. Nature, 476, 429-435, doi:10.1038/nature10343.

Kistler, R., E. Kalnay, W. Collins, S. Saha, G. White, J. Woollen, M. Chelliah, W, Ebisuzaki, M. Kanamitsu, V. Kousky, H. van den Dool, R. Jenne, and M. Fiorino, 2001: The NCEP-NCAR 50-Year Reanalysis: Monthly Means CD-ROM and Documentation. Bull. Amer. Meteor. Soc., 82, 247-267.

Knight, R. W., 1984. Introduction to a new sea ice database. Ann. Glaciol., 5, 81–84.

Lean, J., J. Beer, and R. Bradley, 1995: Reconstruction of solar irradiance since 1610: Implications for climate change. Geophys. Res. Lett., 22, 3195-3198.

Lean, J. L., Y.-M. Wang, and N. R. Sheeley Jr., 2002: The effect of increasing solar activity on the Sun's total and open magnetic flux during multiple cycles: Implications for solar forcing of climate. Geophys. Res. Lett., 29, 2224, doi:10.1029/2002GL015880.

Lean, J., G. Rottman, J. Harder, and G. Kopp, 2005: SORCE Contributions to New Understanding of Global Change and Solar Variability. Solar Physics, 230, 27-53.

Lohmann, U., 2006: Aerosol Effects on Clouds and Climate. Space Science Reviews, 125, 129-137.

Manabe, S., and R. J. Stouffer, 1980: Sensitivity of a global climate model to an increase of CO_2 in the atmosphere. J. Geophys. Res., 85, 5529-5554.

Mantua, N. J., S. R. Hare, Y. Zhang, J. M. Wallace, and R. C. Francis, 1997: A Pacific Interdecadal Climate Oscillation with Impacts on Salmon Production. Bull. Amer. Meteor. Soc., 78, 1069-1079.

Marsh, N. D., and H. Svensmark, 2000: Low cloud properties influenced by cosmic rays. Phys. Rev. Lett., 85, 5004-5007.

Met Office, Hadley Centre: HadISST 1.1 - Global sea-Ice coverage and SST (1870-Present), [Internet]. NCAS British Atmospheric Data Centre, 2006. Available from http://badc.nerc.ac.uk/view/badc.nerc.ac.uk__ATOM__dataent_hadisst.

NASA, 2004: *The Role of Clouds*. National Aeronautics and Space Administration, Langley Research Center, VA, http://www.nasa.gov/audience/forstudents/58/features/F_The_Role_of_Clouds.html.

National Research Council, Panel on Climate Change Feedbacks, Climate Research Committee, 2003: *Understanding Climate Change Feedbacks*. The National Academies Press, 166p.

Parker, D. E., P. D. Jones, A. Bevan, and C. K. Folland, 1994: Interdecadal changes of surface temperature since the nineteenth century. J. Geophys. Res., 99,373-399.

Parkinson, C. L., and D. J. Cavalieri, 2008: Arctic sea ice variability and trends, 1979-2006. J. Geophys. Res. 113, doi:10.129/2007JC004558.

Rahmstorf, S., and R. Alley, 2002: Stochastic Resonance in Glacial Climate. Eos, Transactions, 83, 129.

Ramanathan, V., R. D. Cess, E. F. Harrison, P. Minnis, B. R. Barkstrom, E. Ahmad, and D. Hartmann, 1989: Cloud-Radiative Forcing and Climate: results from the Earth Radiation Budget Experiment. Science, 243, 57-63.

Rayner, N. A., D. E. Parker, E. B. Horton, C. K. Folland, L. V. Alexander, D. P. Rowell, E. C. Kent, and A. Kaplan, 2003: Global analyses of sea surface temperature, sea ice, and night marine air temperature since the late nineteenth century, J. Geophys. Res., 108, 4407, doi:10.1029/2002JD002670.

Rayner, N. A., P. Brohan, D. E. Parker, C. K. Folland, J. J. Kennedy, M. Vanicek, T. Ansell, and S. F. B. Tett, 2006: Improved analyses of changes and uncertainties in marine temperature measured in situ since the mid-nineteenth century: the HadSST2 dataset. J. Climate, 19, 446-469.

Rind, D., J. Lean, and R. Healy, 1999: Simulated time-dependent climate response to solar radiative forcing since 1600. J. Geophys. Res., 104, 1973-1990, doi:10.1029/1998JD200020.

Santer, B. D., K. E. Tayloe, T. M. L. Wigley, T. C. Johns, P. D. Jones, D. J. Karoly, J. F. B. Mitchell, A. H. Oort, J. E. Penner, V. Ramaswamy, M. D. Schwarzkopf, R. J. Stouffer, and S. Tett, 1996: A search for human influences on the thermal structure of the atmosphere. Nature, 382, 39-46.

Santer, B. D., T. M. L. Wigley, C. Doutriaux, J. S. Boyle, J. E. Hansen, P. D. Jones, G. A. Meehl, E. Roeckner, S. Spengupta, and K. E. Taylor, 2001: Accounting for the effects of volcanoes and ENSO in comparisons of modeled and observed temperature trends. J. Geophys. Res., 106, 28,033– 28,060.

Schlesinger, M. E., and N. Ramankutty, 1994: An oscillation in the global climate system of period 65-70 years. Nature, 367, 723-726, doi: 10.1038/367723a0.

Serreze, M. C., A. P. Barrett, J. C. Stroeve, D. N. Kindig, and M. M. Holland, 2009: The emergence of surface-based Arctic amplification. Cryosphere, 3, 11-19.

Solomon, S., G. K. Plattner, R. Knutti, and P. Friedlingstein, 2009: Irreversible climate change due to carbon dioxide emissions. Proc. Natl. Acad. Sci. USA, 106, 1704-1709.

Solomon, S., K. H. Rosenlof, R. W. Portmann, J. S. Daniel, S. M. Davis, T. J. Sanford, and G. Plattner, 2010: Contributions of Stratospheric Water Vapor to Decadal Changes in the Rate of Global Warming. Science, 327, 1219-1223, doi:10.1126/science.1182488.

Stommel, H., and E. Stommel, 1983: *Volcano Weather*. Seven Seas Press, 177p.

Stroeve, J., M. Serreze, S. Drobot, S. Gearhard, M. Holland, J. Maslanik, W. Meier, and T. Scambos, 2008: Arctic Sea Ice Extent Plummets in 2007. Eos, 89, 13-14.

Svensmark, H., 1998: Influence of Cosmic Rays on Earth's Climate. Phys. Rev. Lett., 81, 5027.

Thompson, D. W.J., J. M. Wallace, P. D. Jones, and J. J. Kennedy, 2009: Identifying signatures of natural climate variability in times series of global-mean surface temperature: Methodology and Insights. J. Climate, 22, 6120-6141.

Tolstikov, E. I., 1996: (Ed.), Atlas of the Antarctic. Vol. 1, 126 pp., Glav. Uprav. Geod. Kart. MGSSSR, Moscow.

Trenberth, K. E., J. M. Caron, D. P. Stepaniak, and S. Worley, 2002: Evolution of El Nino-Southern Oscillation and global atmospheric surface temperatures. J. Geophys. Res, 107, 5.1-5.17.

Trenberth, K. E., and D. J. Shea, 2005: Relationships between precipitation and surface temperature. Geophys. Res. Lett., 32, L14703, doi:10.1029/200GL022760.

Trenberth, K. E., J. T. Fasullo, and J. Kiehl, 2009: Earth's Global Energy Budget. Bull. Amer. Meteor. Soc., 90, 311-324.

Twomey, S., 1977: The influence of pollution on the shortwave albedo of clouds. J. Atmos. Sci., 34, 1149-1152.

van Loon, H., and D. J. Shea, 2000: The global 11-year solar signal in July-August. Geophys. Res. Lett., 27, 2965-2968.

Wallace, J. M., Y. Zhang, and J. A. Renwick, 1995: Dynamic Contribution to Hemispheric Mean Temperature Trends. Science, 270, 780-783.

Wallace, J. M., Y. Zhang, and L. Bajuk, 1996: Interpretation of Interdecadal Trends in Northern Hemisphere Surface Air Temperature. J. Climate, 9, 249-259.

Wallace, J. M., and P. V. Hobbs, 2006: *Atmospheric Science: An Introductory Survey*. Second Ed. Elsevier, 505p.

Walsh, J. E., 1978: A data set on Northern Hemisphere sea ice extent, 1953–76. Glaciol. Data Rep. GD-2, Arctic Sea Ice, Part 1, pp. 49–51, http://nsidc.org/, World Data Cent. for Glaciol., Boulder, Colorado.

Wigley, T. M. L., 2000: ENSO, volcanoes and record-breaking temperatures. Geophys. Res. Lett., 27, 4101–4104.

Yang, H., and K. K. Tung, 1997: Water Vapor, Surface Temperature, and the Greenhouse Effect – A Statistical Analysis of Tropical-Mean Data. J. Climate, 11, 2686-2697.

Yulaeva, E., and J. M. Wallace, 1994: The Signature of ENSO in Global Temperature and Precipitation Fields Derived from the Microwave Sounding Unit. J. Climate, 7, 1719-1736.

Zhang, Y., J. M. Wallace, and D. S. Battisti, 1997: ENSO-like Interdecadal Variability: 1900-93. J. Climate, 10, 1004-1020.

Zhang, J., 2007: Increasing Antarctic sea ice under warming atmospheric and oceanic conditions. J. Climate, 20, 2515-2529, doi:10.1175/JCLI4136.1.